Remote Cooling using Cold Electromagnetic Valves to Drive an External Flow Loop on a G-M Cryocooler

by

Kimi Malia Ceridon

B.S., Mechanical Engineering (1999)

Colorado State University

Submitted to the Department of Mechanical Engineering in Partial Fulfillment of the Requirements for the degree of Master of Science in Mechanical Engineering

at the

Massachusetts Institute of Technology

June 2001

Signature of Author.....
Kimi Malia Ceridon
Department of Mechanical Engineering
May 11, 2001

Certified by.....
Joseph L. Smith Jr.
Professor of Mechanical Engineering
Thesis Advisor

Accepted by.....
Ain A. Sonin
Chairman, Department Committee on Graduate Students

Remote Cooling using Cold Electromagnetic Valves to Drive an External Flow Loop on a G-M Cryocooler

by

Kimi Malia Ceridon

Submitted to the Department of Mechanical Engineering on May 11, 2001 in Partial Fulfillment of the Requirements for the Degree of Master of Science in Mechanical Engineering

ABSTRACT

A major limitation of Gifford-McMahon, G-M, cryocoolers is the requirement to conduction cool the refrigeration load. A number of earlier attempts to use check valves to rectify the oscillating pressure from the G-M expansion in an external flow loop were unsuccessful because of valve leakage. A G-M cryocooler has been modified with the addition of Boreas style cold electromagnetic valves to utilize the oscillating pressure to drive the unidirectional flow in an external cooling loop. The cold valve of the Boreas cooler demonstrated minimum leakage and acceptable electrical dissipation even at 4.5 K. Preliminary analysis indicated that the G-M blow down process could be used to power the external flow without seriously degrading the G-M cooler capacity.

Thesis Supervisor: Joseph L. Smith Jr.
Title: Professor of Mechanical Engineering

ACKNOWLEDGEMENTS

I would like to first thank my advisor, Professor Joseph L. Smith Jr., for giving me the opportunity to work on a 'total engineering experience' project. Designing, developing and building a project that started out as a sketch on a piece of paper allowed me to touch on so many of the skills I learned as an undergraduate. It was also inspiring to work with a man who is still in love with being an engineer, who is not afraid to get his hands dirty and who generally likes to tinker. He helped me remember that I wanted to be an engineer because building stuff is fun.

Big thank yous also go out to Mike Damaree, Bob Gertsen and Doris Elsemiller for their support and help and mostly for putting up with me for the last two years.

I would also like to thank my family, Mary, Samuel Juan and Maile and my entire support network. Thanks for being there and for telling me to just go with it. Also, thanks for advising me when I started to take this whole thing way too seriously.

For their financial support, I would like to thank the National Science Foundation. They are really the ones that made my graduate education possible. For the generous donation of equipment, I would also like to thank Leybold Cryogenics and SuperCON. The Gifford-McMahon Cryocooler was really the backbone to this project and the high purity copper wire was the heart of the valves.

Table of Contents

Table of Figures

Nomenclature

Standard Subscripts	
i	general reference
0	initial
gap	property applied to gap
mag	property applied to magnetic circuit
para	property applied to parallel part of magnetic circuit
series	property applied to series part of magnetic circuit
ss	Stainless Steel

Greek Symbols	
φ	Angle subtended by applied load
$\sigma_{bending}$	Bending Stress
θ_c	Angle about core
τ_{shear}	Shear Stress
μ_{χ_1}	Relative Permeability of Cast Iron
X	X-Factor Correlation
Θ_{total}	Rotation Due to 1, 2 and 3
Θ_1	Rotation Due to Load
Θ_2	Rotation Due to Moment
Θ_3	Rotation Due to Torque
Ψ_{total}	Twist Due to 1, 2 and 3
Ψ_1	Twist Due to Load
Ψ_2	Twist Due to Moment
Ψ_3	Twist Due to Torque
δ_{offset}	Offsetting Deflection
δ_{total}	Deflection Due to 1, 2 and 3
δ_1	Deflection Due to Load
δ_2	Deflection Due to Moment
δ_3	Deflection Due to Torque
ϕ	Magnetic Flux
γ	Specific Heat Ratio
μ_0	Permeability of Air
θ_b	Angle subtended by beam
θ_χ	Angle subtended about core
ρ	Resistivity

Symbols	
A_b	Cross Sectional Area of Beam
A_{circum}	Circumferential Area
A_{core}	Cross Sectional Area of Core
$A_{curtain}$	Curtain Area
$A_{valve,bot}$	Valve Head Area, Bottom
$A_{valve,top}$	Valve Head Area, Top
B	Magnetic Field
B_{sat}	Saturation Magnetic Field
C	Capacitance
C_{rect}	Correction Factor for Castigliano's Theorem
$C_{\alpha,i}$	Variables Defined by Roark and Smith
dm	change in mass
D_{port}	Diameter of the Port
d_{tool}	Tool Diameter
e	Electrical Potential
E	Modulus of Elasticity
$E_{capacitor}$	Energy in Capacitor
ecc	eccentricity
E_{fmag}	Energy of Force-Producing Magnetic Field
$E_{kinetic}$	Kinetic Energy
$E_{no\text{-}fmag}$	Energy of Non-Force-Producing Magnetic Field
E_{PdV}	Work Against Pressurize Fluid
$E_{resistor}$	Resistive Energy
E_{spring}	Energy in Spring
E_{stored}	Energy Stored in Magnetic Field
$F_{preload}$	Preload Force on Spring
$F_{applied}$	Applied Force
F_{axial}	Axial Force
F_{BP}	Force Due to Back Pressure
F_{DP}	Force Due to Dynamic Pressure
F_{mag}	Magnetic Force
F_{net}	Net Force Across Valve Head Due to Pressure
F_{offset}	Offsetting Force
F_{radial}	Radial Force arising from Stiffness of Flexure
G_{ss}	Shear Modulus of Stainless Steel
gap	length of air gap in magnetic circuit
gap_{actual}	Actual Physical Gap
$gap_{initial}$	Initial Gap
$gap_{no\text{-}current}$	Gap as it Appears at No-Current Conditions
gap_{offset}	Offsetting Gap
$gap_{theoretical}$	Theoretical Gap
h	enthalpy

i_{coil}	Coil Current
$i_{induced}$	Induced Current
$i_{observed}$	Actual Observed Current
i_{shunt}	Shunt Current
i_{source}	Source Current
$i_{theoretial}$	Theoretical Current
i_{coil}	Coil Current
$i_{\pi,sat}$	Saturation Current at Angle π
I_{xx}	Moment of Inertial about x-x
J_{xx}	Second Moment of Inertia about x-x
k_{sp}	Spring Constant
L_{coil}	Inductance of Coil
l_{ckt}	Length of Circuit
M_0	Applied Moment
$\dot{m}_{choked}$	Mass flow Rate for Choked Flow
m_{core}	Mass of Core
$\dot{m}_{CV}$	Mass Flow Rate in Cold Volume
m_{CV}	Mass in Control Volume
M_{react}	Reactionary Moment
$\dot{m}_{unchoked}$	Mass Flow Rate for Unchoked Flow
N	Turns of the Coil
P_0	Cold Volume Initial Pressure
$P_{crit,He}$	Critical Pressure for Helium
P_{CV}	Cold Volume Dynamic Pressure
P_H	High Pressure
P_L	Low Pressure
$Power_{elect}$	Electrical Power
P_{ratio}	Dynamic Pressure Ratio
P_x	Intermediate Pressure
Q_R	Heat Flow in Regenerator
$r_{av,coil}$	Average Radius of the Coil
R_b	Applied Load
R_b	Radius to Neutral Axis of Beam
R_{coil}	Resistance of Coil
R_{gap}	Reluctance ov Gap
R_{He}	Gas Constant for Helium
R_{mag}	Magnetic Reluctance
R_{para}	Reluctance of Parallel Flux Path
R_{series}	Reluctance of Series Flux Path
R_{shear}	Reactionary Shear
t	time
T_0	Applied Torque
T_0	Cold Volume Initial Temperature

t_{beam}	Height of Beam
T_{CV}	Cold Volume Dynamic Temperature
T_{react}	Reactionary Torque
v_0	Cold Volume Initial Specific Volume
$V_{applied}$	Applied Voltage
V_c	Cold Volume
V_{cap}	Capacitance Voltage
V_{coil}	Coil Voltage
v_{CV}	Cold Volume Dynamic Specific Volume
V_{CV}	Cold Cylinder Volume
vel_{core}	Velocity of the Core
V_{in}	Applied Voltage
V_{shunt}	Shunt Voltage
V_{step}	Step Voltage
w_{beam}	Width of Beam
y	Distance Along Y-Axis

Abbreviations

C	Cold Volume
CH	Cold Head
Comp	Compressor
D	Displacer
D_R	Displacer Motor
G-M	Gifford McMahon
HE	Heat Exchanger
HEI	Heat Exchanger Inlet
HEO	Heat Exchanger Outlet
R	Regenerator
RCE	Regenerator Cold End
RWE	Regenerator Warm End
S	Surge Volume
SI	Surge Volume Inlet
V1	Low Pressure Warm Valve
V2	High Pressure Warm Valve
V3 & V4	Cold Electromagnetic Valve
W	Warm Volume

CHAPTER 1- Introduction

In cryocooler design, actual thermal efficiency is strongly affected by irreversibilities that arise from mechanical and electrical processes. At the time of this thesis, the Cryogenic Engineering Laboratory at Massachusetts Institute of Technology was amidst designing a new cryocooler that incorporated various components designed and tested in the Laboratory. Specifically, it is the intent of this thesis to design and test low-loss, both mechanically and electrically, electro-mechanical valves for use of transporting low-temperature helium between two cold volumes.

For the purposes of this thesis, electro-mechanical valves were fit to the cold volume of a 150-Watt cooling capacity Gifford-McMahon cryocooler. The fluctuating pressures of the Gifford McMahon cycle drove the flow-through valves and made an ideal test-bed for examining the electro-mechanical properties of the valves. They were operated between the cold volume of the Gifford-McMahon cryocooler and an externally designed surge volume. The electro-mechanical valve design itself presented

1) A fully self-contained cold electro-mechanical valve with a single moving core using the working fluid of the cycle for cooling.
2) A new flexure bearing design to maintain friction-free valve displacement.
3) An analysis of physical characteristics of electromagnetic circuit that can be applied to designing controlled valve motion to minimize electrical inefficiencies.

The following pages discuss the history in motivating this project, the system in consideration, the electromagnetic valve design, test procedures and results, conclusions and the feasible uses of the design.

1.1 Project Motivation

The basic process of cryogenic refrigeration involves pre-cooling high pressure gas to a low temperature. The decrease in temperature is typically accomplished via an expansion process that does external work in the cycle. This process cools the fluid by expanding it to a low pressure. Once cooled, the gas absorbs heat by applying it to a heat load. The pre-cooling process then occurs by applying the low-pressure, cool fluid to the high pressure gas prior to starting the cycle again.

Cryocoolers that run these refrigeration cycles are usually self-contained systems that provide local cooling at temperatures less than 100K. While large-scale cryocooler systems employ turbines for the expansion process, small-scale cryocooler systems typically use positive-displacement pistons or displacers for this process. An example of a small-scale, positive-displacement system is the Gifford-McMahon cryocooler cycle and system.

Due to its mechanical simplicity, the Gifford-McMahon system is one of the more commonly used cryocooler configurations. The basic components of the system are a displacer piston, a regenerator and a high speed compressor. The Gifford-McMahon (G-M) system operates through cyclic pressures. The regenerator and cold displacement volume are cycled between a system-high-pressure and a system-low-pressure provided by the external compressor. This is accomplished by means of warm mechanical valves operating between the cryocooler and the compressor.

However, three limitations arise with the G-M cycle. First, a major penalty for the mechanical simplicity is that the refrigeration efficiency of the G-M Cycle is limited. Second, a G-M cycle requires that a load be conduction cooled by direct contact to the cold-expansion cylinder. This prevents the G-M cycle from providing remote cooling for applications external to the system. Third, as a result of the limited heat capacity of the regenerator matrix for counterflow pre-cooling of the high pressure fluid, the G-M system's efficiency is limited at temperatures below 20K. For details of a G-M cryocooler process, refer to Chapter 4- Thermodynamic Cycle Analysis

For the past several years, the Cryogenic Engineering Laboratory at M.I.T. has undertaken several research projects directed at overcoming these limitations of the G-M cryocooler. One of the topics studied was the design of low loss cold electro-mechanical (EM) valves to transfer cryogenic fluid. With respect to the G-M cryocooler cycle, these valves were developed to overcome the requirement of the load to be conduction cooled. Here, cold EM valves were designed to work in conjunction with the oscillating pressures of the G-M cycle to drive the working fluid to a remote cooling location. This was accomplished by applying a uni-directional flow loop to the cold volume of the G-M cryocooler.

The use of cold EM valves to drive flow loops originated with the work of J.A. Crunkleton in the 1980s. In conjunction with a new cryocooler cycle called the Boreas Cycle, Crunkleton developed a low-loss cold EM valve called the Boreas Valve.[1] In the manner proposed above, this valve was used for the positive-displacement expansion process of the cycle. This work also stemmed from research completed previously at M.I.T.

From the research completed at M.I.T.'s Cryogenic laboratory, it was been suggested that cold EM valves could be applied to the expansion process of a high efficiency Collins Cycle system. Rather than the regenerator and positive-displacement piston used in the G-M system, this system utilizes a counterflow heat exchanger with a positive-displacement valve expander. For a complete description of this cycle refer to U.S. patent # 6,205,791.[2]

More recently, R.E. Jones and J.L. Smith Jr. designed a floating piston expander called a slug-tube expander.[3] In this study, they utilized pneumatic valves to complete the expansion process. However, to improve both mechanical efficiency and valve response time, it was proposed that cold EM valves would be better suited as positive displacement expander valves for this process.

In conjunction with the previously completed research, this thesis proposes to fulfill two objectives. First, it is the intention to develop and verify design and manufacturing techniques for low-loss EM valves. Second, this thesis will demonstrate that a G-M system can provide remote cooling using a unidirectional flow loop.*

* All superscripts in the text body refer to the number of the reference appearing pages 101 and 102.

CHAPTER 2- Conceptual Design

2.1 General Valve Design Considerations

The motivation of this project was to prove that remote cryogenic cooling could be achieved through the implementation of low-loss valves. Ultimately, efficient remote cooling would lead to efficient working fluid transfer during the full adiabatic expansion in the new cryocooler cycle. As a test bed for these EM Valves, a G-M cryocooler was retrofitted with an external flow loop and the Cold EM Valves were placed inline of this loop. This allowed the valves to be tested in conjunction with a cycle of known performance.

The primary concept behind this design was an inward-opening, normally-closed valve using a Ferromagnetic Core that moved inside of a stationary electromagnetic coil. The valve design worked on the same principles as a solenoid type valve. However, unlike a solenoid valve, the physical behavior of he electromagnetic circuit was modeled so the motion of the valve could be controlled. Controlling the motion of the Ferromagnetic Core itself minimized the high electrical and mechanical energy losses normally associated with a solenoid valve. Finally, implementing no friction principles in the design would further reduce mechanical losses. To aid in assembly, testing and manufacturing, the valve was made modular with two distinct assemblies: the Housing Assembly and the Valve Assembly. Addressing initial EM valve design concepts and a brief description of equipment used for the adaptation of EM valves to the Gifford-McMahon, G-M, cycle are presented in this chapter. Details of the design of each component of the EM valve appear in Chapter 3- Valve Design.

A typical solenoid valve design incorporated a ferromagnetic core moving inside of a stationary electromagnetic coil. The motion of the solenoid was initiated by designing an adjustable gap into an electromagnetic circuit. This provided a discontinuity in the magnetic permeability of the circuit. An applied voltage excited the electromagnetic circuit and the motion of the core acted to eliminate this discontinuity but eliminating the air gap in the circuit. In solenoid operation, typically a voltage large enough to move the core was applied to the circuit and then maintained until the end of the valve travel. When the magnetic field has sufficiently reduced, a compression spring forced the core in the opposite direction returning the gap to its initial geometry.

Essentially, this was a 'slam-slam' way of designing an electromagnetic valve. In a normally closed valve, the valve was thrown open and the core was slammed against the stops at the end of its travel. Slamming it shut using the action of a compression spring then closed the valve. As can be imagined, this type of design led to large electrical and mechanical losses. An unnecessarily large magnetic field was build up in the circuit, wasting the potential energy stored in the magnetic field. Excess electrical energy typically went into resistive heating. Large impacts at the stops also resulted in large mechanical and kinetic losses and significant wear and tear. This approach to valve design was not sufficient for cryogenic applications.

For this application, it was desired to examine the electro-mechanical properties and behaviors of a solenoid valve and then to apply the concepts of control design to produce a controllable electromagnetic valve. Instead of the 'slam-slam' design philosophy, these valves were to have a prescribed position, velocity and acceleration profile. Enough voltage was to be applied to the circuit to open the valve. However, the core would reach

the end of its travel with minimal velocity. The valve would then be held open a prescribed amount of time. Finally, the excess magneto-motive force would be used to work against a compression spring to return the valve to its closed position with minimal velocity. It was intended that the core just kiss the stops at both ends of its travel.

When dealing with cryogenic fluids, such as helium, leaks at sealing surfaces are commonplace. At a valve seat, the closing force must be sufficient to seal the mating surfaces from leaks. The normally-closed configuration was chosen to ensure not only that maximum seating force occurred during the valve's natural, at-rest position, but also that no external magnetic field would need be applied to maintain the valve closed. The inward-opening, normally-closed design allowed the Valve Stem to be maintained in tension between the Valve Head resting against the valve seat and a preloaded compression spring. The magneto-motive force would act counter the spring force to open the valve or close the magnetic gap and would only be necessary when valve motion was required.

In order to reduce mechanical losses in the valve, it was necessary to implement low- and no-friction concepts to the design. To reduce frictional components, the Valve Stem, Valve Head and moving Ferromagnetic Core were designed as the only moving assembly in the valve. The Head-Stem-Core Assembly moved within the Stationary Coil and Electromagnetic Circuit Assembly. The valve was designed so the Head-Stem-Core assembly was maintained centered within the Electromagnetic Circuit Assembly without any sliding surfaces. This was accomplished by a flexure bearing design that provided sufficient radial stiffness to hold the Head-Stem-Core Assembly centered. However, the flexure bearings were also designed so the axial stiffness was low enough to present only negligible axial forces compared to the axial magneto-motive and spring forces (see Section 3.4- Multi-leaf Flexure Assembly Design).

Finally, manufacturability concepts were addressed in the initial design of these valves. In order fit these valves to the given G-M cryocooler for testing, a modular design was incorporated. The two major assemblies are the Housing Assembly and the Valve Assembly. Within the Valve Assembly were two Multi-leaf Flexure Assemblies, a Head-Stem-Core Assembly, an Electromagnetic Circuit Assembly and a Compression Spring Assembly. This allowed testing, trouble-shooting, assembly and repair of individual modules first. Once individual components were tested, the complete unit was then examined. Chapter 3- Valve Design deals with the design of each individual assembly.

2.2 Equipment Description and Specification

The equipment used to test the PhaseI EM valves was a Leybold Cryogenics' Coolpower 150 cryocooler. This particular cryocooler operated on a standard G-M cryocooler cycle, between the pressures 275 psig and 75 psig. A Leybold Cryogenics' Model UCC 066S Scroll-type Helium Compressor[4] provided the two supply pressures. This system provided constraints on the overall size and geometry of the valves.

Figure 2.1 describes the geometry of the system and Table 2.1 outlines all associated dimensions[5]. In reference to Figure 2.1, all components were pre-manufactured and donated by Leybold Cryogenics. As shown, the two main sections of the cryocooler referenced here were the displacer driving mechanism, D_R, and the cold head, C. No modifications were made to the displacer driving mechanism. The Cold Head remained essentially unmodified as well. The only exception was the machining of attachment points at the Cold End for the EM valves to drive the external flow loop. The helium supply lines connect to the displacer driver mechanism at the quick-release valves shown.

The EM valves were attached to the face of the Cold End of the Cold Head. This point is denoted section A-A on Figure 2.3 and will be referred to as the Cold End henceforth. The EM valves were designed in a manner to maximize the size of the valves while allowing two valves, one exhaust and one intake, to be placed side by side at the Cold End. The EM valves used the G-M cycle to drive the external flow loop. The external flow loop consisted of an intake EM valve, an exhaust EM valve, a surge volume and a heat exchanger.

As stated previously, the valves were designed with two separate main assemblies, the Housing Assembly and the Valve Assembly. The Housing Assembly was permanently attached to the face of the Cold Head at the Cold End via fillet welds. The second assembly, the Valve Assembly, was assembled independent of the Housing Assembly. The Valve Assembly was inserted into the Housing Assembly. To minimize relative motion, misalignment, and vibration the Valve Assembly had a tight sliding fit clearance between its outer wall diameter and the inner diameter of the Housing Wall. Once in the Housing Assembly, the Valve Assembly was held in compression by compressing Belville springs against the assembly. The entire system-the valves, the surge volume, the heat exchanger and the cryocooler- was sealed via indium seals at the external flow loop end of the valves. This allowed the valves, surge volume and cryocooler to form a self-contained unit. Once the supply lines were connected between the compressor and the cryocooler, the scroll compressor supplied helium for the entire unit.

The EM valves had a 3/8-inch throat diameter and with a valve travel of 0.031-inches. This allowed the cold head cylinder cap at the Cold End to be modified to accommodate the valves. Since the valves were normally-closed and opened into the cold volume of the Cold Head, the Valve Head could not interfere with the motion of the Displacer. The minimum cold volume in the Cold Head was essentially zero. Thus, there was approximately zero clearance between the Displacer and the Cold Head Cylinder Cap when the Displacer was at the bottom of its travel. Therefore, when the valve was in its full-opened position the Valve Heads extended no further than flush with the inner surface of the Cold Head Cylinder Cap. This was accomplished by first boring two holes into the cylinder cap. The size of these holes was determined by the size of the throat

section of the flexure assembly and the throat section of the Housing Assembly. These holes were chamfered at 45-degree angles inside of the cold head to allow the Valve Head to nest inside of the cylinder cap (see Section 3.2- Valve Housing Assembly for a detailed discussion). Figure 2.2 shows graphically how this was accomplished.

Figure 2.3 shows a block diagram of how each assembly fit together relative to the other assemblies. As shown, once fully assembled, the entire external flow loop, from section S-S to the surge volume was placed inside of a 5-inch diameter, 30-inch-long canister, that provided a vacuum space around the assembly. This canister was sealed via a Parker o-ring at section S-S. All electrical connections were fed from the vacuum space to the surroundings via a hermetically sealed feed-thru plug at the feed thru point. The length of the valves and the size of the surge volume were limited only be the size of the vacuum can. As is later shown, the size of the surge volume was maximized within these constraints. The valve length was chosen to provide sufficient volume for the Stationary Coil while minimizing manufacturing and dynamic complications. These factors are discussed in detail in Section 3.1- Overall System Design.

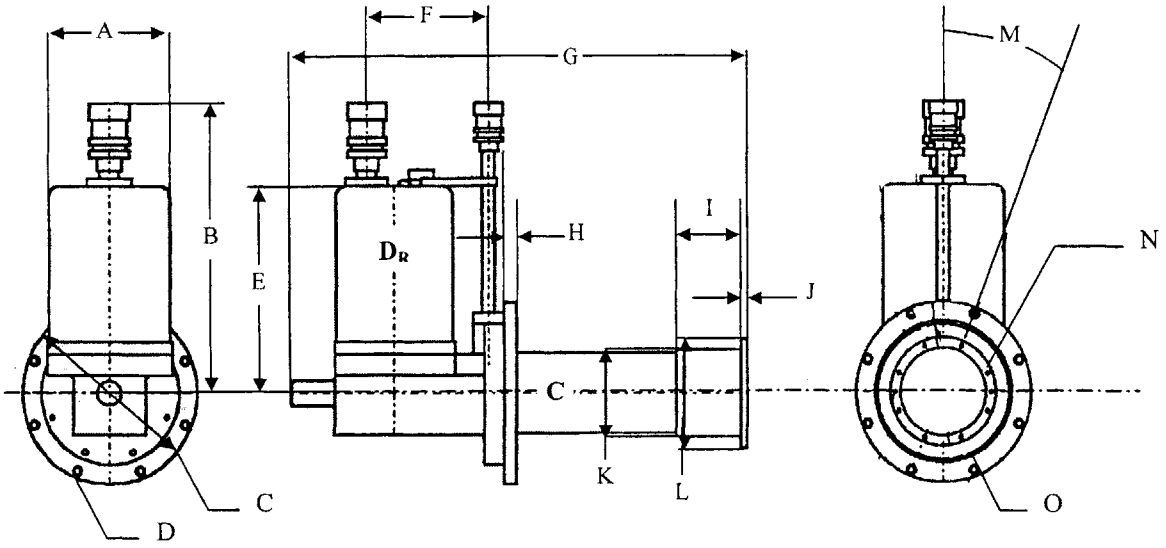

Figure 2.1 - Schematic of Leybold Coolpower 150 Cryocooler.[5]

Dimension	Quantity (inch)	Dimension	Quantity (inch)
A	4.75 DIA	I	2.84
B	11.19	J	0.24
C	7.00 DIA	K	3.39 DIA
D	0.28 DIA THRU, 0.41 DIA x 0.29 DP C'BORE, 8 PLACES ON 8.50 DIA B.C.	L	4.20 DIA
E	8.00	M	22.5 °
F	5.00	N	4-40 TAP on 3.80 DIA B.C.
G	18.65	O	5.24 ID x 5.44 OD O-RING PARKER #2-160
H	0.60		

Table 2.1 - Dimensions of Leybold Coolpower 150 Cryocooler[5] Corresponding to Figure 2.1.

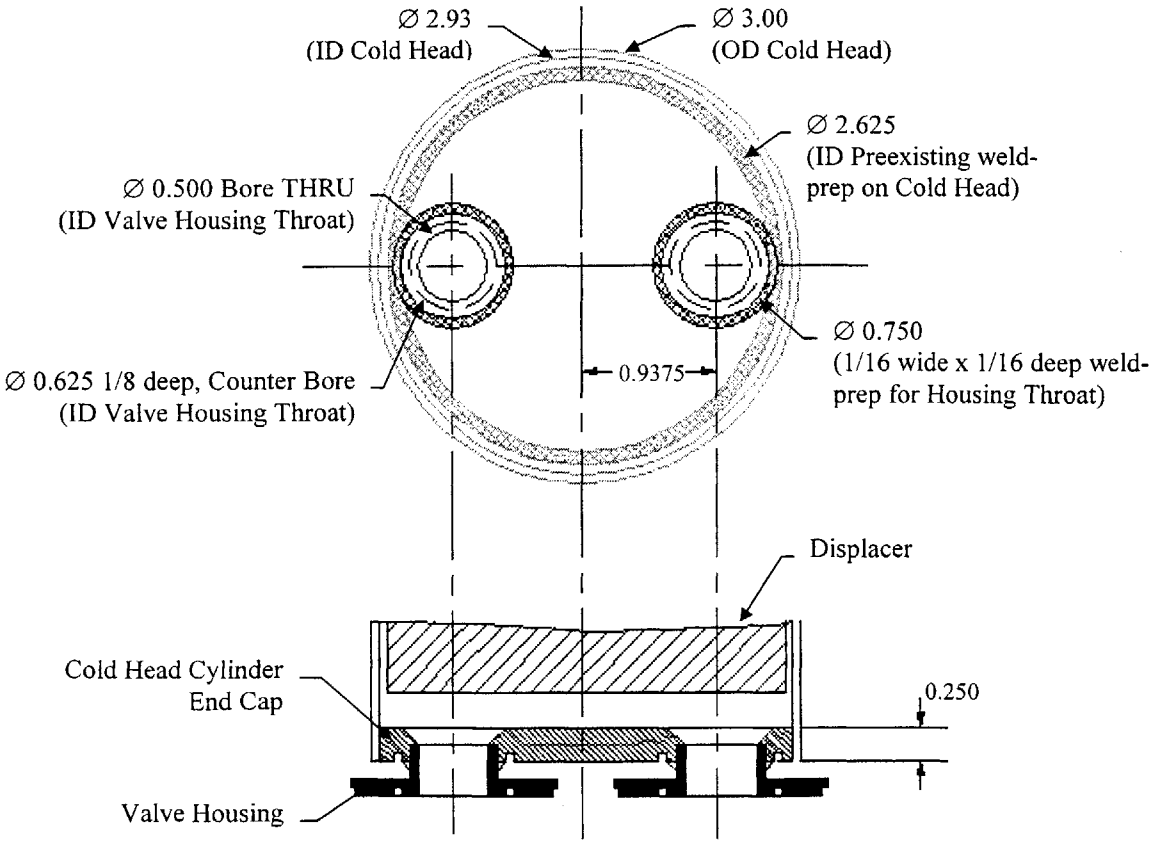

Figure 2.2- Cross-sectional view of chamfering of Cold Head Cylinder Cap.

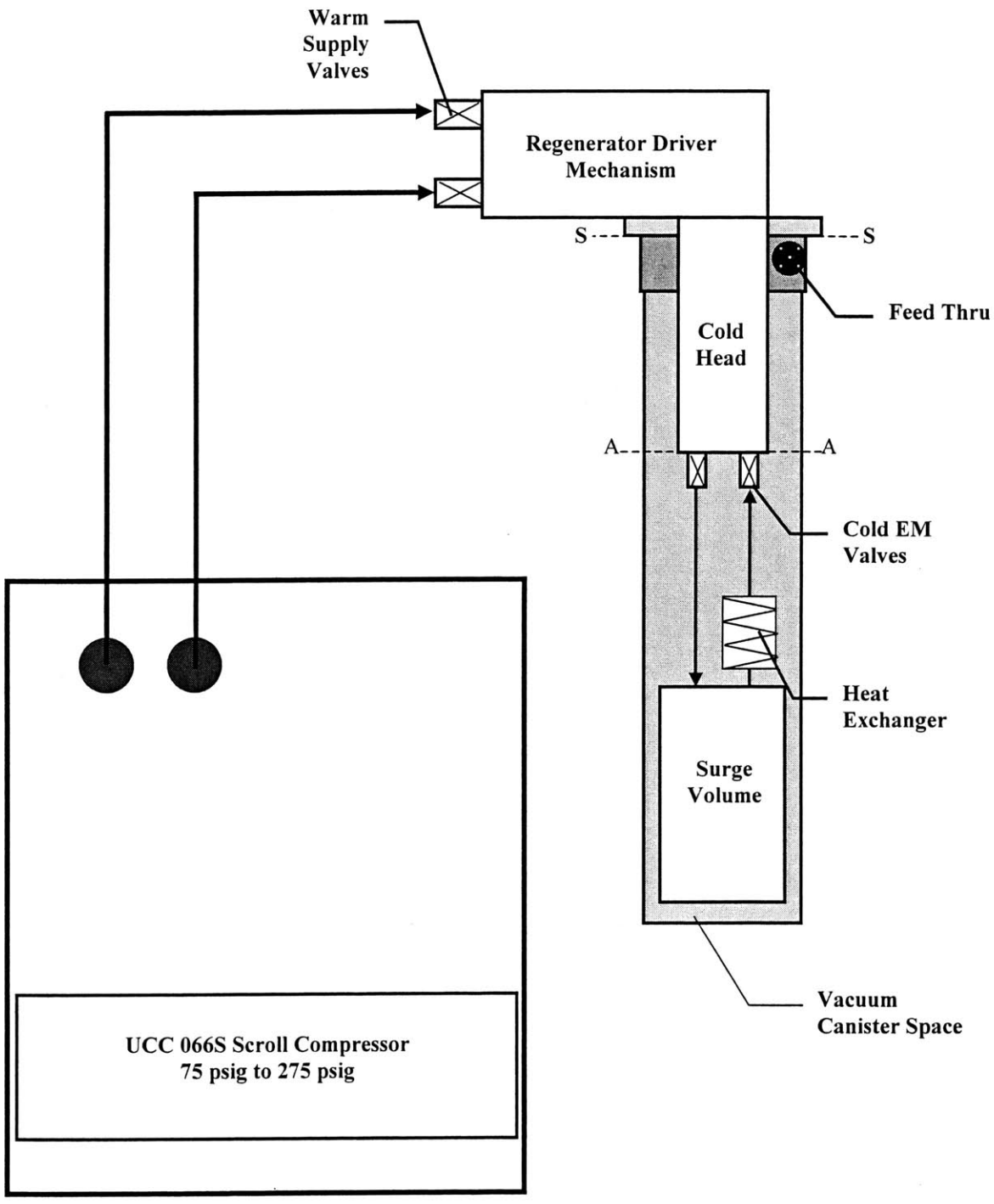

Figure 2.3- Block diagram of Entire System

CHAPTER 3- Valve Design

When designing the Phase I EM valves, several factors affected the mechanical design of the components in the system. These factors were associated with space constraints, fluid dynamics, material properties and electro-mechanical behavior.

First, the valves had to work in conjunction with the pre-existing equipment. The main focus of this preliminary design was to examine the characteristics and behaviors of this particular EM valve and Electromagnetic Circuit Assembly. Therefore, it was desired to make them as large as the geometry of the equipment would allow for easy physical examination. The minimum valve travel was specified by matching the cross-sectional area of the throat to the curtain area of the valve at the full-opened position. Additionally, as has been stated, the valves were configured in a normally-closed, inward-opening fashion. This set limits on the amount of valve travel, the Electromagnetic Circuit Assembly geometry and the Head-Stem-Core Assembly.

Second, it was desired to utilize the working fluid to cool the Stationary Coils during operation. This required that the design incorporate a fluid pathway through the valve. At minimum, the cross-sectional area of this pathway had to be the same as the throat area and the curtain area.

The third factor was related to material science considerations. In this application, there are four items that affect material selections: operating temperature, magnetic properties, electrical properties and strength.

Since the operating temperature of the valves was set by the cryocooler between 77 and 83.5 K, it was necessary that all materials chosen for the design had similar coefficients of expansion and that they maintained desirable material properties at this temperature or less. This was achieved by manufacturing all components from steel alloys. Ideally, to meet this condition, all components would be made of the same material; however, as is next explained, this was not possible.

With respect to magnetic properties, it was desired to have a highly permeable magnetic circuit. However, for optimal magnetic performance, it was desired for the magnetic field to remain concentrated only in this circuit. So, to avoid leaking the magnetic field into surrounding components, it was also favorable for the rest of the valve to have relatively low magnetic permeability. For this reason, it was not possible to manufacture all components of the same material.

In a similar manner, it was desired for the Stationary Coil to be highly conductive with very small and predictable changes in resistivity with the changing temperature. Since the valve was to be manufactured of steel alloys, which are conductive, the copper wire was coated to insure that the coil did not short circuit to other valve components. Additionally, most common copper alloys exhibit non-linear material characteristics at low temperatures. This is due to the differences in properties between the copper and the alloying inclusions. For this reason, a copper alloy was chosen to minimize these non-linearities. This characteristic and the copper selection are described in-depth in Section 3.3-Electromagnetic Circuit Assembly Design.

The fourth material factor for consideration was the strength of the material. Once assembled, most components were held in either a compressive or tensile stress state. However, since the components were designed of steel and the loads were relatively

small, this was not a concern. Concerns of strength were address primarily in the Multi-leaf Flexure Assembly design. Since the flexures were as thin as possible with deflections on the order of three- to six-times the thickness of the material, a detailed stress-strain analysis was performed and substantial safety factors were incorporated. This analysis is detailed in Section 3.4- Multi-leaf Flexure Assembly Design.

The final factor that affected mechanical design was electro-mechanical behavior. As stated, these valves were low-loss electro-mechanical valves. With that in mind, electro-mechanical losses had to be minimized. Thus, unique manufacturing techniques were incorporated to reduce and/or eliminate eddy currents in the electromagnetic circuit. The circuit geometry was also carefully considered to minimize the amount of magnetic field built up and left in the circuit during operation. Finally, shown in Chapter 6, the electro-mechanical behavior was tested and analyzed in order to design empirical correlations that served as models in the design of a valve controller.

This chapter presents the mechanical design considerations used designing low-loss, controllable, electro-mechanical valves.

3.1 Overall System Design

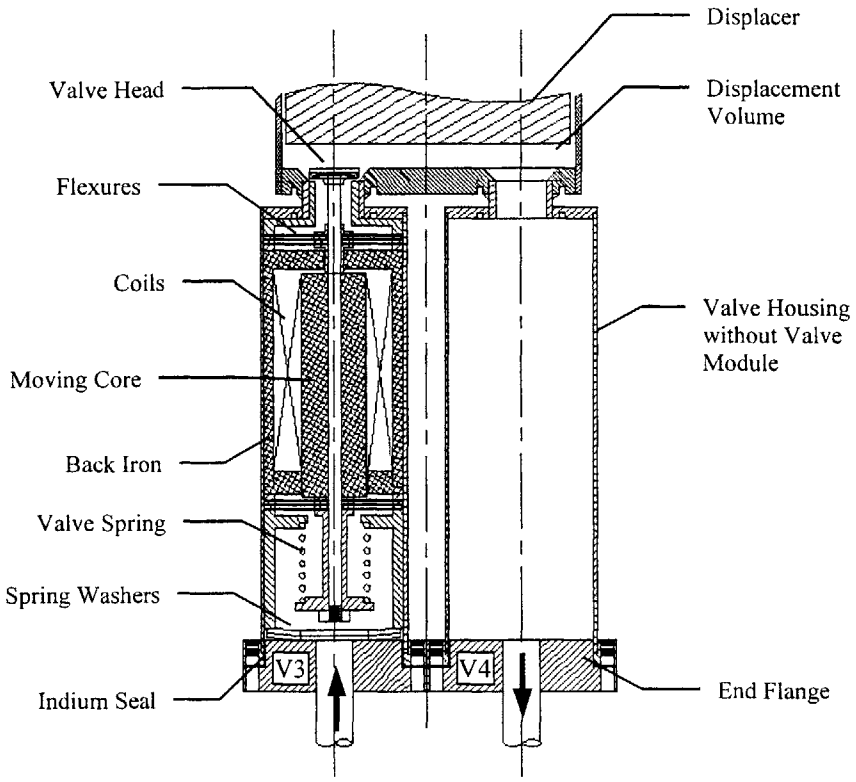

Figure 3.1- Depiction of components of the valve. Right is the housing assembly; left includes the valve assembly

In Figure 3.1, the general configuration of the EM valves are denoted V3 and V4. This describes the position that the valves were attached to the cold end of the G-M cryocooler. In Figure 3.1, the left valve is shown as the intake and the right is shown as the exhaust. The major components of the valve assembly are annotated on the intake and the valve housing is annotated on the exhaust. As stated previously, each Valve Assembly consisted of two Multi-leaf Flexure Assemblies, a Head-Stem-Core Assembly, an Electromagnetic Circuit Assembly and a Compression Spring Assembly. Each of these assemblies is depicted in Figure 3.1. Figure 3.2 is a photograph of the entire valve assembly. In this chapter, the design, manufacture and assembly of each of the valve components are discussed in detail.

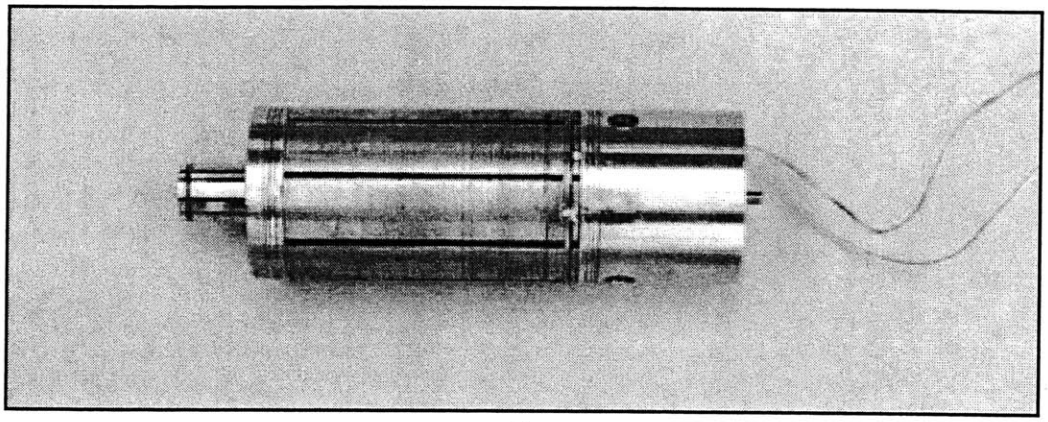

(a)

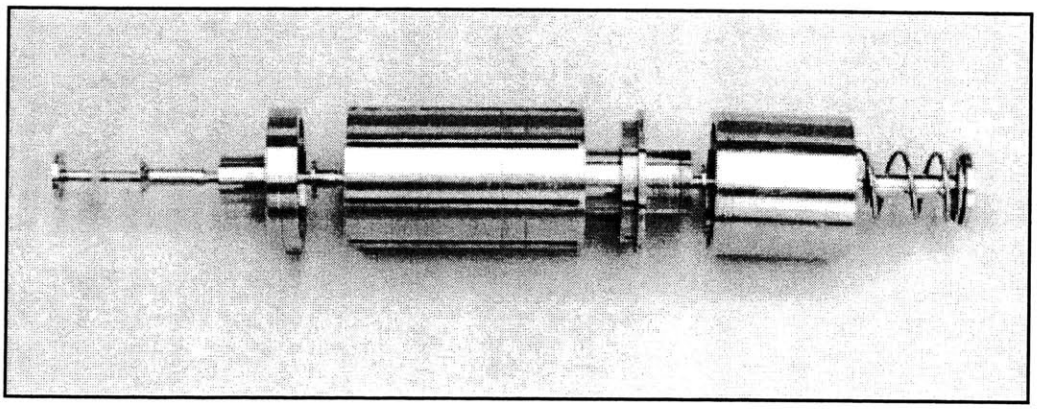

(b)

Figure 3.2 – Photograph of the Valve Assembly.
(a) fully assembled
(b) exploded view

3.2 Housing Assembly

The most influential factor in designing the Housing Assembly was the geometry of the pre-existing cold head. Once the dimensions of the housing were determined, the outer radius of the Valve Assembly was established. The housing was designed to maximize the size of the valves by utilizing all of the space available at the cold end of the cold head. The Housing Assembly was also designed to minimize the impact of the valve on the original system's performance and geometry. Ultimately, two identical housing assemblies were permanently affixed to the Cold Head Cylinder Cap. They were placed symmetrically about the centerline of the cold head. Here, the Housing Assembly design is examined in depth.

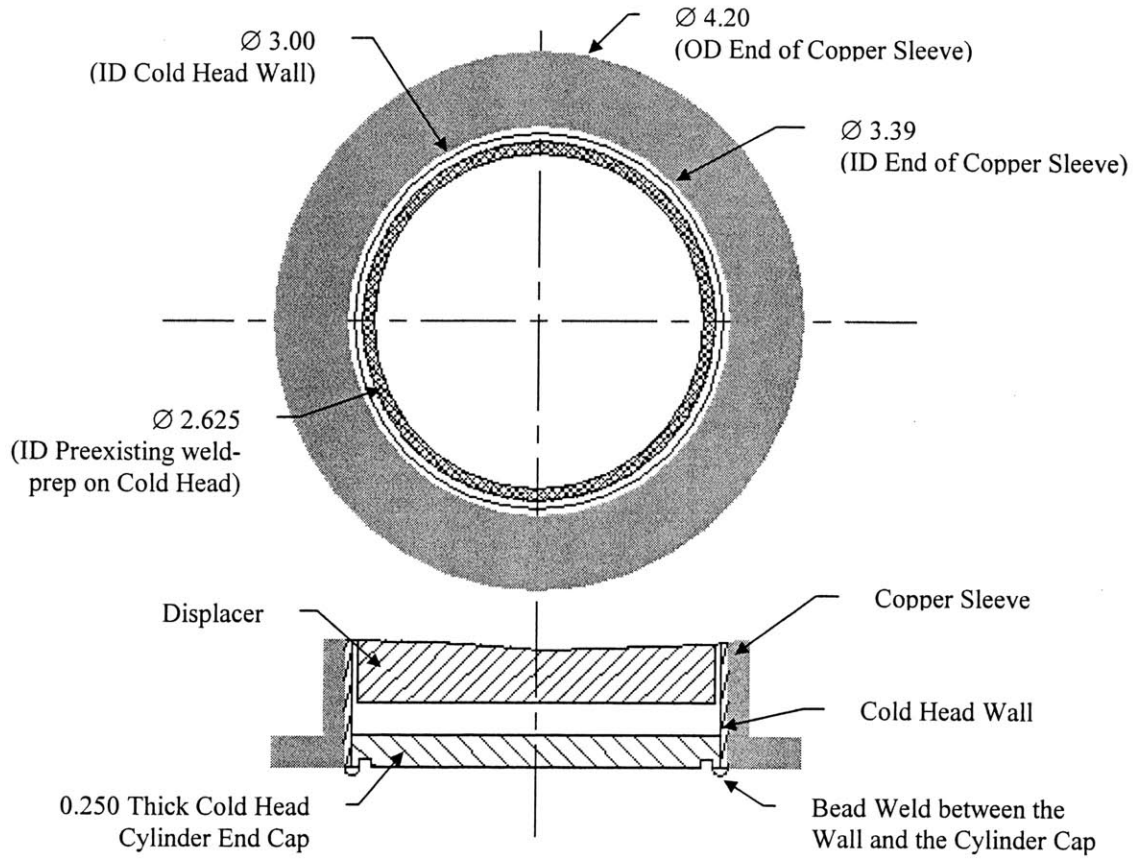

Figure 3.3 - Close up view of the cold end geometry depicting weld-preps, cap thickness and pertinent geometry.

The first task was determining the placement of the Housing Assembly on the Cold Head Cylinder Cap. The cylinder of the cold head had a 3-inch internal diameter and a 0.035-inch wall thickness. The stroke of the displacer went from 0 to 0.625-inch from the surface of the Cold Head Cylinder Cap. All components of the commercial cryocooler were maintained and modified only for the purpose of valve attachment. This geometrically limited the size and position of the valves relative to the Cold Cylinder.

Figure 3.3 shows a cross-sectional view of the Cold Head Cylinder Cap as it appeared in reference to the Cold End. The thickness of the Cold Head Cylinder Cap was ¼ -inch. Pertinent features, such as weld beads and weld-preps are depicted here. Since it was desired to maintain the structural features of the cryocooler, all manufacturing was done to accommodate the existing features of the Cold Head.

Each Housing Assembly consisted of five components: the Throat, the Cylinder Cap, the Wall, the End Flange and the Sealing Cap. Each of these components had a circular cross-section concentric about the same centerline. Since the Housing Assembly was permanently fixed to the face of the Cold End of the cryocooler, the alignment of the Valve Assemblies within the Housing Assembly was critical. This presented difficulties in the assembly and fixation of the Housing Assembly. For proper alignment, it was important to ensure each component was concentric with each other component in the

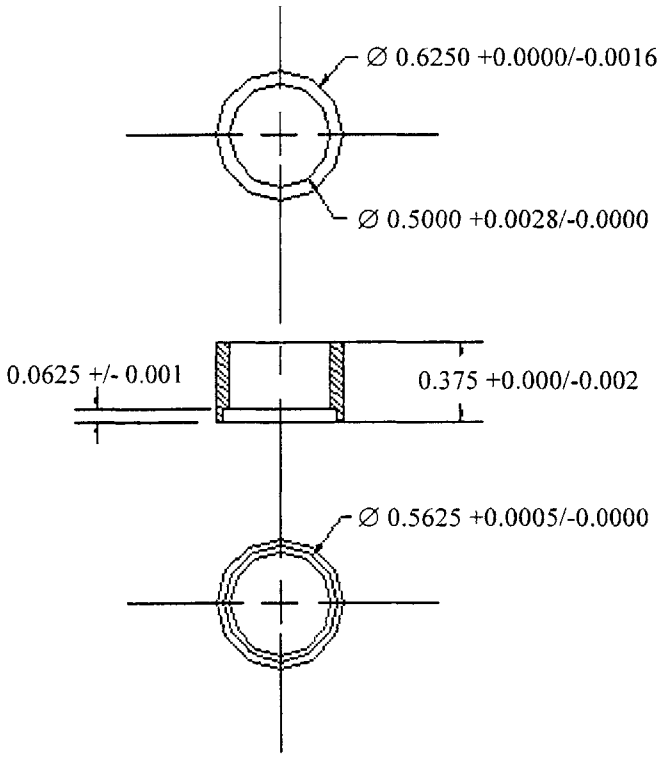

Figure 3.4 - Standard orthographic view of throat

assembly. However, this was not simply a task of assembling the housing then welding the entire assembly to the Cold Head Cylinder Cap. Due to space constraints, the each component of the housing was welded to the Cold Head Cylinder Cap in a systematic manner.

Design of the housing began with the placing two throat sections as far apart as possible on the Cold Head Cylinder Cap. The throat was chosen as ½-inch diameter, stainless steel tubing with a $^1/_{16}$-inch wall thickness. A $^1/_{16}$-inch weld-prep was required to attach the throat sections to the face. An orthographic view of the Housing Throat appears in Figure 3.4.

Taking into consideration the weld-prep and weld bead that existed on the Cold Head Cylinder Cap, the maximum allowable distance placed the centerlines of the throat sections 1.875-inches apart.

With the throat geometry specified, two ½-inch holes were bored through the Cold Head Cylinder Cap. They were centered 1.875-inches apart. The holes were then chamfered at 45-degrees inside of the Cold End to a depth that allowed top the valve head to sit flush or below the internal surface of the Cold Head Cylinder Cap. The Housing Throats were then butted against a counter-bore that was machined into the outer surface of the Cold Head Cylinder Cap (Refer to Figure 2.2 for details of this machine work). The weld-preps for the throat sections were machined into the face of the Cold Head Cylinder Cap. The throat sections were clamped into the counter-bore and TIG-welded directly to the Cold End face. TIG-welding was accomplished by rotating the cold head and throat about the Housing Throat centerline on a variable speed lathe.

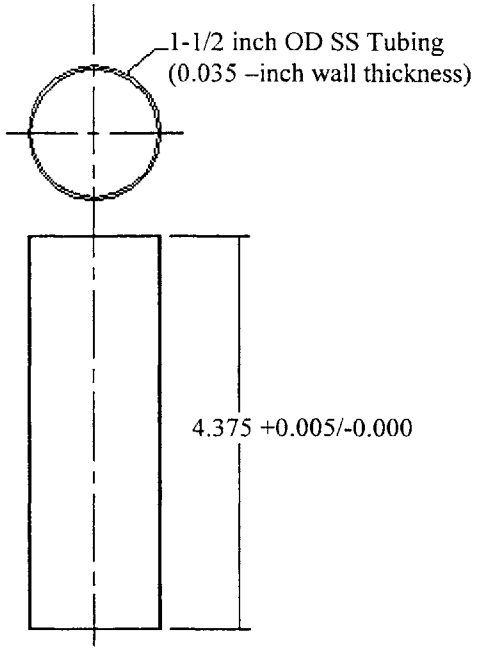

Figure 3.5 Standard Orthographic View of Housing Wall.

The Housing Wall was chosen as 1.50-inch stainless steel tubing with a wall thickness of 0.035-inch. The length of the housing was chosen to accommodate the full length of the valve assembly; this dimension is addressed in Section 3.5- Compression Spring Assembly. Figure 3.5 shows an orthogonal view of the Housing Wall. The specification of the Housing Wall dimensions allowed a $^1/_8$-inch thick Cylinder Cap to be designed. The outer and inner diameters of the Housing Cap were 1.50-inches and 0.875-inch, respectively. A 0.0035-inch wide, $^1/_{16}$- inch deep flange was machined at the outer diameter of the Housing Cap to accommodate sliding the Housing Wall over the Housing Cap. At the inner diameter, a $^1/_{16}$- inch weld-prep was machined to weld the Housing Cap to the Housing Throat. The placement of the valves in the Cold Head is represented in Figure 3.6.

The 1.50-inch diameter wall left a $^3/_8$-inch clearance between the two housing walls. The final geometric constraint arose from this dimension. Figure 3.5 depicts how the preexisting weld beads, weld-prep and geometry of the Cold Head interacted with geometry proposed here. This is an end-on view of the Cold End with the weld-preps and pertinent housing diameters depicted.

The Housing End Flange and Sealing Cap served two purposes. First they created two mating surfaces for squeezing an indium seal. These mating surfaces are denoted on Figure 3.1. This was the temporary seal between the valves and the external flow loop that isolated the system from the surroundings. The second purpose of these components was to compress the Belleville springs between the Sealing Cap and the Valve Assembly.

Opposite the indium seal, the Sealing Cap was designed to mate with the Housing End Flange and compress the Belleville springs. The thickness of the Sealing Cap, ½ - inch, was chosen to be sufficient to extend far enough into the housing to compress the Belleville springs. The mating surface was designed with 12 symmetric 5-40 thru holes to match those of the Housing End Flange. 12 5-40 allen-head cap screws were used to mate the Housing End Flange to the Sealing Cap and once tightened, an indium seal and Belleville springs were compressed. From previous work done by Brisson[16], 12 screws were chosen to provide sufficient compressive force on the indium seal to ensure proper sealing of the valve housings.

Finally, a bore at the center of the Sealing Cap accommodated the $^3/_8$-inch copper tubing. These ports allowed the helium flow to pass between the Cold Head and the external flow loop. Figures 3.7 and 3.8 show standard orthographic views of the Housing End Flange and Sealing Cap. The total assembly can be viewed in Figure 3.1 of the previous section.

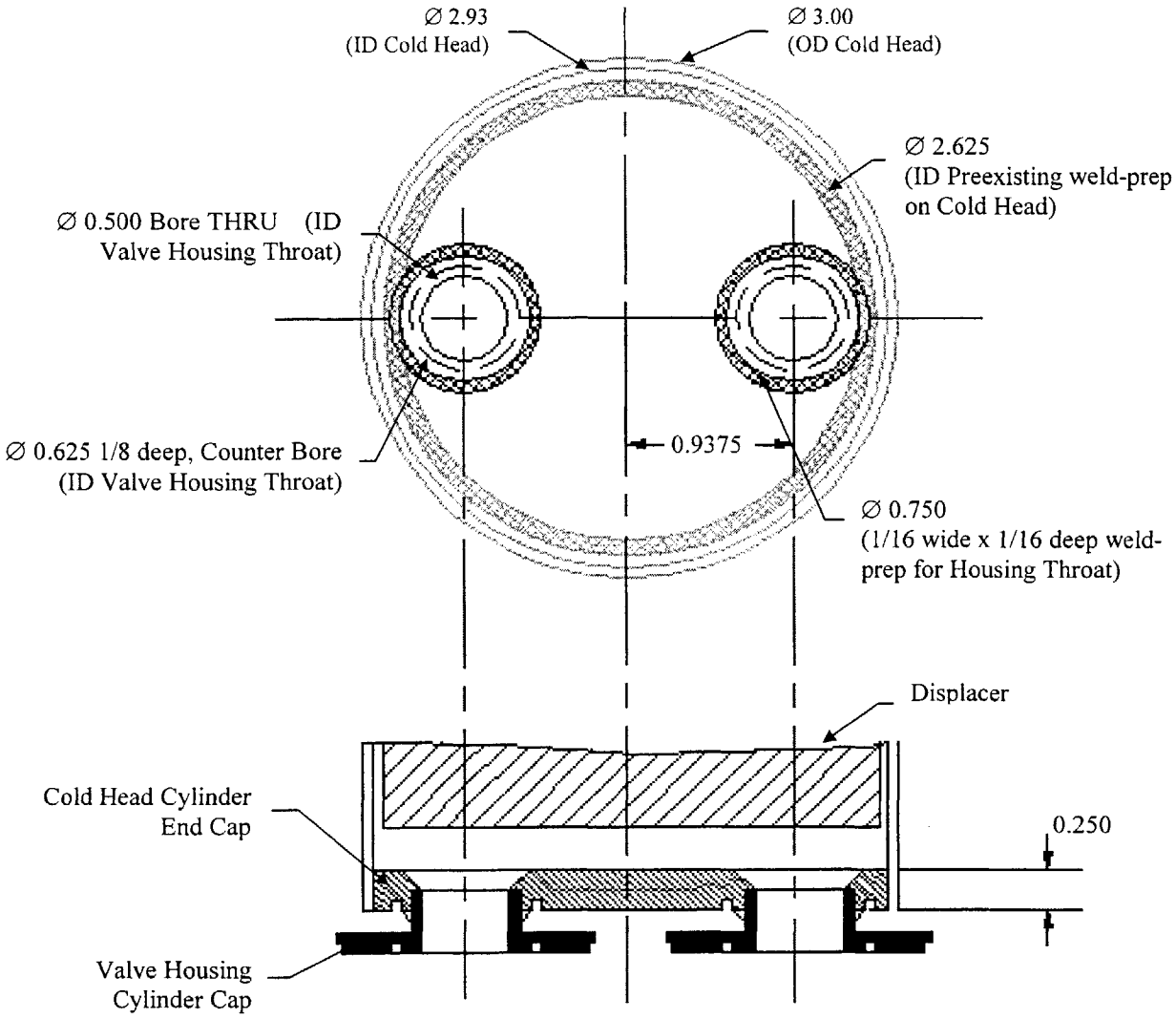

Figure 3.6 – Dimensions of the Cold Head relative to the Valve Throat and Cylinder Cap.

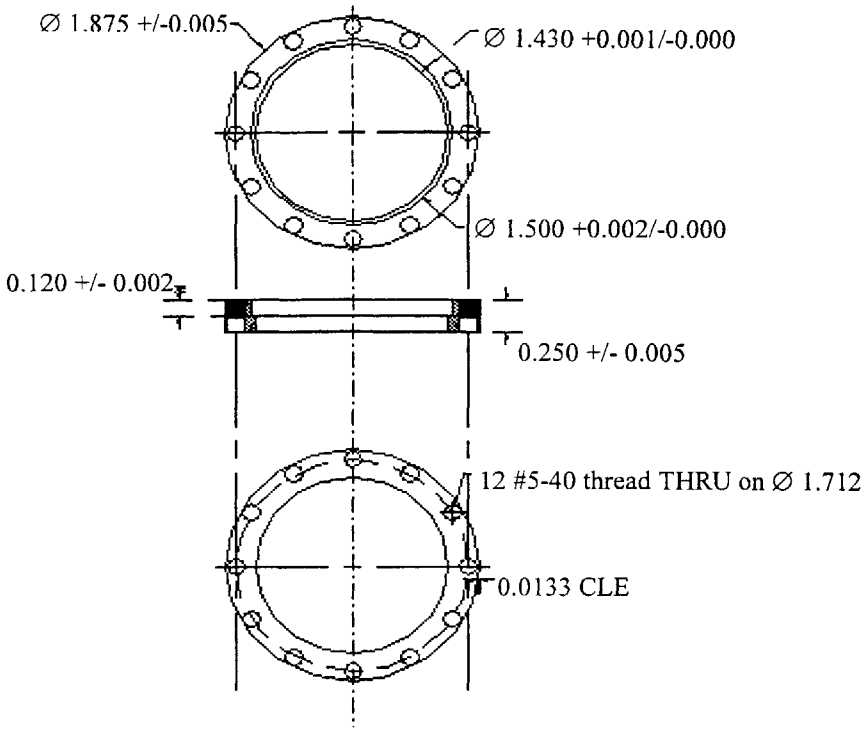

Figure 3.7 - Standard orthographic view of housing end flange

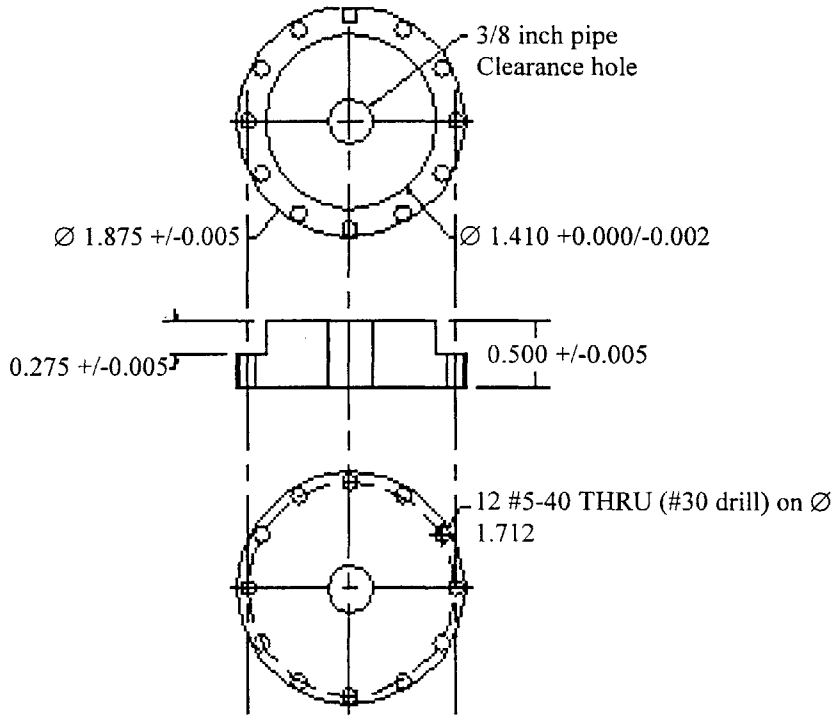

Figure 3.8 - Standard orthographic view of the sealing cap

3.3 Electromagnetic Circuit Assembly

An electromagnetic circuit represented the dynamic link between the mechanical output and the electrical input of the EM valves. The Back Iron and Ferromagnetic Core had to meet the electro-mechanical requirements set forth by the dynamics of the valve. It was also necessary to allow the working fluid to pass through this assembly, which meant incorporating fluid passages into the circuit. In this section, the items that affected the design of the Electromagnetic Circuit Assembly are discussed. The Ferromagnetic Core completed the electromagnetic circuit although for manufacturing purposes it was not considered specifically part of the Electromagnetic Circuit Assembly itself,. The aspects of the Ferromagnetic Core that are linked to the Electromagnetic Circuit Assembly design are discussed here. The incorporation of the Ferromagnetic Core into the Head-Stem-Core Assembly is addressed in the Section 3.6- Head-Stem-Core Assembly Design.

Given the dimensions of the Housing Walls, the electromagnetic circuit was designed so the Back Iron and the Stationary Coil was assembled as a single self-contained unit. The Valve Stem diameter was chosen as $^1/_8$-inch. This set the outer diameter of the Back Iron at 1.43-inches and the inner diameter of the Ferromagnetic Core at $^1/_8$-inch. Between these extremes the Electromagnetic Circuit and Stationary Coil existed.

In designing the Electromagnetic Circuit, the simply electromagnetic circuit schematic of Figure 3.9 was used. This figure denotes a core centerline as line A-A.

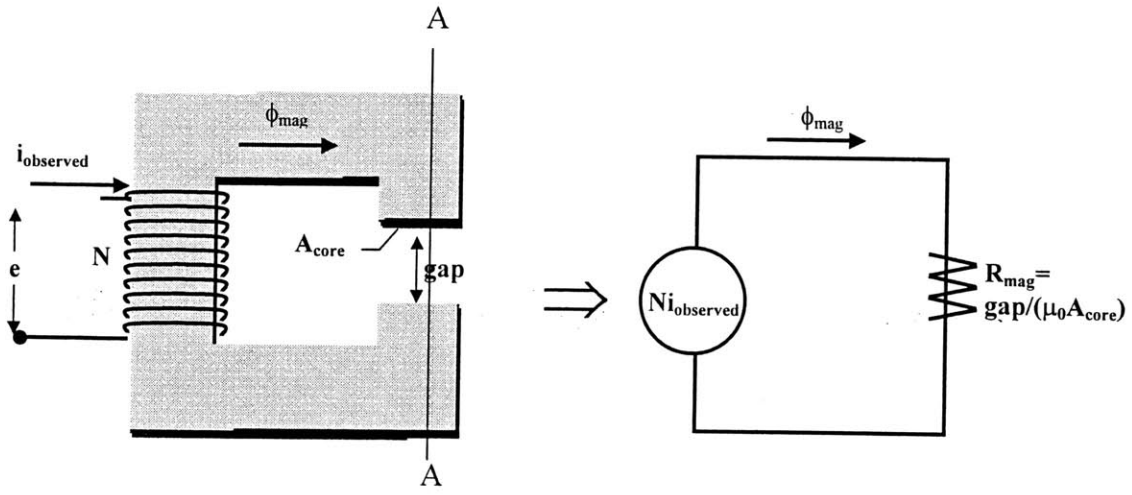

(a) Electromagnetic Circuit

(b) Equivalent Electrical Circuit Analogy

Figure 3.9 - Simple Electromagnetic Circuit Geometry

However, this simplified circuit allowed pertinent geometries, gap and A_{core}, to be specified. In Chapter 6- Electromagnetic Circuit Analysis, the complexities of the actual geometry are addressed.

Equation 3.1 shows how the magnetic force created by the electromagnetic circuit presented in Figure 3.9 is related to the geometry of the circuit. As can be seen, the gap dimensions are the main geometric factors that influence the force created by an electromagnetic circuit. The maximum gap length, gap was set by a maximum possible valve lift of 0.062-inches. This leaves the cross-sectional area of the gap to be specified. This cross-sectional is defined as the cross-sectional area of the Ferromagnetic Core. The inner diameter of the Ferromagnetic Core accommodates the Valve Stem. The outer diameter of the Ferromagnetic Core was chosen as 0.655-inches. This set the required minimum cross-sectional area of all sections of the electromagnetic circuit.

$$F_{mag} = \frac{\mu_0 \cdot A_{core}}{2}\left[\frac{N \cdot i_{observed}}{gap}\right]^2 \qquad \textbf{Eq. (3.1)}$$

The Back Iron was designed as a capped 'Magnetic Cage' that contained the Stationary Coil. Since the helium flow was used to cool the Stationary Coil, the Magnetic Cage concept arose incorporating fluid flow passages through the Back Iron. Figure 3.10 presents an standard orthographic view of the Back Iron. As can be seen, the Back Iron was a hollow cylinder with eight axial-symmetric slots machined through the walls. These slots run the length of the cylinder with a $^1/_8$-inch hoop of ferromagnetic material left at the cap-end of the Magnetic Cage. This hoop of material was to maintain the structural integrity of the component. The surface area of at the minimum radius of the Back Iron's end determined the thickness of the end of a Magnetic Cage.

Two competing factors affected the wall thickness and slot width of the back core: electromagnetic circuit cross-sectional area and fluid passage cross-sectional area. The Ferromagnetic Core defined the minimum electromagnetic circuit cross-sectional area while the minimum fluid passage area was defined by the throat diameter. These two factors were balanced to obtain a wall thickness of 0.10-inch and a slot width of $^1/_{16}$-inch.

Slotting of the cylinders was completed via a milling procedure. A slotting saw and circular indexer were used in this procedure. The $^1/_{16}$-inch slots were first cut into solid ferromagnetic cylinders. The cylinders were then hollowed to the depth set forth by Magnetic Cage length and end thickness. The hollowed depth of the Magnetic Cage was 2.173-inches. This dimension and the thickness of the Magnetic End Cap were chosen to set the length of the Stationary Coil at 2.00-inches. Precision work to square the slots completed the manufacture of a Magnetic Cage.

Similar considerations went into Magnetic End Cap design. The thickness was chosen according to the surface area at the minimum radius of the Magnetic End Cap. The minimum radius was defined so the air gap between the Back Iron and the Ferromagnetic Core was minimized while maintaining a friction-free sliding fit. A close-sliding fit clearance of type RC2 was chosen with a clearance of 0.003-inch on the radius.

The same process that slotted the Magnetic Cages was used to slot the Magnetic End Caps. In the design the Magnetic End Cap slots, it was necessary to direct the fluid past the hoop of material left at the end of the cage and out of the core. This required that

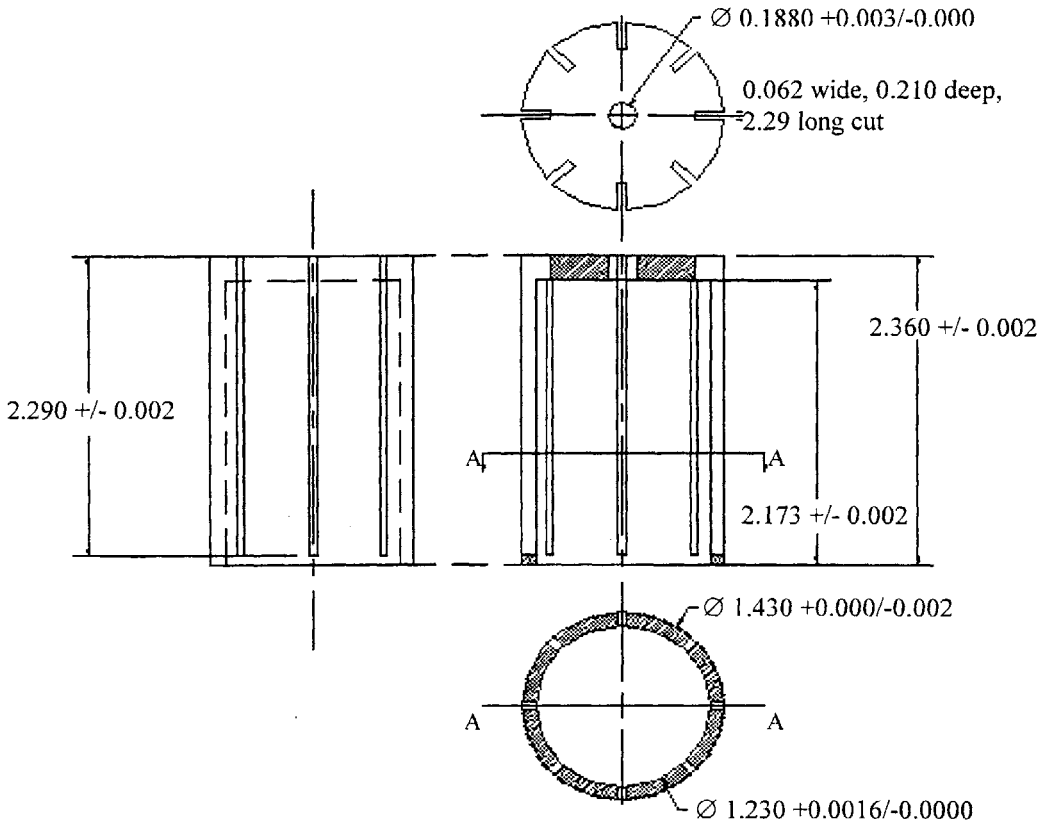

Figure 3.10 - Standard orthographic View of the Magnetic Cage

each slot extend from the outer diameter to a depth of 0.210-inch. Additionally, since the Stationary Coil was to be contained inside of the Magnetic Cage and Magnetic End Cap assembly, it was necessary to incorporate feed through passages for the coil leads. Figure 3.11 depicts the geometry of the End Caps and Figure 3.12 is a photograph of a Magnetic Cage and Magnetic End Cap.

The Ferromagnetic Core length was chosen to ensure the electromagnetic circuit would be completed regardless of its axial position. This length was 2.235-inches.

With the geometry of the Electromagnetic Circuit Assembly specified, the design of the Stationary Coil was a matter of specifying a wire and a coiling process. Once wound, the Stationary Coil would fit tightly inside of the Magnetic Cage assembly. The Stationary Coil's inner and outer diameter was defined by a running fit about the Ferromagnetic Core and a close sliding fit inside of the Back Iron. These dimensions and the hollow length inside of the cage defined the volume available for the Stationary Coil.

As stated previously, copper alloys exhibit non-linear material properties at low temperatures. This characteristic was associated with pure copper's highly temperature dependant thermal and electrical characteristics. As with other pure materials, the

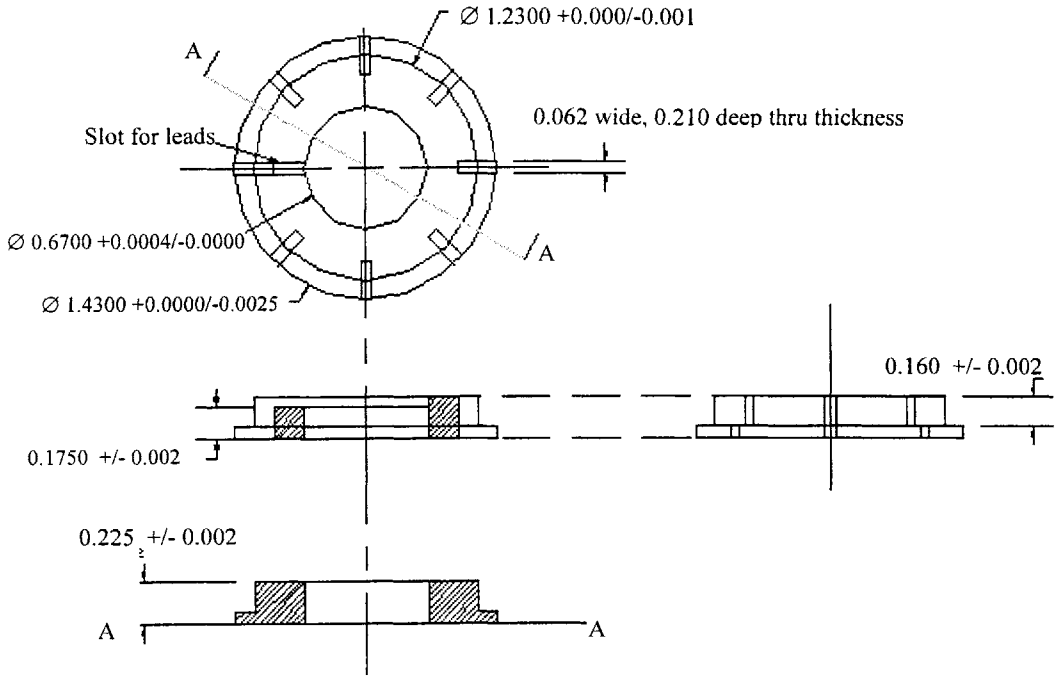

Figure 3.11 – Standard orthographic view of the magnetic end cap

resistivity of copper decreases with increasing temperature. However, with an alloy, the resistivity of the inclusions does not necessarily change at the same rate as the matrix material. The resistivity becomes highly dependent on the free-mean path of an electron in the wire. This was especially true of copper alloys. When the copper alloy reached a low enough temperature, its resistivity was no longer dependant on the properties of copper, but rather on the number of inclusions contained in the alloy. When this occurred, the slope of the change in resistivity of the copper alloy abruptly changed to a nearly constant value. The less pure the copper alloy, the higher the temperature at which this change occurs. It was therefore desired to use highly pure copper for the Stationary Coil. To reduce the cost of the coil, the second most pure commercially available copper wire, OFHC (CDA 10200), was chosen.

With a wire-type specified, the wire diameter and coating were specified. Three competing factors were critical in fully specifying the wire. These were resistivity, manufacturability and power consumption of the Stationary Coil.

In the design of the Stationary Coil, the volume of wire in the coil determined the magnetic flux and thus, the magnetic force generated by the electromagnetic circuit. Equation 3.2 relates magnetic flux to the generated magnetic force.

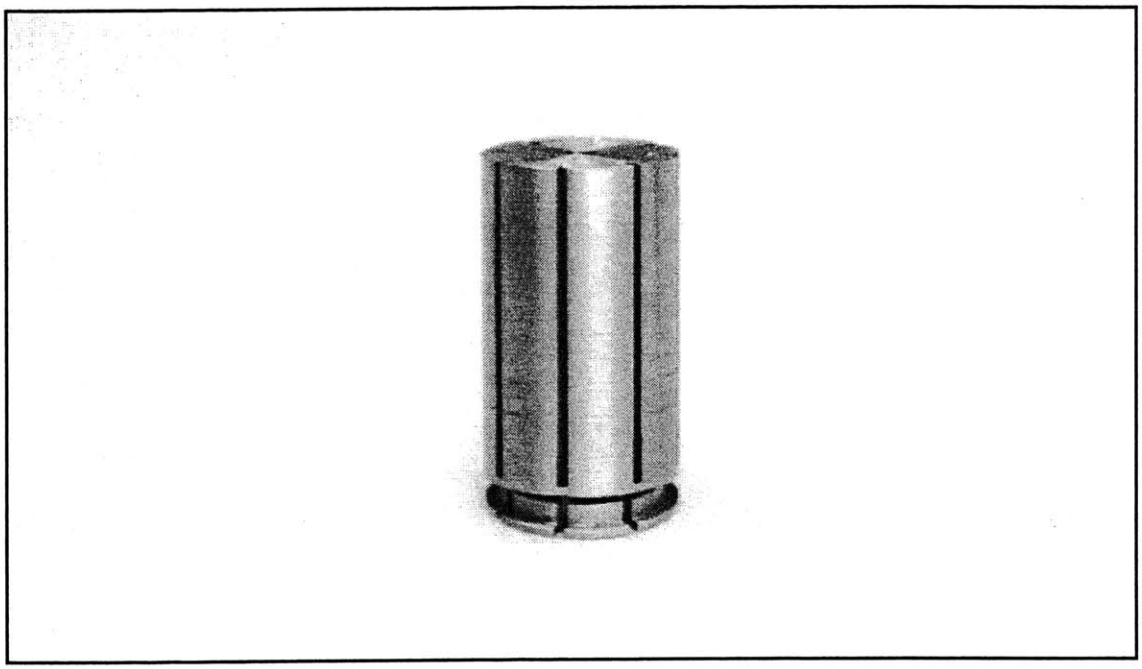

Figure 3.12 - Photograph of Magnetic Cage and End Cap

$$F_{applied} = \frac{\phi_{mag}^2}{2 \cdot \mu_0 \cdot A_{core}} \qquad \textbf{Eq. (3.2)}$$

It was desirable to maximize the amount of copper and minimize the amount of free space and coating in the Stationary Coil. Minimizing free space resulted from carefully rolling the coil as tightly as possible and was, thus, a concern during coil manufacture. Since Formvar is a wire coating commonly used in cryogenic applications, it was selected as the wire coating. It was specified as double build coating to allow the wire to be handled while reducing the possibility of stripping the coating and short-circuiting the Stationary Coil during assembly. Note that μ_0 refers to the permeability of air.

Equation 3.3 gives the relationship between the magnetic flux and the induced current. With air permeability, μ_0, being a material constant and core cross-sectional area and the air gap given by the previously defined geometry of the electromagnetic circuit, this left the product of $N \cdot i_{observed}$ to determine the magnetic flux generated in the circuit. As can be seen, a single-turn coil is capable of achieving the same magnetic flux as a 1000-turn coil. However, the trade off is that the current required to drive the single turn circuit is 1000 times greater than the current required to drive the 1000-turn circuit. Therefore, it was desirable for the wire diameter to be as small as possible to reduce the current, and thus the power consumption, of the circuit.

$$\phi_{mag} = \frac{N \cdot i_{observed} \cdot \mu_0 \cdot A_{core}}{gap} \qquad \textbf{Eq. (3.3)}$$

On the other hand, as shown in Equation 3.4, the resistivity increases with decreasing wire diameter. According to Equations 3.5, an increase in required current and, thus, an increase in power consumption occurs as resistivity increases.

$$R_{coil} = 2 \cdot \pi \cdot \rho \cdot r_{av,coil} \cdot N \qquad \textbf{Eq. (3.4)}$$

$$V_{coil} = I_{coil} \cdot R_{coil}$$
$$Power_{Elect} = I_{coil}^2 \cdot R_{coil} \qquad \textbf{Eq. (3.5)}$$

An additional consideration was that as wire diameter decreased, difficulty of manufacture increased. As the wire diameter went down, less material was available for plastic deformation. The wire appears to have less strength with decreasing diameter. This posed an additional difficulty in design. The wire required sufficient strength to withstand not only the tension of rolling a coil but also the compression of the layers of wire in the coil.

Given these considerations, a 22.5 gage OFHC (CDA 10200) wire was chosen. The coating was completed as a first run by SuperCON. The coils were manufactured in-house on a variable speed lathe set up with a wire-tensioning and wire-cleaning device.

When winding the Stationary Coil, the geometry of the magnetic circuit was held with a specially designed mandrel. To ensure the lead placement, the mandrel also incorporated measure that matched the geometry Magnetic End Cap. This allowed each coil to be rolled and counted by hand. For ease of removal from the mandrel, the coils were fit with thin polyurethane washers at each end and a polyurethane insert at the inner diameter. Each successive layer was coated and free space in the Stationary Coil was filled with clear Stycast® Epoxy.

To complete the coil a final coating of black Stycast® Epoxy was cured to the outer surface of the coil. The entire Stationary Coil was then turned on a lathe to remove the excess black epoxy and ensure the outer diameter. The final diameter of the coil met a sliding fit clearance within the Magnetic Cage. This allowed the Stationary Coil to be inserted and centered inside of the Magnetic Cage. The Stationary Coil, Magnetic Cage and Magnetic End Cap were aligned and welded together as a single assembly.

3.4 Multi-Leaf Flexure Assembly Design

In order to achieve a design with no frictional components, the Head-Stem-Core Assembly had to remain centered in the Valve Assembly throughout the motion of the valve. As Section 3.6- Head-Stem-Core Assembly Design describes, the Valve Stem and Valve Head were manufactured as a single assembly, which was clamped to the Ferromagnetic Core. The clamping force was provided via the Compression Spring Assembly (described in the Section 3.5- Compression Spring Assembly Design). The motion of the valve was limited to the Head-Stem-Core Assembly and the Valve Head position was controlled with the travel of the Ferromagnetic Core inside of the electromagnetic field created by the Stationary Coils. The Ferromagnetic Core and Valve Stem are held centered in the Stationary Coil orifice via thin Multi-leaf Flexure Assemblies.

A flexure is typically a flat, thin, circular, non-linear spring that is commonly used in space-constrained applications. With a flexure, different spring characteristics can be achieved in two orthogonal directions, radial and axial. Thus, axial and radial stiffness were the two factors that influenced the design of these Multi-Leaf Flexure Assemblies. It was desired to eliminate most non-linearities in analysis and testing processes; therefore the flexures were designed to minimize their impact on the valve operation. The flexures added negligible axial loading and they provided sufficient radial stiffness to prevent the Ferromagnetic Core from being offset inside of the Back Iron by the electromagnetic field inside of the radial air gaps created by clearances.

Since the Head-Stem-Core assembly must move as if it were a single unit, the assembly traveled inside two primary orifices. To complete the electromagnetic circuit, the Ferromagnetic Core traveled inside of the lower orifice of the ferromagnetic Back Iron. As stated, the air gap at this interface was reduced with a close-sliding fit clearance of type RC2, which introduced and air gap of 0.003-inches on the radius of the orifice. The Valve Stem traveled in the upper orifice of the Back Iron. The clearance at this orifice is similar to that of the lower orifice. This 0.003-inch clearance was used to specify the amount of axial stiffness necessary to prevent the core from being offset inside of the Back Iron.

Principals of electromagnetism were applied to determine the possible axial loading applied to the Multi-leaf Flexure Assemblies. If the Ferromagnetic Core were to offset in the orifice by the maximum of 0.003-inches, an unequal electromagnetic field was set up inside of the gap, which induced an uneven force acting on the Ferromagnetic Core. The maximum offsetting occurred when the ferromagnetic circuit was at magnetic flux saturation and the core was in a fully off-centered position. For most common carbon steels magnetic saturation occurs at a value of approximately 1.8 Teslas.

The simple schematic shown in Figure 3.13, describes the geometry used for determining the offsetting electromagnetic force. In this position, the gap geometry varied in a sinusoidal fashion, the maximum offsetting force occurred at the point when the gap was at its maximum. The governing relationship behind determining this off centering force related the magnitude of the electromagnetic field to the induced potential in the gap. This potential was then translated to a force via Equation 3.6.

$$F_{offset} = \frac{A_{circum}}{2}\left[\frac{B_{sat}^2}{\mu_0}\cdot\int_0^{\pi}\sin(\theta_c)d\theta_c + \mu_0\cdot(N\cdot i_{\pi,sat})^2\int_{\pi}^{2\pi}\frac{\sin(\theta_c)}{gap(\theta_c)}d\theta_c\right] \qquad \textbf{Eq. (3.6)}$$

The term i_{sat} was defined according to Equation 3.7. Equations 3.6 and 3.7 defined the force that each the Multi-leaf Flexure Assemblies in each EM valve had to overcome to maintain the core in the centered position. From the specified geometry, this force was 9.3 lbf.

$$i_{\pi,sat} = \frac{B_{sat}\cdot gap(\pi)}{N\cdot\mu_0} \qquad \textbf{Eq. (3.7)}$$

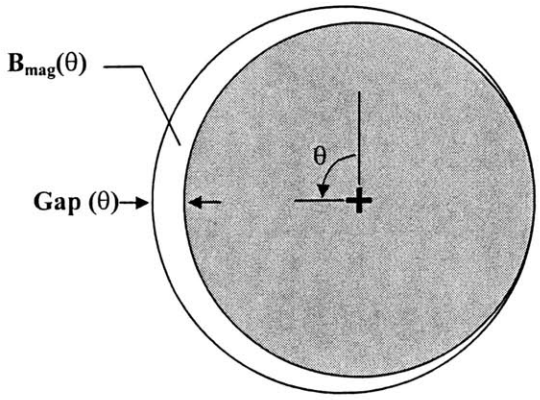

Figure 3.13 - Offsetting geometry to determine offsetting force

The second factor affecting the geometry of the flexure design was the maximum axial valve travel. The Valve Head had a maximum of 0.031-inches of lift with each flexure having a positive and negative axial deflection of one-half the valve travel, 0.0155-inch. Dynamically speaking, the flexures had a negative deflection of 0.0155 inch when the valve was closed. At one-half the distance of the valve travel, the flexures passed through their neutral position and reached a maximum positive deflection of 0.0155-inch when the valve head reached its full-open position. To insure that the internal stresses associated with the axial flexure deflection were within material constraints, each flexure was designed with a safety factor of 2 with respect to the axial

deflection. Thus, for design purposes maximum positive and negative axial deflection was considered as 0.031-inches.

The final consideration in flexure design was applying an appropriate radial geometry. Several configurations were considered and analyzed. These concepts included symmetric, straight-spoke radial patterns and symmetric pre-stressed or pre-deformed axial patterns. In these concepts, a single flexure was to be used on either side of the Electromagnetic Circuit Assembly. In analysis, these patterns were modeled as short thin beams. This resulted in beam deflections on the order of three- to six-times the thickness of the beam. Analysis proved that the stress induced at these deflections were well beyond that of material constraints. From this analysis, it was determined that the length of the beams must be increased to reduce the stresses at maximum deflection.

Increasing the beam length was accomplished by applying curved beam geometry to the flexures. This allowed the beam length to be increased to the circumference of the radial clearance between the Housing Wall and the Valve Stem. However, this configuration also created an uneven radial stiffness. Three-leaf flexure assemblies were chosen as the minimum number of flexures required to provide symmetric radial stiffness within each assembly. A Multi-leaf Flexure Assembly was located above and below the Electromagnetic Circuit Assembly.

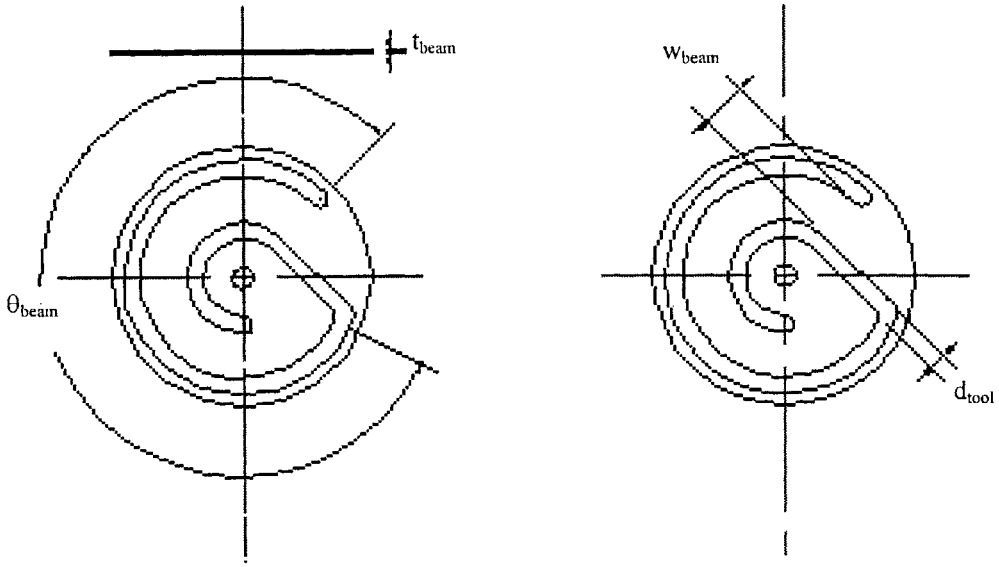

Figure 3.14 - Un-Dimensioned Radial Geometry

The radial geometry of the flexures was chosen so that they were manufactured in-house using traditional manufacturing techniques, i.e. milling, drilling and turning. This meant minimizing number of tooling paths and minimizing the changes in direction of the cutting pattern. This was achieved by incorporating simple geometric shapes, concentric radial patterns and standard angle specifications in the design. As shown in Figure 3.14, a single flexure was as a circular beam spanning between the moving valve stem and the stationary housing. Each flexure was manufactured of a single sheet of spring steel. Milling the required pattern into the spring steel formed a curved thin beam. This pattern utilized a single tool path and limited changes in the tool direction two circular cuts and a single diagonal cut.

Each Multi-Leaf Flexure Assembly consisted of three single flexures stacked with a 120° of relative rotation. 0.035-inch spacers were placed between each single flexure. The spacer thickness was chosen to accommodate the maximum positive and negative axial deflections without allowing the flexures to interfere with one and other. Multi-leaf Flexure Assemblies were located above and below the moving Ferromagnetic Core. At the inner diameter, the flexures were held clamped to the Head-Stem-Core Assembly via the Compression Spring Assembly. They were also clamped at the outer diameter to the Ferromagnetic Cage via the Belleville springs.

Given the above-specified geometry, required deflections and applied forces, each flexure was analyzed as a thin-curved beam. Static curved beam analysis allowed the necessary dimensions of this thin-beam configuration to be defined. In the analysis, Excel and MathCad were used to vary the control variables of beam thickness, t_{beam}, beam width, w_{beam} and beam span,θ_{beam}. Each flexure was to be made of hardened 401 stainless spring steel. There were three thickness of spring steel available for use in this design, 0.006-, 0.010- and 0.012-inches. The radial deflection of the end of the beam was specified as the maximum offset allowed inside of the orifice, 0.003-inches and the maximum axial deflection was taken as 0.031-inches, one-half the distance of maximum valve travel including safety factor. The two methods of analysis were used in specifying these dimensions are described below.

First, a beam width was determined for each of the three thicknesses available. Using the above force, a curved beam analysis with deflection in the plane of curvature was undergone. The stiffness of a single flexure for each thickness was determined from this analysis. Figure 3.15 shows the schematic of a curved beam loaded in the plane of curvature used for this static analysis. Material properties for 401 Stainless Steel were used in conjunction with Equations 3.8 to determine the stiffness of each flexure for varying beam spans, θ_{span}. Equation 3.8 was developed from Castigliano's Theorem for strain energies and Figure 3.15 defines all geometries.[6]

$$F_{Radial} = \frac{2\delta_{offset} E_{ss} A_b}{R_b}\left[\left(\frac{R_b}{ecc} - 1\right)\left(\theta_b - \cos\theta_b \sin\theta_b\right) + \frac{CE_{ss}}{G_{ss}}\left(\theta_b + \cos\theta_b \sin\theta_b\right)\right]^{-1}$$

Eq. (3.8)

C is a correction factor used for a rectangular beam and e is the eccentricity of the curved beam.

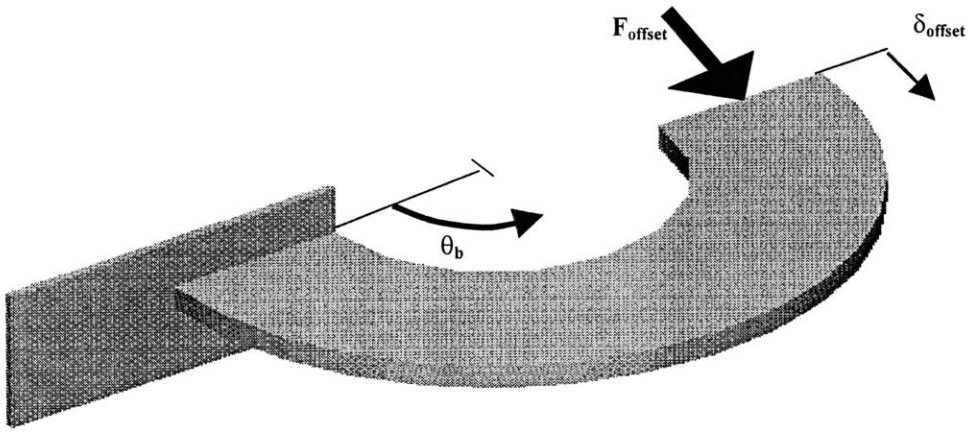

Figure 3.15 - Schematic of a curved beam loaded in the plane of curvature used for this static analysis

The beam thickness, t_{beam} and beam width, w_{beam} were then varied. Given the space available for tooling and the selected geometry, beam widths were chosen to accommodate end mill diameters, denoted d_{tool} on Figure 3.14, of $^1/_{16}$-, $^3/_{32}$-, $^1/_8$ and $^5/_{32}$-inch. This provided four possible radial stiffnesses for each thickness available.

Each flexure carried more than one third of the possible offsetting load. Once the combinations of these two variables were calculated, the optimal combination was chosen by analyzing the stresses induced in the flexure via the radial deflection that arises during valve travel. Details of the algebra associated with these calculations can be found in Appendix A- Flexure Analysis.

The second part of the analysis used formulas available in Roark and Young's Formulas for Stress and Strain[7], to analyze the maximum stresses induced in the flexure at maximum deflection. This analysis proved more complex due the geometry of the system. Since the flexures were clamped in the center and at the outer edge, several boundary conditions were introduced. Three cases were chosen and moments, torsions and forces were equated according to the rules of superposition. The maximum stresses induced were found.

The three cases arose from a curved beam loaded perpendicular to the plane of curvature. Each case is briefly outlined next. The case description was defined by the beam end conditions and the type loading applied to the beam. Refer to Figure 3.16 for the free-body schematic of a beam loaded perpendicular to the plane of curvature. Applicable deflection, rotation and twist equations are presented. Deflection, δ_i, was normal to the plane of curvature. Rotation, Θ_i, was in the plane of the bending moment.

Twist, Ψ_i, was in the plan of torsional reaction. All constants, $C_{\alpha i}$ are defined in Appendix A- Flexure Analysis for the following the cases.

It was noted that this analysis was for thin-beams and only approximated the behavior of a plate or shell of revolution. For the purposes of this analysis, this approximation was sufficient and an adequate factor of safety was incorporated into the final flexure design.

Case 1- Curved beam with one end fixed and one end free. The beam is loaded at the end.

$$\delta_1 = \frac{-F_{axial} R_b^3}{E_{ss} I_{xx}} \left(C_{\alpha 6} \sin\theta_b - C_{\alpha 9}(1-\cos\theta_b) - C_{\alpha 3} \right)$$

$$\Theta_1 = \frac{F_{axial} R_b^2}{E_{ss} I_{xx}} \left(C_{\alpha 6} \cos\theta_b - C_{\alpha 9} \sin\theta_b \right) \qquad \textbf{Eq. (3.9)}$$

$$\Psi_1 = \frac{F_{axial} R_b^2}{E_{ss} I_{xx}} \left(C_{\alpha 9} \cos\theta_b + C_{\alpha 6} \sin\theta_b \right)$$

Case 2- Curved beam with one end fixed and one end free. The beam is loaded with a bending moment at the free end.

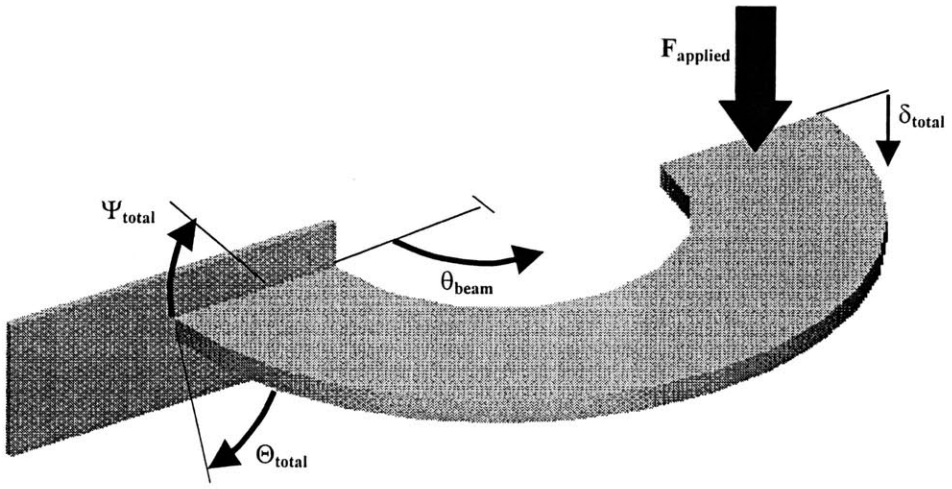

Figure 3.16 - Free-body schematic of a beam loaded perpendicular to the plane of curvature

$$\delta_2 = \frac{M_0 R_b^2}{E_{ss} I_{xx}} \left(C_{\alpha 4} \sin\theta_b - C_{\alpha 7} (1 - \cos\theta_b) - C_{\alpha 1} \right)$$

$$\Theta_2 = \frac{M_0 R_b}{E_{ss} I_{xx}} \left(C_{\alpha 7} \sin\theta_b - C_{\alpha 4} \cos\theta_b \right) \qquad \textbf{Eq. (3.10)}$$

$$\Psi_2 = \frac{-M_0 R_b}{E_{ss} I_{xx}} \left(C_{\alpha 4} \sin\theta_b + C_{\alpha 7} \cos\theta_b \right)$$

Case 3- Curved beam with one end fixed and one end free. The beam is loaded with a twisting moment (torque) at the free end.

$$\delta_3 = \frac{T_0 R_b^2}{E_{ss} I_{xx}} \left(C_{\alpha 5} \sin\theta_b - C_{\alpha 8} (1 - \cos\theta_b) - C_{\alpha 2} \right)$$

$$\Theta_3 = \frac{-T_0 R_b}{E_{ss} I_{xx}} \left(C_{\alpha 5} \cos\theta_b - C_{\alpha 8} \sin\theta_b \right) \qquad \textbf{Eq. (3.11)}$$

$$\Psi_3 = \frac{-T_0 R_b}{E_{ss} I_{xx}} \left(C_{\alpha 8} \cos\theta_b + C_{\alpha 5} \sin\theta_b \right)$$

Using Equations 3.9-3.11 and all the induced boundary conditions, the rules of superposition for thin-beam analysis were applied. The total deflection, rotation and twist of the beam was a composite of the deflection, rotation and twist of each of the above cases. Total deflection was half the distance of the maximum valve travel. Total Free end rotation, Θ and total free end angle of twist, Ψ were zero. Therefore, the boundary conditions for the beam are stated in Equations 3.12 as follows:

$$\begin{aligned} \delta_{total} &= \delta_1 + \delta_2 + \delta_3 \\ 0 = \Theta_{total} &= \Theta_1 + \Theta_2 + \Theta_3 \\ 0 = \Psi_{total} &= \Psi_1 + \Psi_2 + \Psi_3 \end{aligned} \qquad \textbf{Eq. (3.12)}$$

Using Excel and these boundary conditions, various applied forces were input until the desired boundary conditions were met. A reactionary shear, R_{shear}, bending moment, M_{react} and torsional moment, T_{react} were induced by this applied force and the boundary conditions. Details of the algebra associated with these calculations are found in Appendix A- Flexure Analysis. These reactions were used along with Equations 3.13 to determine the stresses introduced in the flexure at the axial deflection associated with the full-opened and full-closed positions of the valve plus the designed safety factor. The thickness of the flexure was chosen to maintain all of these stresses below material constraints.

$$\sigma_{bending} = \frac{M_0 y}{I_{xx}}$$

$$\tau_{torsion} = \frac{T_0 (w_{beam}/2)}{J_{xx}} \qquad \text{Eq. (3.13)}$$

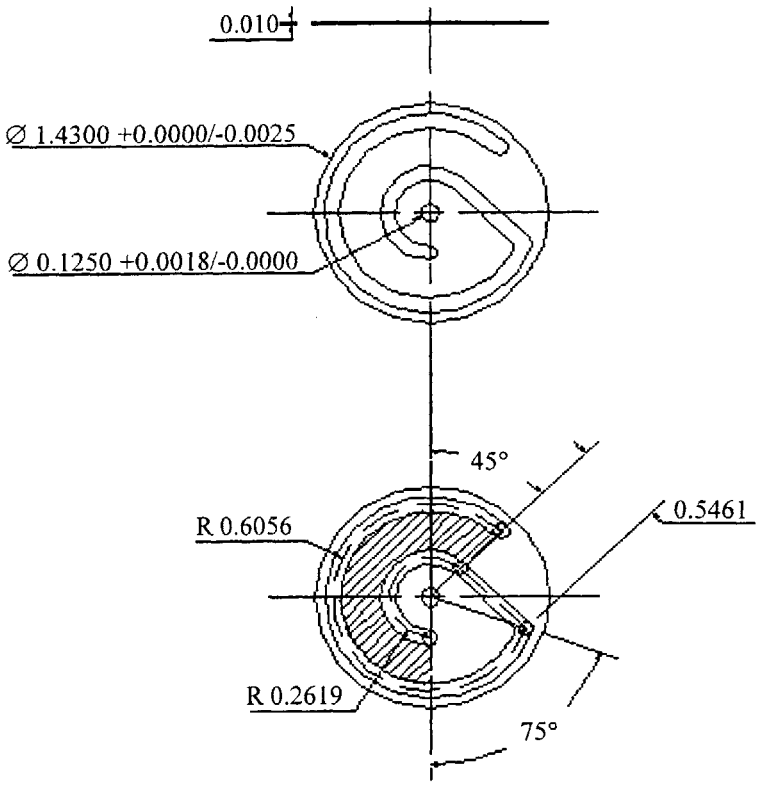

Figure 3.17 - Final Flexure Design, with all dimensions included

The final flexure design, including the chosen dimensions of t_{beam}, w_{beam}, θ_b and d_{tool}, appears in Figure 3.17. As noted, the beam width was 0.25- inches, beam thickness was 0.010-inches and beam span was 300° of rotation. This incorporated a tool diameter of $^3/_{32}$-inch. These dimensions arose from the optimization of the preceding analysis. Figure 3.18 describes the state of stress of the flexure throughout the span of the beam for the maximum valve travel plus safety factor. For this configuration the maximum bending stress, $\sigma_{bending}$ was found to be approximately 9 ksi and the maximum torsional shear stress, $\tau_{torsion}$ as approximately 7 ksi. Both values were well below the elastic limits of 401 Stainless Steel. This configuration also provided more than 11 lbf of lateral stiffness for each three-leaf flexure assembly.

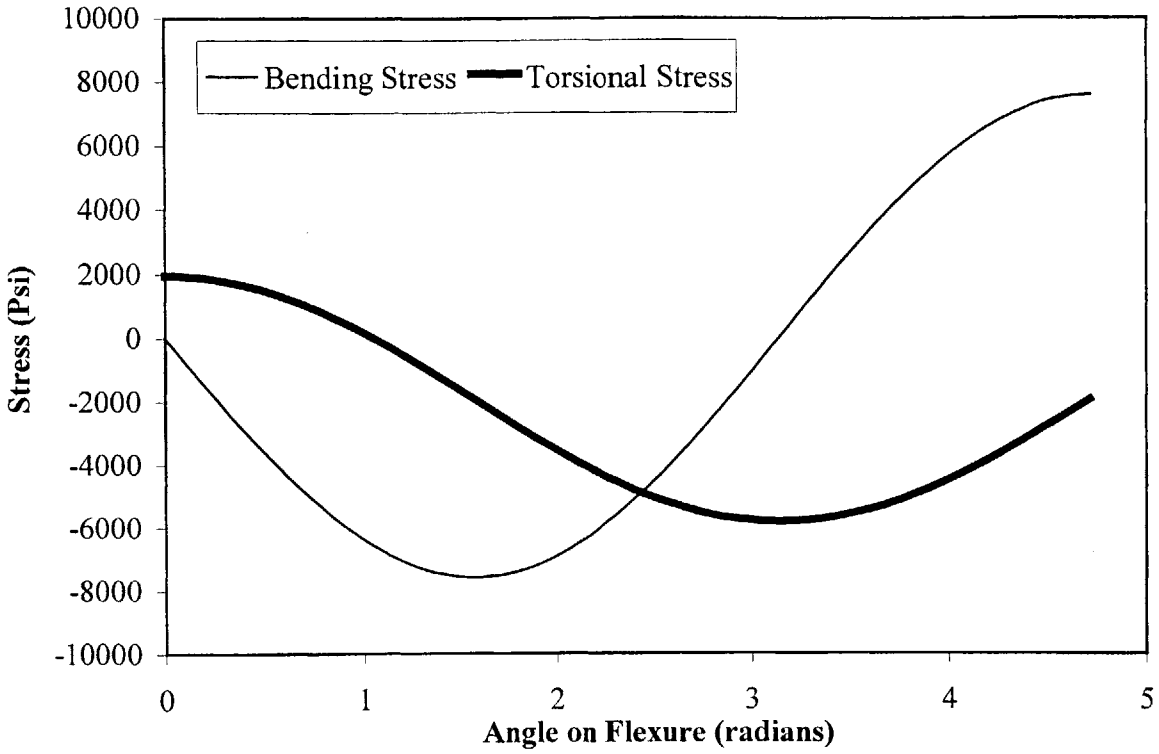

Figure 3.18 - State of stress in the flexure throughout beam span for maximum valve travel plus safety factor.

The Multi-leaf Flexure Assemblies were designed to have sufficient radial stiffness to overcome the radial instabilities associated with the electromagnetic force exerted on the stem at the maximum possible off-center position. The valve stem had a standard sliding fit clearance in the hole in the back core of 0.003-in on the radius. An electromagnetic flux existed in this gap. The flexures stiffness was selected so the net flexure force of the Multi-leaf Flexure Assemblies returned the valve to a centered position when offset radially by 0.003-inch. This design was refined by a stress analysis of a flexure under the conditions of maximum deflection. Figure 3.17 presents the final single flexure design and Figure 3.19 shows a photograph of a flexure as-manufactured.

To finalize the Multi-leaf Flexure Assemblies, Inner Spacers were designed to clamp the flexures to the stem of the Head-Stem-Core assembly and Outer Spacers were designed to maintain this clearance at the Housing Wall. As stated, the spacers had a minimum thickness of 0.035-inches. The width of the spacers was chosen to provide sufficient clamping area. Figure 3.20 shows the dimensions of the three types of spacers used.

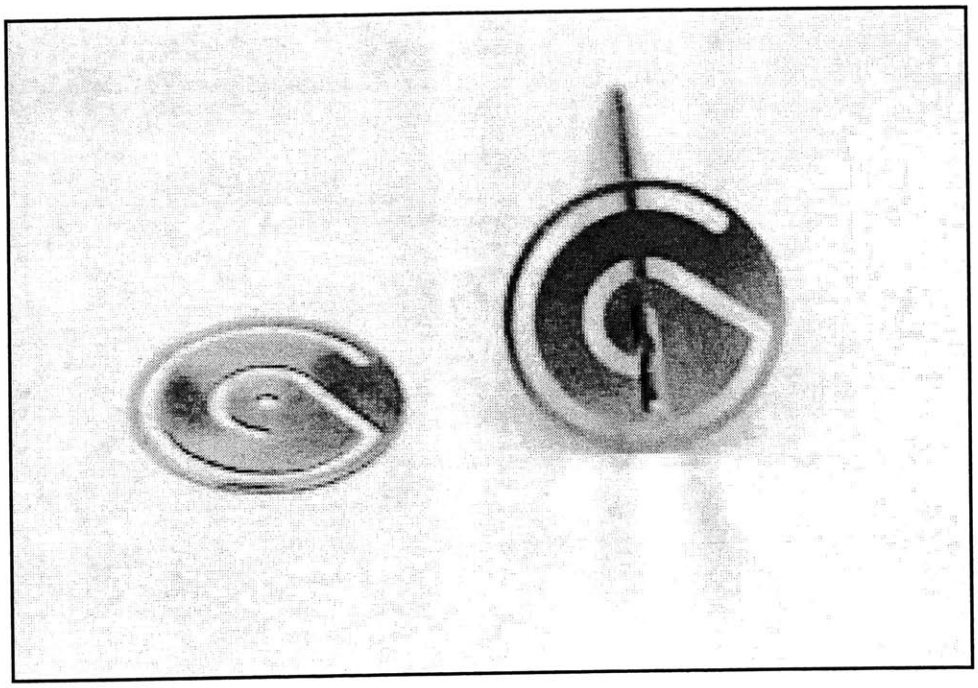

Figure 3.19 – Photograph of Single Flexure

Assemblies above and below the Ferromagnetic Core were completed by welding parts of adjacent sections to the assemblies. The stack located above the core was welded to the Valve Throat section, shown in Figure 3.21. Dimensions for this component were chosen in accordance with the inner diameter of the throat section of the housing assembly and the desired 3/8-inch throat diameter. The stack located below the core was welded to the outer compression spring platform, which is described in Section 3.5-Compression Spring Assembly. In reality, the outer compression spring platform was part of the lower flexure stack assembly; however its design is presented along with Section 3.5-Compression Spring Assembly. Figure 3.22 shows a cross-sectional view of how these stacks are ordered in each assembly. Figure 3.23 and 3.24 provide photographs of the upper and lower Multi-leaf Flexure Assemblies respectively.

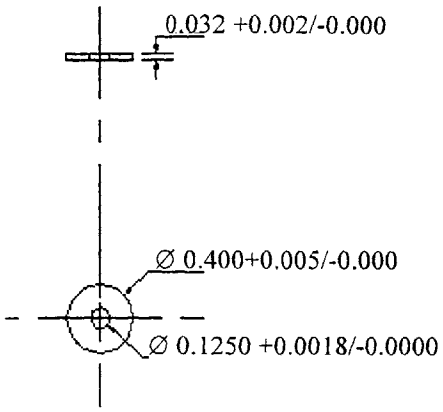

(a) Small inner spacer at Valve Stem

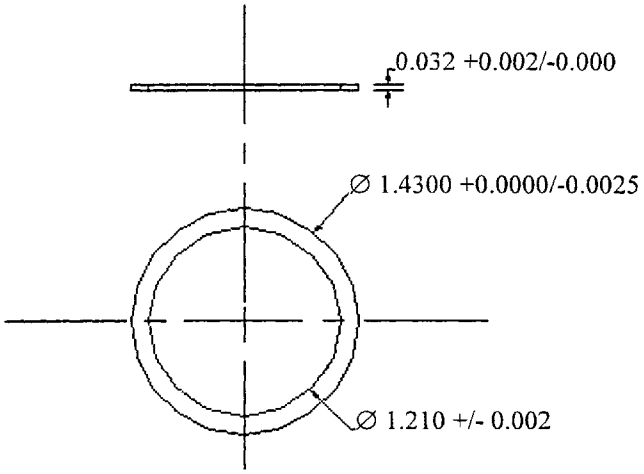

(b) Thin outer spacer at Housing Wall

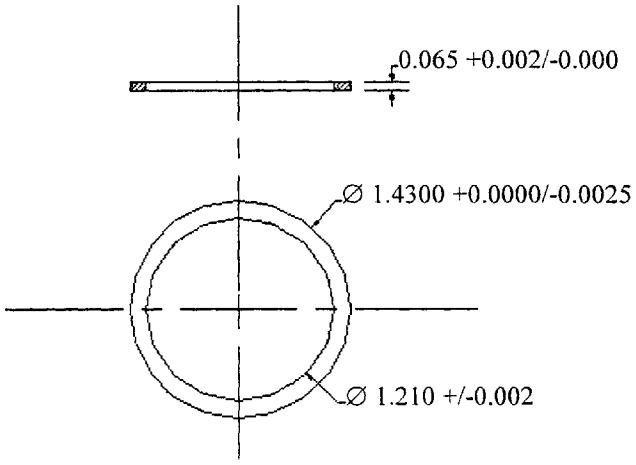

(c) Thick outer spacer at Housing Wall

Figure 3.20 – Three Types of Spacers Used

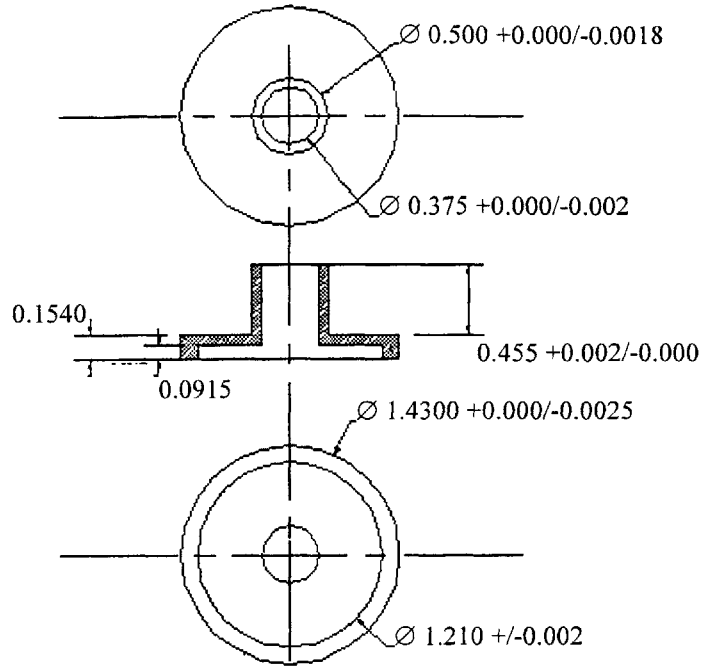

Figure 3.21 – Standard orthographic View of Valve Throat Section

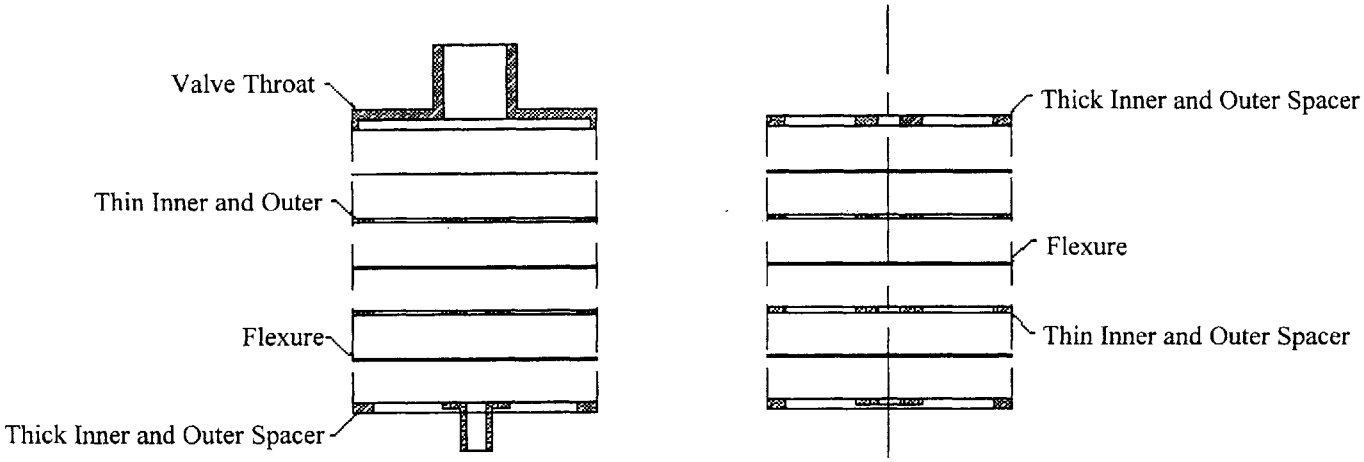

(a) Stacking order of top Multi-leaf Flexure Stack

(b) Stacking order of bottom Multi-leaf Flexure Stack

Figure 3.22 – Cross-sectional view of stacking order

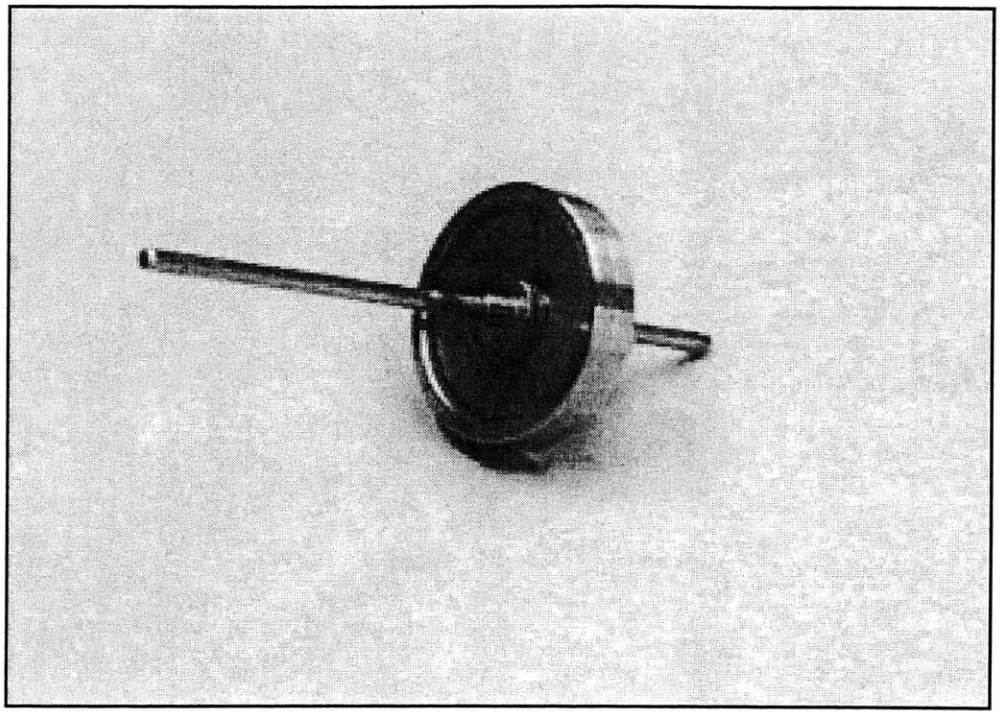

Figure 3.23 – Photograph of Upper Multi-Leaf Flexure Assembly

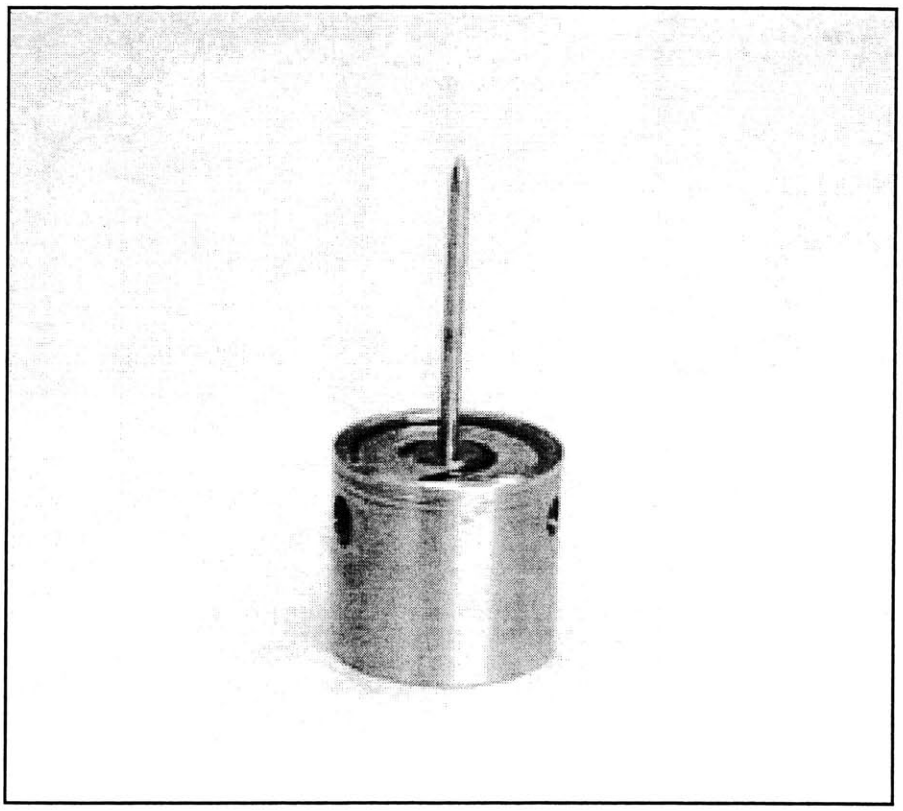

Figure 3.24 – Photograph of Lower Multi-leaf Flexure Assembly

3.5 Compression Spring Assembly Design

To fully specify the length of the Valve Assembly, the dimensions of the final compression spring assembly had to be specified. This entailed choosing an adequate compression spring and designing the two platforms, which held it in place. Although the outer compression spring platform appeared as part of the Multi-leaf Flexure Assembly and the inner compression spring platform appears in the next section as part of the Head-Stem-Core Assembly, for the purposes of this thesis, they appear in this section as a separate assembly. Spring selection and the platform design are detailed here.

As has been stated, these valves were to require no magnetic force to keep them in the closed position. Thus, a compression spring was chosen to serve two purposes. First, it held the valve closed with sufficient force to ensure that the valve seats and seals properly. Second, it acted as the force to return the valve to the closed position once the system low pressure was reached.

The first qualification was met by ensuring that the compression spring exerted sufficient force to allow a Kel-F® valve seat to seal against helium leaks. From work completed by Miller and Brisson [16], the necessary seating force, given the seating area was determined. Data from that study showed that if the force applied to the seat at room temperature allowed the Kel-F® to creep, then a tight low-temperature seal was achieved. At room temperature, with no electrical input to the Stationary Coils, the cold EM valves were closed by the compression spring with sufficient force to deform the Kel-F® seat and shape the seating surface. Even at low temperatures, this deformation provided a tight seal with leak rates well below tolerable limits. Thus, a compression spring that exerted more than 10 lbf in its initial position was chosen.

The spring was to be initially compressed 0.800-inches. From this dimension, an end ground, carbon steel, SPEC linear compression spring was chosen to provide the required 10 lbf of force. The spring chosen had a wire diameter of 0.059-inch with a coil diameter of 1.50 inches. Its spring constant was 15.0 lb/in (2630 N/m) and it free length was 1.5-inches (0.0381-m). When compressed to 0.800 inches (0.0203-m), this spring exerted 10.5 lbf (46.8 N) on the platforms.

The platforms were designed around the dimensions of the spring. Figure 3.1 presented the general configuration of the Valve Assembly. From this, it can be seen that the compression spring was held between the flanges of two platforms. One end of the spring was held at the Inner Compression Spring Platform, which moved with the valve action. The other end was held against the Outer Compression Platform, which acted as a stationary surface.

The Inner Compression Spring Platform provided tension to the valve stem as well as set the final length of the Valve Stem. From the bottom of the valve seat to the end of the stem, the length of the Valve Stem was 3.93-inches. The Inner Compression Spring Platform also served as the actuator that transferred the magnetic force acting in the gap of the electromagnetic circuit to the compression spring. This component was allowed to move with the motion of the valve and thus, appears as part of the Head-Stem-Core Assembly. The Inner Compression Spring Platform appears in Figure 3.25.

The Outer Compression Spring Platform served three purposes in the Valve Assembly. It acted as the stationary platform, as the final component adding to the length

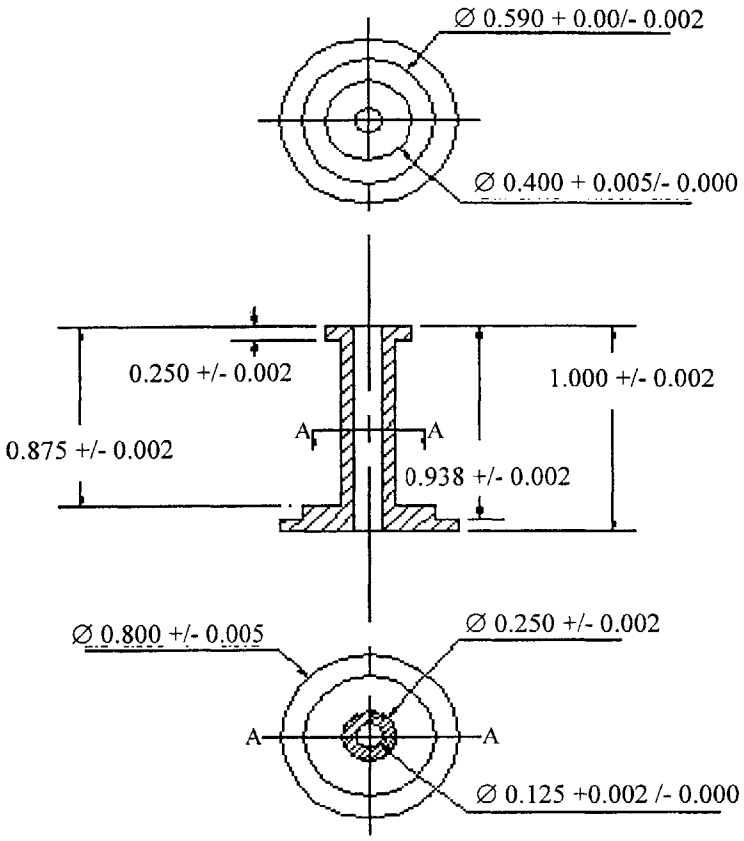

Figure 3.25 - Standard orthographic View of the Inner Compression Spring Platform

of the valve and as the final passageway for the wire leads between the Back Iron and the flow-thrus.

The Outer Compression Spring Platform provided the second surface that held the spring in compression. In order for this platform to act as a stationary surface it was held tightly against the lower Multi-leaf Flexure Assembly. As depicted in the previous section, this component was welded to the lower stack of the Multi-leaf Flexure Assemblies.

As the final component adding to the length of the Valve Assembly, the Outer Compression Spring Platform set the length of the Housing Wall as 4.375-inches. As seen in Figure 3.1, it acted as the surface that mated to the Belleville springs. Thus, the wall thickness of the Outer Compression Spring Platform was chosen to ensure that the Belleville springs (SPEC 1.375 inch diameter Belleville springs) would be held in compression between the end of the Outer Compression Spring Platform and the Housing

Cap (see Section 3.2 Housing Assembly Design). See Figure 3.26 for an standard orthographic view of the Outer Compression Spring Platform.

To ensure that the compression spring is held centered in the assembly, flanges the width of the diameter of the spring wire were machined into the two platforms. Machining of these components was completed on a horizontal lathe. Upon final assembly, feed-thrus for the coil wires were positioned and machined in via a milling operation.

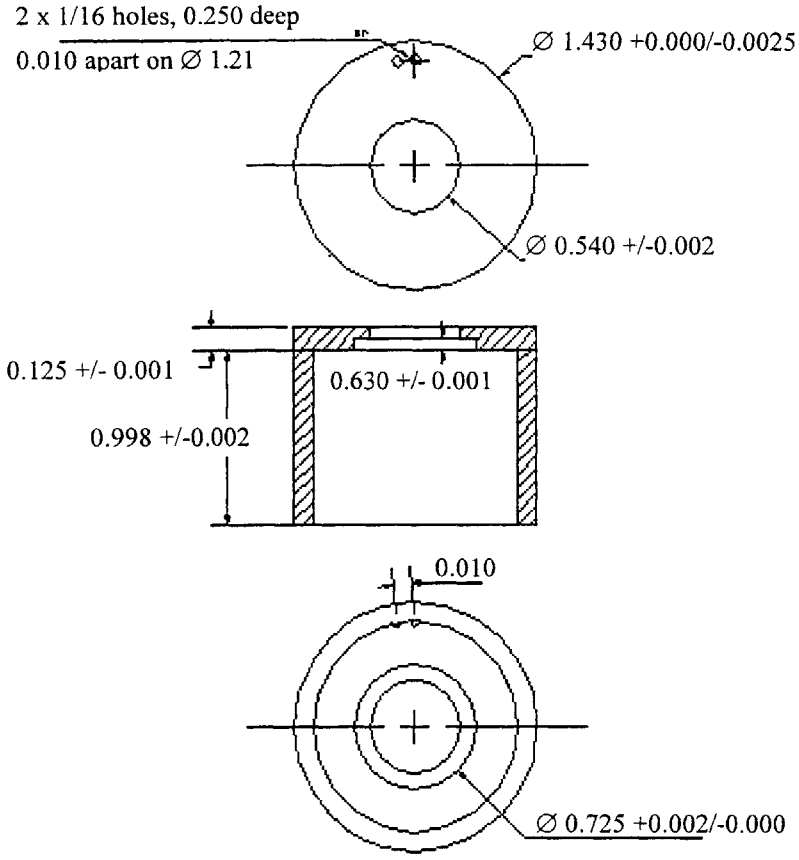

Figure 3.26 - Standard orthographic View of the Outer Compression Spring Platform

3.6 Head-Stem-Core Assembly Design

The only moving assembly of the EM valve was the Head-Stem-Core Assembly. This assembly consisted of the Valve Head, the Valve Seat, Seat Clamp, Core Clamp and the Valve Stem. Although presented in previous sections, the Ferromagnetic Core and the Inner Compression Spring Platform were part of this assembly. This section discusses the procedure for specifying the dimensions of this final assembly and some of the manufacturing procedures used to produce these parts. The Inner Compression Spring platform was described in Section 3.5- Compression Spring Assembly Design. The dimensions of the Ferromagnetic Core were set forth in Section 3.3- Electromagnetic Circuit Design. In essence, the Housing Assembly held all the 1.43-inch diameter components together via the Belleville springs. The Valve Stem held all the 1/8 -inch diameter components together by the 5-40 nut on the threaded end of the valve stem. The dynamic link between these two diameters was the Multi-Leaf Flexure Assemblies that held the Valve Stem centered. Manufacture and incorporation of the Ferromagnetic Core into the Valve Assembly are presented here.

Given the geometry of the Chamfers in the Cold End of the Cold Head, the thickness of the Valve Head and Valve Seat were specified. At the point of maximum travel, the valve head extended to 0.031-inch below the surface of the Cold Head Cylinder Cap. The total thickness of the Valve Head including the thickness of the Valve Seat was set at 0.085-inch. To ensure the strength of the Valve Head, its thickness was set at 0.050-inch with the Kel-F® Valve seat being 0.035-inch thick.

To simplify the manufacture of the Head-Stem-Core Assembly, the Valve head was machined as a ½-inch disk with a 1-inch long, 1/8-inch diameter stem at the center. The total stem length was achieved by welding an 1/8-inch rod to the 1-inch stem of the Valve Head.

The Valve Seat was manufactured as a 0.035-inch washer with a 1/8-inch diameter bore at its center to accommodate the Valve Stem. The Valve Seat was held flush against the Valve Head with the Seat Clamp. The Seat Clamp also served the purpose of maintaining the axial distance between the Valve Seat the upper Multi-leaf Flexure Assembly. The Seat Clamp length was thus defined as the distance measured between the seating surface of the Valve Throat and the first Inner Spacer with the flexure in their neutral position. The Seat Clamp is tapered at the Valve Seat end to ensure sufficient clamping area and to prevent the Valve Seat from fluttering as helium flows into the external flow loop. Figure 3.27 shows an standard orthographic view of the Seat Clamp.

When the valve was closed, the Valve Stem was held in tension between the valve seat resting against the Valve Throat and the Inner Compression Spring Platform. The components about the Valve Stem, which held this assembly clamped, were the Multi-leaf Flexure Assemblies, the Seat Clamp, the Core Clamp, the Ferromagnetic Core and the Inner Compression Spring Platform. These components were held in compression via a single 5-40 nut at the end of the Valve Stem. The dimensions and spacing between all other components in the Valve Assembly set the dimensions of the Core Clamp.

The Core Clamp acted as the final spacer between the Ferromagnetic Core and the upper Multi-leaf Flexure Assembly. The dimensions of this component were defined by the geometry of the Magnetic Cage. Its geometry is described in Figure 3.28. The Inner

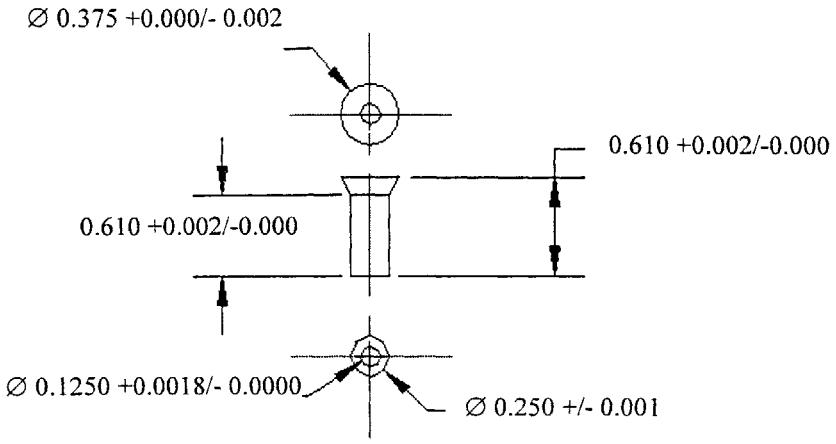

Figure 3.27 - Standard orthographic View of the Seat Clamp

Spacers defined the geometry of the disk end. To ensure the optimal usage of the surface area of the Ferromagnetic Core, the wall thickness of the throat of the Core Clamp was minimized. The wall thickness was chosen to ensure the throat would not mushroom under the applied compressive load. The length of the Core Clamp was defined as the distance between the last upper Multi-leaf Flexure Assembly and the top of the Ferromagnetic Core when the Electromagnetic Circuit was at its maximum air gap.

With the Core Clamp length specified the final length of the Valve Stem was specified as 3.93-inches. This length accommodated all of the components about the Valve Stem and a 5-40 allen-head nut. Once welded to the Valve Head, the Valve Stem was machined to length and the end threaded with 5-40 threads. Figure 3.29 shows a photograph of the Valve Head, Valve Stem, Valve Seat and Seat Clamp.

With all of the geometry of the valve specified, the concern of eddy currents developing in the Ferromagnetic Core was addressed. In electromagnetic circuit design, eddy currents, magnetic currents that run the circumferentially about the ferromagnetic components, can arise. Once developed, these currents act to retard the magnetic field in the electromagnetic circuit. Thus, the amount of force that can be extracted from the electromagnetic circuit is diminished. To hinder this behavior, the ferromagnetic parts were manufactured so that a continuous circumferential magnetic path was not available.

In the Magnet Cage, this was accomplished incidentally with the machining of fluid passages through the wall thickness. However, the process of eliminating these magnetic pathways was more difficult in the Ferromagnetic Core. In a first attempt, the Ferromagnetic Core was slotted in a process similar to the process that slotted the

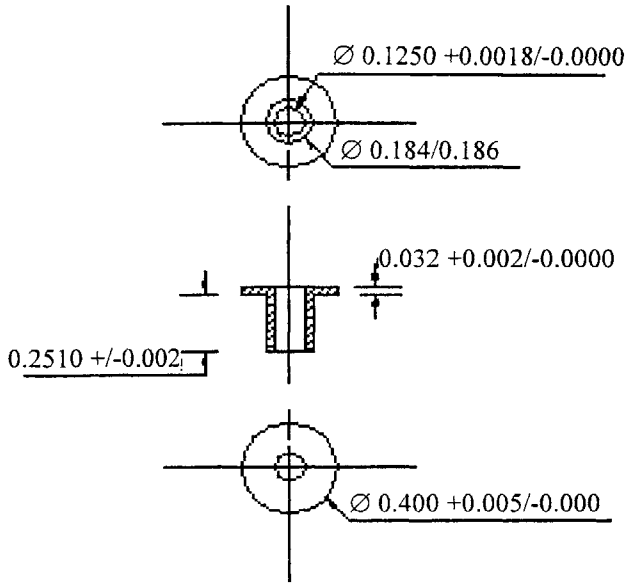

Figure 3.28 - Standard orthographic View of Core Clamp

Magnetic Cage. Four slots, 0.010-inch wide were machined ¼-inch deep into the length of the Ferromagnetic Core. This procedure proved to significantly reduce the cross-sectional area of the Ferromagnetic Core. This resulted in an unacceptable reduction of the magnetic force produced in the Electromagnetic Circuit. Refer to Equation 3.1 for the relationship between magnetic force and electromagnetic circuit geometry.

An additional difficulty in this configuration arose in boring the 1/8-inch diameter center hole into the Ferromagnetic Core. The low- carbon steel chosen for this application was soft and difficult to machine. The machining of the long center bore resulted in significant tool drift from the entrance to the exit of the bore. This resulted in misalignment of the Valve Stem relative to the Ferromagnetic Core.

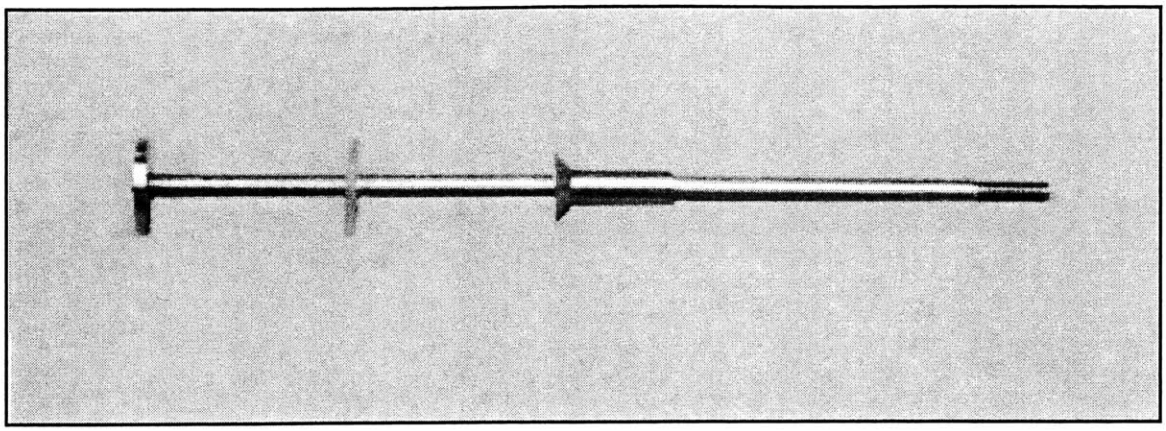

Figure 3.29 - Photograph of Head, Stem, Seat and Seat Clamp

In order to maintain the cross-sectional area of the Ferromagnetic Core and ensure a straight center bore, a unique manufacturing process was developed. The Ferromagnetic Core was manufactured of four 3/8-inch square quadrants of low-carbon rolled steel and the circular cross-section was achieved through a six step machining process. Since this presented a unique method of core manufacture, the process is outlined below.

Ferromagnetic Core Machining Process:

1. **Welding-** Four 2.5-inch lengths of 3/8- by 3/8- inch low carbon steel rolled were lightly tack welded at the ends into the configuration shown in Figure 3.30a.

2. **Turning-** Using a ¾-inch square collet, the corners of the four quadrants were broken. This resulted in the dimension A-A of Figure 3.30b measuring 0.967-inch.

3. **Rotation and Welding-** The four tack welds were filed away and each quadrant was rotated to bring the four broken corners to the center as shown in Figure 3.30c. The quadrants were again tack welded at the ends. Since these tack welds held the core together, they were allowed to penetrate deeper into the material than the previous one.

4. **Center Boring-** The broken corners of the quadrants provided a straight and centered guide hole through the Ferromagnetic Core. This hole was used to guide a long twist drill through center of the quadrants. The twist drill size was chosen so the Ferromagnetic Core was a loose press fit on the Valve Stem. Figure 3.30d shows this step. Again, the ¾-inch collet was used to grip the assembly.

5. **Turning**- The four quadrant assembly was turned from a square cross-section to a circular cross-section. In reference to Figure 3.30e, the final Ferromagnetic Core diameter of 0.655-inch was achieved in this step.

6. **Trimming**- The Ferromagnetic Core was finally machined to the length of 2.235-inches and the final configuration. The square end used to grip the part was removed in this step as well. An standard orthographic view of the final assembly is shown in Figure 3.31.

This process broke the circumferential path around the Ferromagnetic Core into for quadrants. It as successfully designed a method for creating a straight and centered guide hole through the Ferromagnetic Core.

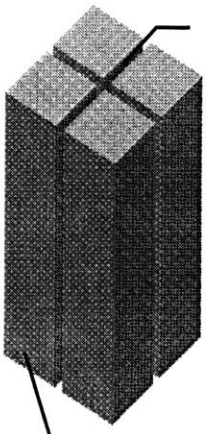

(a) Step #1

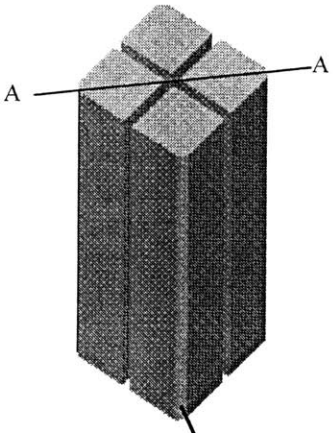

(b) Step #2

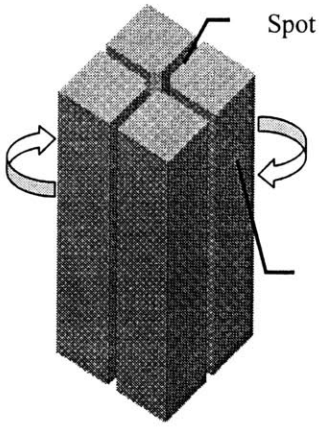

(c) Step #3

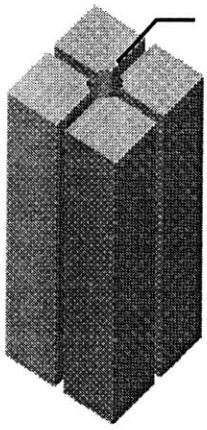

(d) Step #4

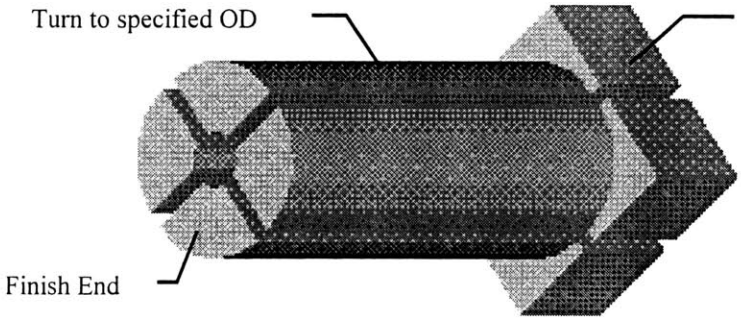

(e) Step #5

Figure 3.30 – Isometric View of the Procedure for Machining the Ferromagnetic Core

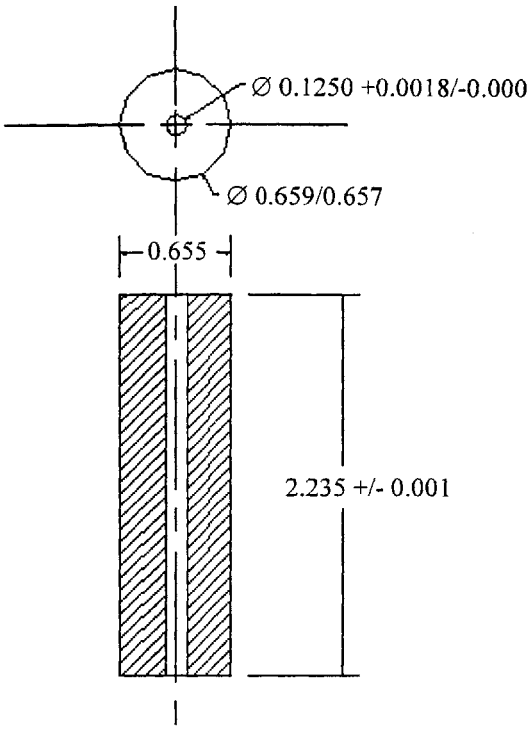

Figure 3.31 – Standard orthographic View of Ferromagnetic Core

CHAPTER 4- Thermodynamic Cycle Analysis

4.1 Standard G-M Cycle and System

Ideally, the G-M cryocooler was a system consisting of an open-cycle with two constant volume and two constant pressure thermal processes. Unlike the proposed design for the new cryocooler, the G-M cryocooler was driven by an external compressor and controlled at the warm end by a charge valve and an exhaust valve. The system specified here was rated as a 150-Watt at 77 K capacity. It was a single-stage, cryocooler with helium as the working fluid. The two main components of the system were the compressor and the cold head. The external compressor was a single-stage scroll-type compressor. It operated at room temperature and supplied two constant pressures, P_H and P_L, to the cold head. Detailed examination of the compressor will be forgone in this thesis.[8] Relationships developed from Introduction to Thermodynamics by Sonnetag and Van Wylen[9] and Engineering Thermodynamics by Cravalho and Smith.[10]

The principal thermodynamic components of the Coolpower 150 cryocooler, shown in the schematic of Figure 3.1, were as follows:

Comp – External scroll-type compressor.

V1 – Warm end valve 1 – operated between high supply pressure, P_H, 275 psi gauge and warm volume.

V2 – Warm end valve 2 – operated between low supply pressure, P_L, 75 psi gauge and warm volume.

D – Displacer– piston-like mechanism inside of cold head cylinder.

D_R – Electric motor – displacer driver mechanism.

R – Regenerator matrices – the primary heat transfer mechanism contained inside the displacer.

W – Warm volume.

C – Cold volume – point where external load was applied.

As shown, the cross-sectional interfaces between components were the regenerator warm

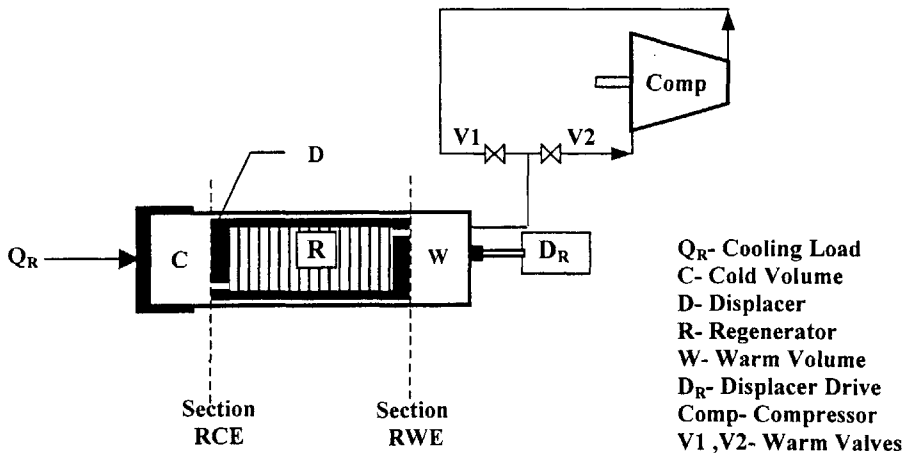

Figure 4.1 - Thermodynamic components of the unmodified system

end, RWE and regenerator cold end, RCE.

When operated as specified by the manufacturer, the G-M cycle consisted of the four discreet processes and four equilibrium states defined below. Top dead center (TDC), in reference to Figure 4.1, was defined when the displacer was to the left with C at minimum volume.

State 1	W, R and C, all at P_L, D at TDC
Process 1-2	Close valve V2, open valve V1, charge W, R and C to P_H
State 2	W, R and C at P_H, D at TDC
Process 2-3	Move displacer from TDC to BDC
State 3	W, R and C at P_H, D at BDC
Process 3-4	Close valve V1, open valve V2 to blow down to P_L
State 4	W, R and C at P_L, D at BDC
Process 4-1	Move displacer from BDC to TDC

For the cold volume, the solid line in Figure 4.2 shows these states and processes on a Pressure-Volume diagram.

In order to examine the performance of the cold EM valves, the external flow loop was added to this standard system. Figure 4.3 shows how this addition modified the system for the purposes of this project. The existing system appears in gray and the additional equipment is in black. The additional components added to the system were as follows:

S – Surge volume –large cold volume external to the cold head to maintain an essentially continuous flow through the external flow loop.

HE – Heat exchanger –refrigeration load for external flow loop.

V3 – Cold electromagnetic valve 3 –cold volume exhaust valve, operates downstream of the cold volume.

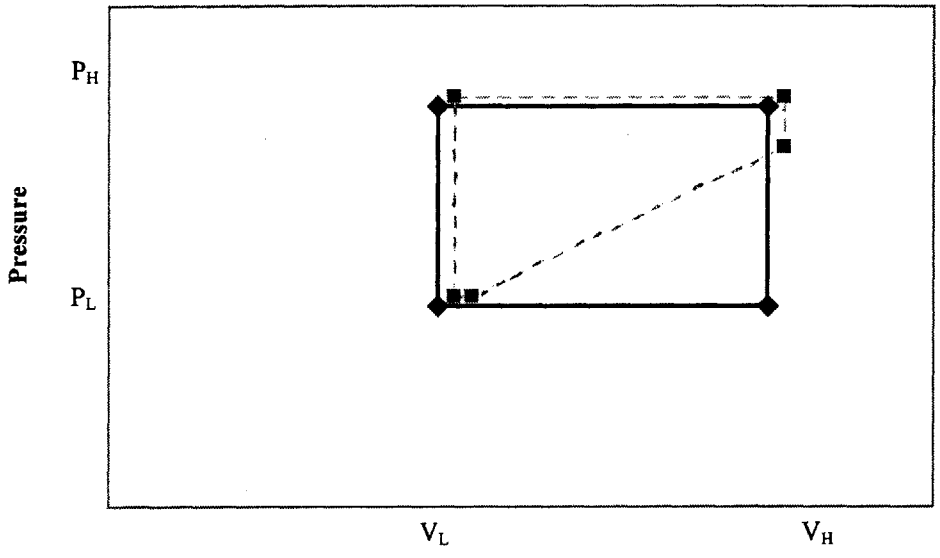

Figure 4.2 - P-V diagrams of the two processes

V4 – Cold electromagnetic valve 4 –cold volume intake valve, operates downstream of the external load heat exchanger and the surge volume.

As shown, three additional cross-sectional interfaces were defined as surge intake, SI, heat exchanger inlet, HEI and heat exchanger outlet, HEO.

For this analysis, the mass of gas stored in heat exchanger HE was assumed small compared with that of the cold volume and the surge volume. This modified cycle consisted of the discreet processes and equilibrium states defined below. In this case, an intermediate pressure, P_X, defined a new state in the cycle.

State 1	W, R, C and S all at P_L, D at TDC
Process 1-2	Close valve V2, open valve V1, charge W, R and C to P_H
State 2	W, R and C at P_H, S at P_L, D at TDC
Process 2-3	Move displacer from TDC to BDC
State 3	W, R and C at P_H, S at P_L, D at BDC
Process 3-4	Close valve V1, open valve V2 until W, R and C reach P_X
State 4	W, R and C at P_X, S at P_L, D at BDC
Process 4-5	With V2 closed, open V3 to equalize W,R and C with S
State 5	W, R, C and S at $P_L + \Delta P$, D at BDC
Process 5-1	Close V3, open V4 and V2 to equalize W,R,C and S to P_L, then move displacer from BDC to TDC.

Referring again to Figure 3.2, the pressure-volume diagram appear as the broken line. Process 4-5 was defined as an adiabatic expansion into the surge volume through the external flow loop. Process 5-1 was the completion of the expansion through valve V2.

To compare the performance of the unmodified and the modified systems, a simple first-order thermodynamic analysis was performed. The performance of the two cycles

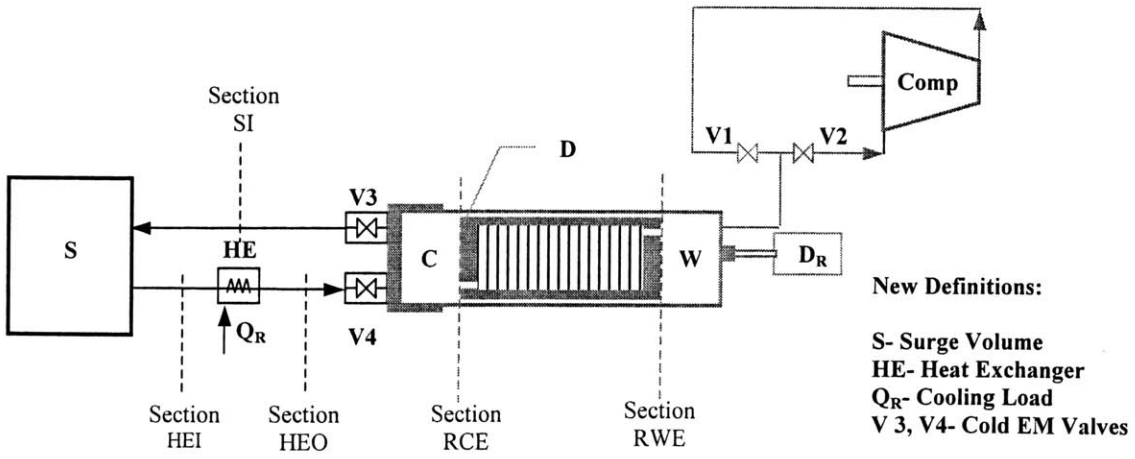

Figure 4.3 - Thermodynamic components of the modified system

was compared to determine how the external flow loop degrades the performance the given G-M cycle. This analysis was based on mass and energy balances for each component throughout each process.

4.2 G-M Cycle Analysis, Standard[9,10]

Beginning at state 1, valve V1 was opened and high-pressure helium charged the regenerator R and the warm volume W to 275 psi gauge at state 2. Process 2-3 filled the cold volume C with gas by moving D from TDC to BDC at State 3. The helium lost heat as it flowed through the regenerator matrices. Due to the displacer motion at system high-pressure P_H, the work $P_H \cdot V_C$ flowed up the displacer. At state 3, valve V1 closed and valve V2 opened. Through valve V2, the gas in both volume C and in the regenerator was exhausted to system low-pressure P_L to arrive at State 3. As the displacer moved from BDC to TDC during Process 4-1, the cool gas flowed through the regenerator and out valve V2. During processes 3-4 and 4-1, heat flowed from the walls of volume C to the cold gas.

Performing a first law analysis for each process, allowed the overall cooling capacity to be determined. Balancing energy and mass flows for the volumes contained in C and R gave the cooling Q_R as

$$Q_R = (P_H - P_L) \cdot V_C - \oint_{RWE} h \cdot dm \qquad \text{Eq. (4.1)}$$

where V_C was the displacer displacement volume. The first term defined the net-work that flowed up the displacer from the cold end to the warm end. Due to the ineffectiveness of the regenerator for specified temperature span, the second term arose as the net enthalpic flow h that flowed down the regenerator from warm end to cold end. The net enthalpic flow for the cryocooler was evaluated from the measured cooling capacity and the displacer work term. A detailed analysis appears in Appendix B-Thermodynamic Analysis.

4.3 G-M Cycle Analysis, External Flow Loop Added[9,10]

In the modified cycle, States 1, 2 and 3 as well as processes 1-2 and 2-3 were the same those specified for the standard cycle; therefore, the same mass entered the regenerator R across section RWE for both cycles. Additionally, both cycles were considered to have equivalent regenerator effectiveness and temperature spans.

The modified cycle varied from the unmodified beginning at state 3. At state 3, valve V2 opened and in process 3-4, gas exhausted out through valve V2 until the pressure in volume C and regenerator R decreased to state 4. State 4 was defined as having a pressure P_X that is intermediate to P_H and P_L. At P_X, valve V2 closed and EM valve V3 opened. The degree which the external flow loop affects the system performance was determined by varying the value of the control parameter P_X. In process 4-5, gas in cold head exhausted out through EM valve V3 into the external flow loop until the pressure in volume S, volume C and regenerator R equalized to pressure $P_L + \Delta P$, where ΔP was defined as a differential pressure that was just sufficient enough to drive the helium through the external flow loop. At $P_L + \Delta P$, valve V3 closed and valve V2 opened. The

displacer now moved from TDC to BDC and the exhaustion of the regenerator R, volume C and volume S to P_L proceeded through valve V2.

The operating states of the modified cycle were defined such that the net enthalpic flow at the warm end of the regenerator and the temperature span within the regenerator are the same as in the simple cycle. Equation 1 was still used to define Q_R for the energy and mass balances on volumes C, R and S. This particular analysis aimed at examining only those loses associated with the addition of the external flow loop; therefore, electrical losses in EM valves V3 and V4 are ignored and heat leaks were considered to be negligible. By matching processes 1-2 and 2-3 to the standard cycle, Q_R was unaffected by either the addition of the flow loop or the value of P_X selected for the cycle.

However, the refrigeration temperature at which the load was cooled was affected by both of these factors. Examining the predicted refrigeration temperature for each cycle did the comparison of the performance between the standard cycle and the modified cycle. This was done by relating the refrigeration temperature at the external heat exchanger HE to the low temperature defined by the span of the regenerator. Examination and balance of the fluxes of both energy and mass at boundaries RWE, RCE, SI, and HE2 allowed energy flux across HEI during process 5-1 to be determined. This was accomplished sequentially beginning at State 1, Process 1-2 and following each process in order.

With the exception of Process 4-5 the end state of each process was determined from initial conditions. A numerical integration was performed from State 4 to the final state as determined by the selected P_X. For the regenerator R and volume C, State 1 was predetermined, which set the end point of Process 5-1. This allowed the determination of the energy flux that exited HE and flowed across section HEO to volume C for Process 5-1. For this analysis, gas crossing section HEO was assumed to be at the load temperature. By doing this, the cooling load temperature was fixed by the flow of energy across boundaries.

Instead of reducing Q_R, the modification of the cycle resulted in a higher cooling temperature than that for the simple cycle. It was also shown that the value of P_X had a significant impact on the performance of the cycle. The cooling temperature as a function of the intermediate pressure P_X is shown in Figure 4.4. This was for the regenerator span specified by the standard system, which was given by a cooling temperature of 77 K.

From Figure 4.4, it was concluded that the maximum available mass would be circulated into the surge volume. Thus, P_X was chosen to be as close to P_H as possible, which means that since there is no improvement in refrigerator performance, process 3-4 was not a necessary addition to the cycle. For the purposes of driving the helium through external flow loop, P_X was chosen as only differentially less than P_H. In this analysis, the volume S was treated as a large pressure reservoir; therefore, external flow loop mass circulation was maximized when the volume S was large compared with driving volume C.

The modifications largest affect was realized as an in increase in refrigeration temperature at the load. At the operating point where P_X was approximately equivalent to P_H, the refrigeration temperature was calculated as 80 K. Modeling approximations could result in this higher temperature, but second-order affects are likely to have caused the apparent increase in cooling temperature. Exhausting from P_X to P_L through EM

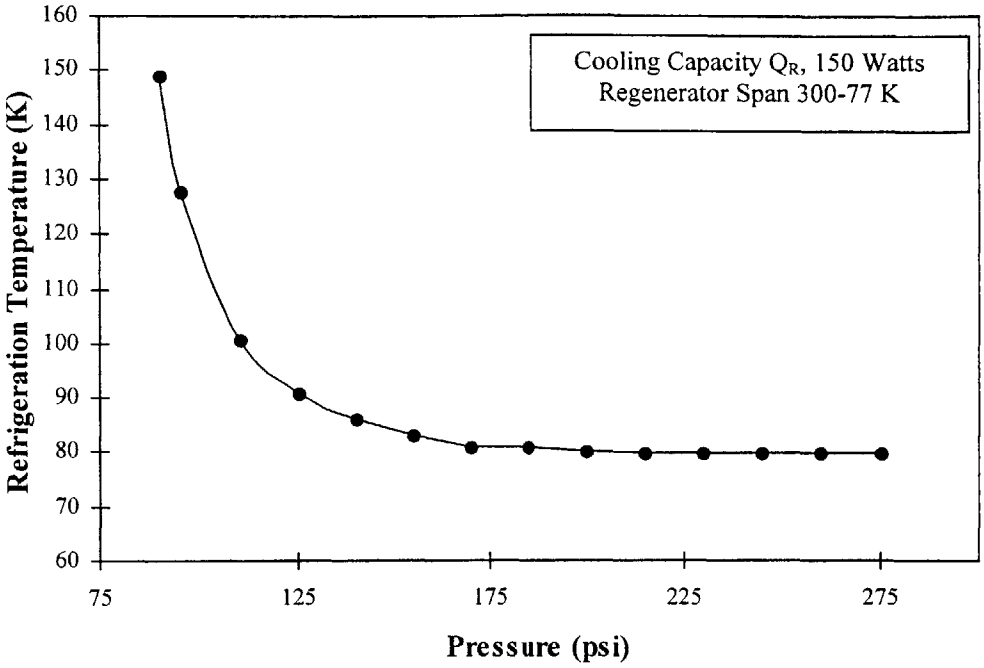

Figure 4.4 - Temperature Distribution with changing P_X

valve V3 moves the cooling load, Q_R, from the mass expanding in the cold volume to the mass circulating in the surge volume. Decreasing P_X resulted in a decrease the circulating mass. In order to absorb the cooling load, a larger temperature rise of the circulating mass occurred. Thus a larger refrigeration temperature at Q_R is realized.
This preliminary analysis, examined only first order thermodynamic affects. A more in depth analysis would be required to examine the neglected second order affects such as losses at the valves, non-linearity in the regenerator temperature distribution and effectiveness and external radiation heat leak. A more thorough analysis and experimental procedure would be required to evaluate the impact of these second order affects on the cycle performance. A detailed analysis appears in Appendix B-Thermodynamic Analysis.

CHAPTER 5- Fluid Dynamic Analysis

Chapter 3 established the geometry of the EM valves and Chapter 4 presented a first order thermodynamic analysis of a G-M Cycle modified with an external flow loop. Here, a detailed analysis of the fluid dynamics associated with Process 4-5 of the modified G-M cycle. As stated previously, Process 4-5 was considered an adiabatic blow down of the cold volume into the surge volume. The analysis of this blow down process is presented in this chapter. Relationships in this chapter were developed from Introduction to Thermodynamics by Sonnetag and Van Wylen,[9] Fluid Mechanics by White[10] and Introduction to Fluid Mechanics by Fay.[11]

To remind the reader, the equilibrium states and discreet processes of the modified cycle are again presented here. Figure 4.3 is also appears again below as Figure 5.1.

State 1	W, R, C and S all at P_L, D at TDC
Process 1-2	Close valve V2, open valve V1, charge W, R and C to P_H
State 2	W, R and C at P_H, S at P_L, D at TDC
Process 2-3	Move displacer from TDC to BDC
State 3	W, R and C at P_H, S at P_L, D at BDC
Process 3-4	Close valve V1, open valve V2 until W, R and C reach P_X
State 4	W, R and C at P_X, S at P_L, D at BDC
Process 4-5	With V2 closed, open V3 to equalize W,R and C with S
State 5	W, R, C and S at $P_L + \Delta P$, D at BDC
Process 5-1	Close V3, open V4 and V2 to equalize W,R,C and S to P_L, then move displacer from BDC to TDC.

Recall, in chapter 3, it was determined that P_X should be equivalent to P_H. This minimized the refrigeration temperature at the heat exchanger. The blow down process through EM valve V3 begins at P_H and completes at the system equilibrium pressure of $P_L + \Delta P$.

The temperature span of the regenerator and the mass of fluid circulating into and out of the cold end of the regenerator was considered the same for both the modified and unmodified cycle. At the end of Process 3-4, the helium was at 83.5K. The mass of fluid available for the blow down process consisted of only the volume of fluid in the cold volume at State 4. The surge volume in the external flow loop was considered large compared with that of the cold volume. For this initial analysis, the EM valve was considered as an orifice with an area equal to that of the valve curtain area. The dynamics of the curtain area are incorporated into Chapter 7- Valve Dynamics.

The assumptions and simplifications allowed for the blow down analysis to be considered as an open adiabatic expansion of the cold volume. Expansion began at 275 psig and 83.5K. It proceeded through a 8.355E-4 m^2 orifice to 75 psig.

For helium, the critical pressure ratio was determined from Equation 5.1 with $\gamma = 5/3$.

$$\frac{P_{low}}{P_{crit,He}} = \left(\frac{2}{\gamma+1}\right)^{\frac{\gamma}{\gamma-1}} = 0.487 \qquad \textbf{Eq. (5.1)}$$

The pressure ratio of this system was greater than 3:1, which indicated that the blow down process began with choked flow through the orifice. Choked flow continued until the critical pressure ratio was achieved.

Since the blow down process was considered adiabatic, the Process 4-5 in the cold volume was defined as isentropic process that follows Equation 5.2

$$P_{CV} \forall_{CV}^{\gamma} = const. \qquad \textbf{Eq. (5.2)}$$

From this equation, the following adiabatic relationships are derived.

$$\frac{T_{CV}}{T_0} = \left[\frac{P_{CV}}{P_0}\right]^{\frac{\gamma-1}{\gamma}} = \left[\frac{v_{CV}}{v_0}\right]^{\gamma-1} \qquad \textbf{Eq. (5.3)}$$

Here, the subscript 0 indicates the initial conditions in the cold volume at time zero. P_0 was P_H; T_0 was the temperature of the helium exiting the regenerator; v_0 was the specific volume of the helium in the cold volume at these conditions. The displacer remained at BDC for this process, therefore the total volume of the cold volume remained fixed throughout the process.

During the choked flow process, the fluid was compressed at the throat and a limit was set on the amount of mass that could pass through the orifice. Equation 5.4 determined this limit.

$$\dot{m}_{choked} = \left[\left(\frac{\gamma}{R_{He}}\right)^{1/2}\left(\frac{\gamma+1}{2}\right)^{\frac{1-\gamma}{2(\gamma-1)}}\right]\left(\frac{A_{curtain}}{\sqrt{T_0}}\right)\frac{P_{CV}^{\frac{\gamma+1}{2\gamma}}}{P_H^{\frac{1-\gamma}{2\gamma}}} \qquad \textbf{Eq. (5.4)}$$

Once the critical pressure ratio was achieved, the flow became unchoked. Equations 5.5 defined the amount of mass passing through the throat area for unchoked flow.

$$\dot{m}_{unchoked} = A_{curtain}\left[\frac{5}{R_{He}T_0}\cdot\left[\frac{P_L^{\frac{\gamma+1}{\gamma}}}{P_H^{\frac{1-\gamma}{\gamma}}}\right]\cdot\left[\left(\frac{P_{CV}}{P_L}\right)^{\frac{\gamma-1}{\gamma}}-1\right]\right]^{1/2} \qquad \textbf{Eq. (5.5)}$$

In Equations 5.4 and 5.5, P_{CV} was defined as the dynamic pressure in the cold volume and Equation 5.6 defines the new pressure ratio.

$$P_{ratio} = \frac{P_L}{P_{CV}} \qquad \textbf{Eq. (5.6)}$$

The dynamic pressure was determined by applying the conservation of mass to the cold volume. The mass in the cylinder was determined by the ideal gas relationship of Equation 5.7.

$$m_{CV} = \frac{P_{CV}\forall_{CV}}{R_{He}T_{CV}} = \left(\frac{\forall_{CV}}{R_{He}}\right)\left(\frac{P_H}{T_0}\right)\left(\frac{P_{CV}}{P_H}\right)^{1/\gamma} \qquad \textbf{Eq. (5.7)}$$

Differentiating Equation 5.7 yields Equation 5.8, which was the mass flow rate from the cold volume through the valve as a function of the change in pressure in the cylinder over time.

$$\dot{m}_{CV} = \frac{1}{\gamma}\left(\frac{\forall_{CV}}{R_{He}}\right)\left(\frac{P_H}{T_0}\right)\left(\frac{P_{CV}^{\frac{1-\gamma}{\gamma}}}{P_H^{1/\gamma}}\right)\frac{dP_{CV}}{dt} \qquad \textbf{Eq. (5.8)}$$

Equating the mass flow rate of Equation 5.6 to the appropriate mass flow rate defined by either Equation 5.4 or Equation 5.5 allowed the change in pressure in the cold volume over time to be determined.

Equations 5.1 through 5.8 set up a step-wise integration approximation of the mass flow rate and pressure drop in the cold volume of the cylinder. This integration used a straight approximation between time steps. Step-wise integration was completed with Excel with time steps of 0.0001 seconds. At the completion of each time step, Equation 5.6 was compared with Equation 5.1 to determine the whether the flow regime was

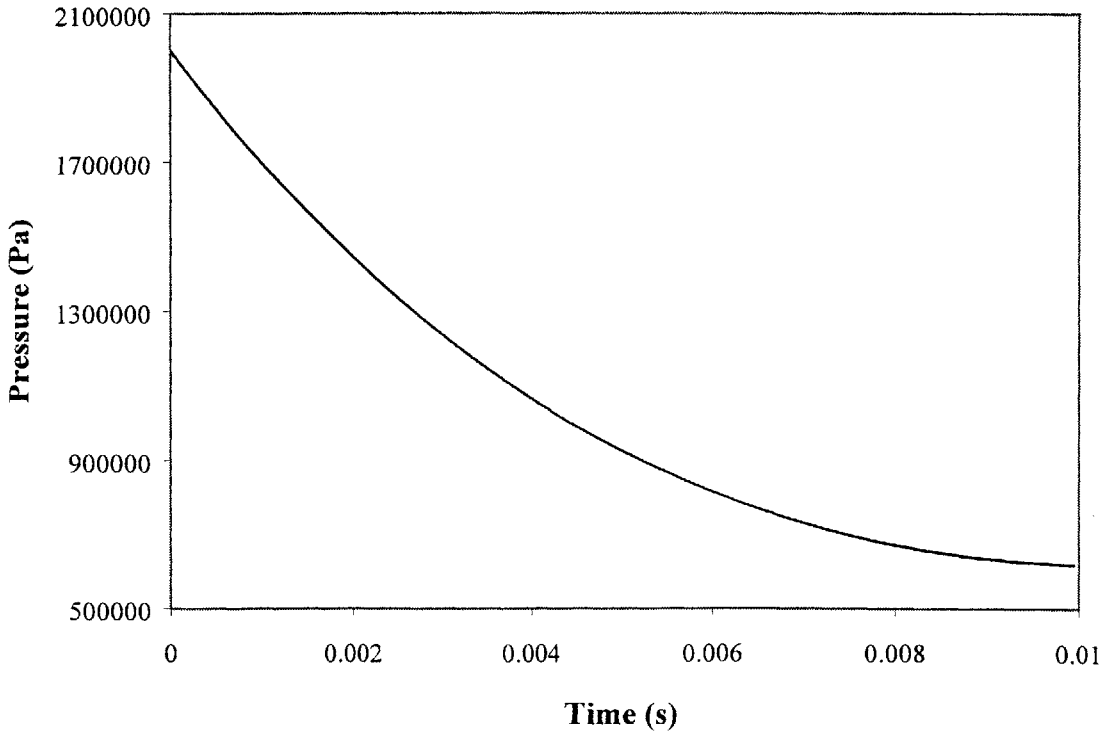

Figure 5.1- Pressure Change in CV with time

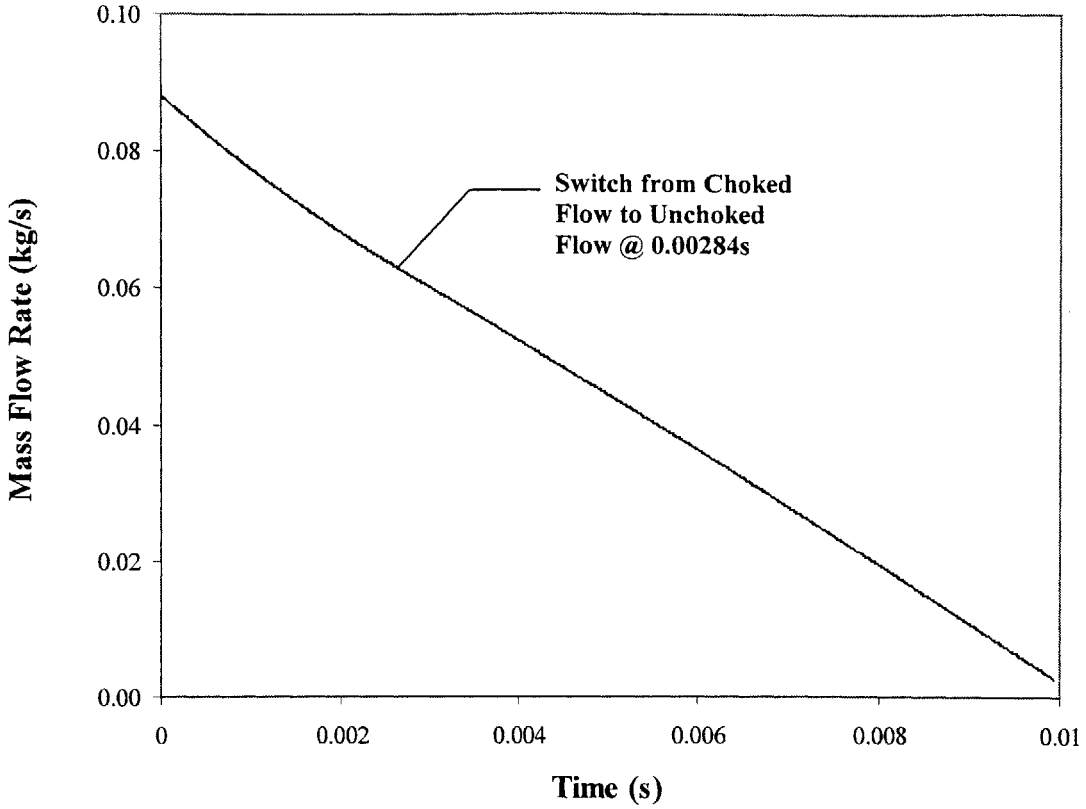

Figure 5.2- Mass flow rate across orifice over time

choked or unchoked. The integration marched on until the cold volume reached 75 psig and was in equilibrium with the backpressure in the surge volume.

Again, for the initial analysis, the valve was considered to be in its full open position with the curtain area fixed at 8.255E-4 m^2. Figure 5.2 presents a plot of how the pressure in the cold volume changed with time and Figure 5.3 depicts the mass flow rate over time. For this scenario, the pressure equalizes at 0.010 second.

Once the blow down dynamics were determined, the force on the valve head due to the pressure gradient was incorporated into the analysis. The dynamic pressure in the cold volume and the area of the top of valve head determined the pressure acting on the top of the valve head. The backpressure and the area of the bottom of the valve head determined the force acting on the bottom of the valve head. Figure 5.4 shows how the net force on the valve head, defined by Equation 5.9, changed with time.

$$F_{net} = P_{CV} A_{valve,top} - P_L A_{valve,bot} \qquad \textbf{Eq. (5.9)}$$

Details of the above analysis appear in Appendix C- Fluid Dynamic Analysis.

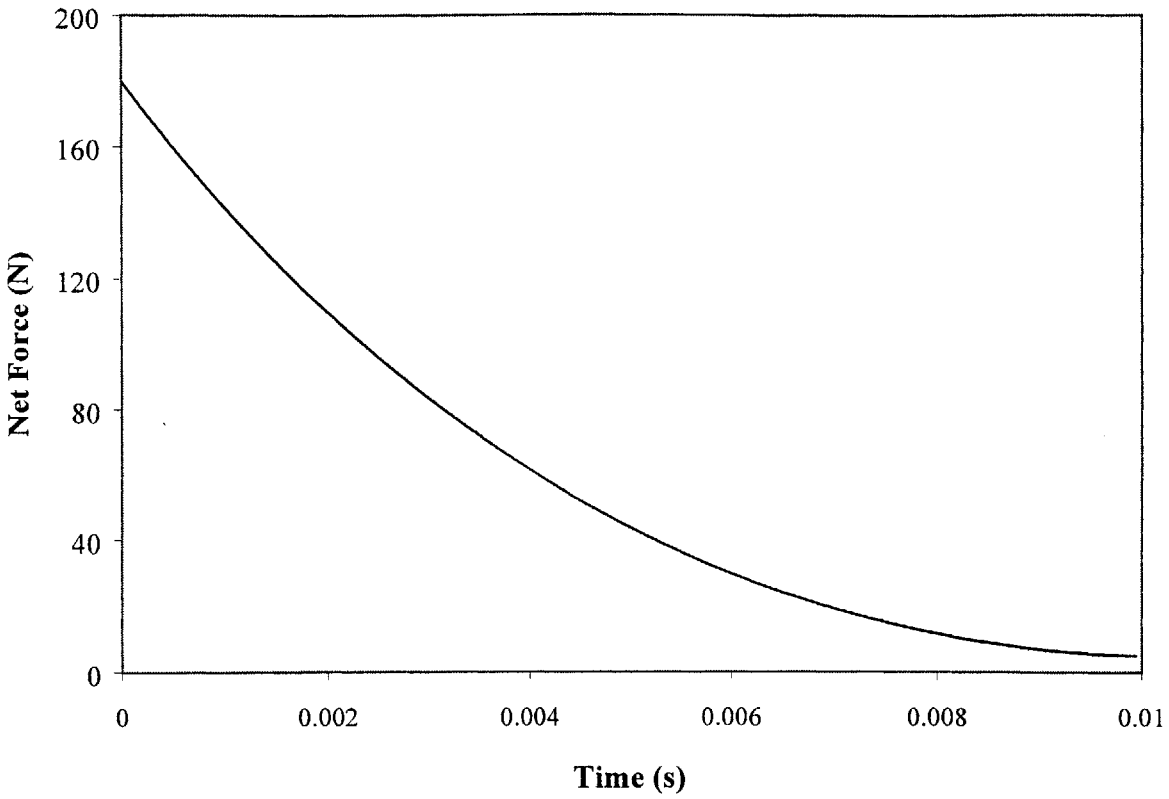

Figure 5.3- Force differential on the valve head over time.

CHAPTER 6- Electromagnetic Circuit Characterization

The analysis of the physical behavior of the electromagnetic circuit was the link between the electrical controller and the mechanical output of the valves. In order to design a controllable solenoid-type of electromagnetic valve, the physical properties of the electromagnetic circuit must be understood. Theoretical relationships laid the groundwork for modeling an electromagnetic circuit, but understanding the electro-mechanical relationships that pertained to this specific circuit was necessary. Once the valves were manufactured, the circuit was experimentally tested and empirical correlations were designed. This chapter discusses the methodology of testing, analyzing and modeling the electro-mechanical behavior of this valve's electromagnetic circuit. It also presents a process for modeling similar circuits. Electromagnetic relationships were developed in reference to Electric Machinery by Fitzgerald, Kingsley and Kusko,[13] Engineering Electromagnetics by Hayt[14] and Elements of Electrical Engineering by Cook and Carr.[15]

6.1 Experimental Set-up

Once manufactured, a test apparatus was designed for the EM valves. In simplest terms, the magnetic field intensity is related to the force produced by the field through Equation 6.1.

$$F_{mag} = \frac{B^2 A_{core}}{2\mu_0} \qquad \textbf{Eq. (6.1)}$$

From theory, magnetic field intensity is then related to current as shown in Equation 6.2.

$$B = \frac{Ni_{applied}\mu_0}{gap} \qquad \textbf{Eq. (6.2)}$$

Combining Equations 6.1 and 6.2, as stated previously, the ideal force produced in the air gap of an electromagnetic circuit can be related to the electrical input to the circuit via Equation 3.1. Equation 3.1 is repeated here (Equation 6.3) for reference.

$$F_{mag} = \frac{\mu_0 \cdot A_{core}}{2}\left[\frac{N \cdot i_{applied}}{gap}\right]^2 \qquad \textbf{Eq. (6.3)}$$

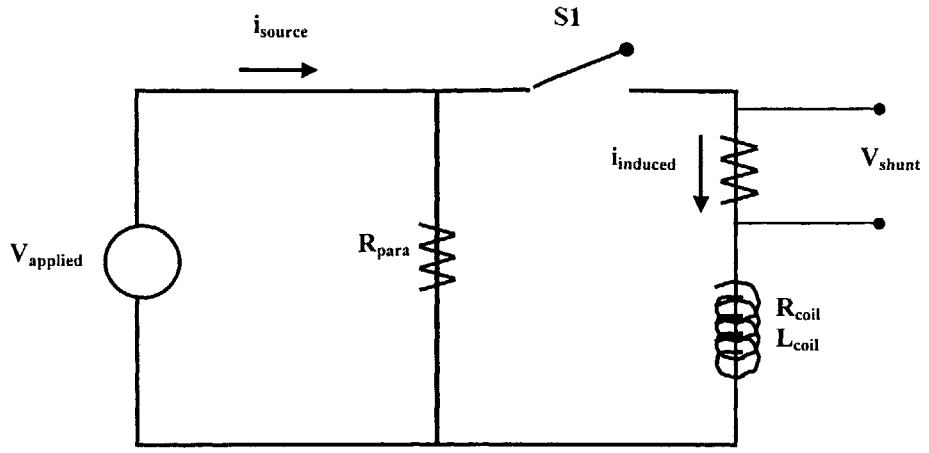

Figure 6.1- Schematic of Electrical Circuit used to obtain data for analysis

Given the geometry of the circuit and the specifications of the coil, the magnetic force is directly related to the square of the current in the coil and inversely related to the square of the length of the air gap. Therefore, it was desired explicitly to relate these three quantities.

On the electrical side, Figure 6.1 depicts the schematic of the circuit used in collecting the electromagnetic circuit data. The input voltage and shunt voltage were noted. The total number of windings per coil was 677, yielding a measured resistance in the Electromagnetic Coil of 2.3 Ω. A 2 Ω resistor was placed in parallel to the Electromagnetic Coil A 50 mΩ shunt resistor was placed in series to the Electromagnetic Coil and switch S1 was used to apply voltage to the coil over short durations to limit the electrical heating in the coil.

Mechanically, the force produced in the air gap was measured. This was accomplished by attaching measured loads to the threaded end of the valve stem. To quantify the load as just that applied, the compression spring was removed for this procedure. This is depicted in Figure 6.2. The weight of the Head-Stem-Core assembly was small compared to the attached loads and was thus negligible. The attached load varied from approximately 13 N to 222 N.

As stated, the length of the air gap also plays a role in the amount magnetic force produced. Once assembled the final gap length turned out as 0.0265-inch.

It was desired to examine the behavior of the valve for different gap geometries. Since this was a fast acting valve and the experimental set up was simple, the dynamics of the air gap-magnetic force-current relationship could not be measured directly. Discreet measurements were taken by varying the air gap geometry for each measured load attached to the valve stem. This was accomplished by placing combinations of 0.002-, 0.005- and 0.010-inch spacers between the Valve Seat and the seating surface of the Valve Throat. This allowed the gap geometry to be varied from 0.0265-inch to 0.0045inch.

Experimental data was collected in the following manner:

1. Added load- Load the valve stem with a measured load. Noted load.
2. Fixed initial gap geometry- Added spacer between Valve Head seating surfaces. Noted spacer thickness.
3. Applied Voltage to Coil- With power source in current limited mode, closed switch S1 and adjusted applied voltage until valve opened. Noted applied voltage and voltage across shunt resistor at opening.
4. Repeated with same load and new spacer thickness.

This procedure was then repeated for various loads between 13 N and 222 N. The shunt voltage was converted to a coil current and spacer thickness was converted to air gap geometry.

Data collected in this procedure appears in Appendix D- Trial Data. The conversion of the data appears in Appendix E- X-Factor Development.

6.2

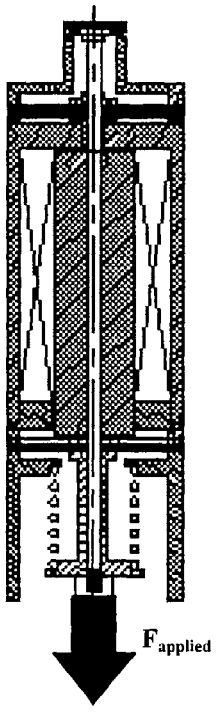

Figure 6.2- Cross-sectional view of valve loading for testing purposes

X-Factor Correlation Development

In Section 3.3- Electromagnetic Circuit Assembly, the Electromagnetic Circuit was designed to appear as the circuit presented in Figure 3.8. Ideally, the applied force is related to the current in the coil and the air gap geometry according to Equation 6.3. In an ideal circuit, this is true. However, in the real world, physical circuit characteristics dominate. Therefore, there were losses present. These losses arose for various reasons.

First, since the permeability of most steel alloys is only on the order of 5000 times that of air, magnetic flux is lost to the air surrounding the circuit. For similar reasons, the magnetic field also tends to fringe out in the gap as well. Only the magnetic field directly in the air gap volume and running parallel to the direction of motion contributes to creating a magnetic force on the ferromagnetic core.

Additional losses arose from material imperfections, circuit imperfections and air gaps presented by the manufacturing process.

All of these losses added up to an electromagnetic circuit that did not behave according to theoretical relationships. No theoretical relationships exist to quantify any of these losses specifically. As shown in Figure 6.3 (a), the circuit of Figure 3.8 was modified with two additional flux paths: a series path and a parallel path. Individual losses were not quantified, but all the losses were lumped into one of these paths.

From the analogous electrical circuit in Figure 6.3 (b), the relationship of Equation 6.4 was developed. Analogous to electrical potential, current and resistance, magnetic potential is Ni, current is flux and resistance is reluctance.

$$Ni_{shunt} = \phi_{gap}\left[R_{series} + \frac{1}{1/R_{gap} + 1/R_{para}}\right] \qquad \textbf{Eq. (6.4)}$$

This initial analysis attempted to directly quantify the equivalent resistances in the circuit, R_{series} and R_{para}. Equations 6.5 gives the final relationship developed from Equation 6.4 for this circuit. It was intended that the three unknowns, R_{series}, R_{para}, and ϕ_{para}, were found for each air gap geometry as a function of applied force. The background development and algebra appear in Appendix F- X-Factor Development.

$$\sqrt{\frac{2F_{applied}}{(A_{core}\mu_0)}} \cdot gap = Ni_{shunt}\left[R_{series} + \frac{1}{1/R_{gap} + 1/R_{para}}\right]^{-1} - \phi_{para}$$

$$R_{gap} = \frac{gap}{\mu_0 A_{core}} \qquad \textbf{Eq. (6.5)}$$

Using the relationships defined by Equations 6.5, it was attempted to directly quantify the losses in the electromagnetic valve. However, applying this relationship to the data collected in the procedure outlined in the previous section yielded a linear relationship between the series magnetic flux, parallel magnetic flux and the air gap magnetic flux. Each of these quantities varied linearly with respect to each other as the circuit geometry

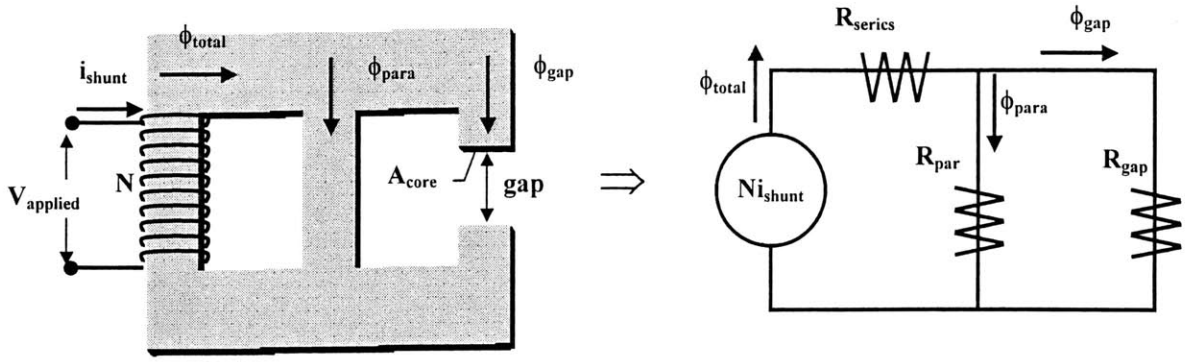

(a) Electromagnetic Circuit **(b) Equivalent Electrical Circuit Analogy**

Figure 6.3 – Theoretical Magnetic Circuit including flux leakage paths

and applied load change. It was concluded that Equations 6.5 could not yield independent relationships for each flux present in the circuit.

Upon determining the linear dependence of the three flux quantities, it was necessary to design a new approach for characterizing the behavior of the electromagnetic circuit. The method for developing the empirical correlation that related the applied force to the air gap geometry and the coil current is discussed here. Although specific to this valve, this method was intended to be a design tool that can be applied to similar electromagnetic circuits.

In reference to the analogous electrical circuit in Figure 6.3 (b), Kirkoff's and Ampere's Laws were applied to this circuit and Equations 6.6 were determined. Again the analogous magnetic potential, current and resistance were used.

$$\frac{\phi_{series}}{\phi_{gap}} = \frac{\phi_{total}}{\phi_{gap}} = 1 + \frac{\phi_{para}}{\phi_{gap}}$$

Eq. (6.6)

$$(Ni)_{gap} = (Ni)_{para}$$

The following general magnetic relationship was applied to the relations of Equations 6.6.

$$Ni_{gap} = \frac{l_{gap}}{\mu_{gap} A_{gap}} \cdot \phi_{gap}$$

$$Ni_{para} = \frac{l_{para}}{\mu_{para} A_{para}} \cdot \phi_{para} \qquad \textbf{Eq. (6.7)}$$

The result is presented in Equation 6.8.

$$\frac{\phi_{para}}{\phi_{gap}} = \left[1 + \frac{\frac{\mu_{para} A_{para}}{l_{para}}}{\frac{\mu_0 A_{gap}}{l_{gap}}} \right] \qquad \textbf{Eq. (6.8)}$$

However, the data was taken in terms of coil currents and applied loads and not in terms of magnetic fluxes. Given that the measured quantities were not fluxes, Equation 6.8 proved difficult in applying it to the measured data.. Therefore it was desired to characterize this quantity in terms of the measured coil currents, applied loads and physical gap geometry.

Equation 6.5 stated that, theoretically, if a prescribed magnetic force were to be produced then a specified current should be applied to the coil. The actual magnetic force produced in the gap was the same as the force produced by the applied load. Therefore, given the applied load a theoretical current could be determined as shown in Equation 6.9.

$$F_{applied} = \frac{\mu_0 \cdot A_{core}}{2} \left[\frac{N \cdot i_{theoretical}}{gap_{theoretical}} \right]^2 = \frac{B_{theo}^2 A_{core}}{2\mu_0} \qquad \textbf{Eq. (6.9)}$$

Equation 6.10 represents solving Equation 6.9 for the theoretical current.

$$i_{theoretical} = \sqrt{\frac{2F_{applied}}{\mu_0 \cdot A_{core}}} \cdot \frac{gap_{theoretical}}{N} \qquad \textbf{Eq. (6.10)}$$

From this relationship, an empirical correlation termed the X-Factor was derived as the ratio of the theoretical current to the observed current for given applied loads and theoretical gaps. This is shown in Equation 6.11. In this relationship note that the X-Factor relationship was correlated from the measured quantities of observed current, applied force and theoretical gap.

$$\frac{i_{theoretical}}{i_{observed}} = \mathrm{X} = \sqrt{\frac{2F_{applied}}{\mu_0 A_{core}}} \cdot \frac{gap_{theoretical}}{Ni_{observed}} \qquad \textbf{Eq. (6.11)}$$

Equation 6.9 represented the theoretical relationship between the applied force and the current. However, recall that the air gap geometry also played an important roll in this relationship. The actual physical air gap differs from the gap that is used in this relationship. Theoretically, when the air gap reached zero, either the theoretical magnetic force became infinite or the theoretical current became zero. Physically, neither of these scenarios was the case. As a result, Equation 6.9 required a theoretical gap to calculate the theoretical current.

The theoretical air gap was derived from experimental data. Data was grouped according to the applied load. The observed current was measured as a function of gap for several values of applied load. Air gap as a function of current was plotted for each applied load. Plots of 'Air Gap versus Current' for a few selected loads appear in Figure 6.4.

In Figure 6.4, trendlines extrapolating the data back to zero current appear as solid lines. As can be seen, all trendlines extrapolated back to zero current at an apparent air gap of -0.006-inch. The negative value indicated that a current theoretically existed when the physical air gap was zero. This was a result of imperfect circuit geometry and losses due to other air gaps in the circuit. The theoretical air gap used in Equation 6.11 was defined as the following.

$$gap_{theoretical} = gap_{actual} - gap_{no-current} \qquad \textbf{Eq. (6.12)}$$

The same plot was also used to define the experimental correlation of the X-factor. Equation 6.11 was rearranged to appear as Equation 6.13

$$\frac{gap_{theoretical}}{i_{observed}} = \sqrt{\frac{\mu_0 A_{core} N^2}{2F_{applied}}} \cdot X_{current} \qquad \textbf{Eq. (6.13)}$$

Since the theoretical air gap was a linear combination of the physical air gap and the zero current air gap, it was noted that the quantity on the left of Equation 6.10 was the slope of the lines that appear on the plots of Figure 6.5 and 6.6.

Figure 6.5 presents a plot of the slopes of the Air Gap/Current relationships as a function of applied load. The thin line represents the actual slopes taken from the data and the thick line represents corresponding points from the curve fit relationship presented in Equations 6.14.

$$f(F_{applied}) = 0.003\left(\frac{in}{Amp}\right) + 0.065\left(\frac{in}{Amp}\right) \cdot \exp\left[-0.115\left(\frac{1}{lbf}\right)\left(1.09lbf + F_{applied}\right)\right]$$

Eq. (6.14)

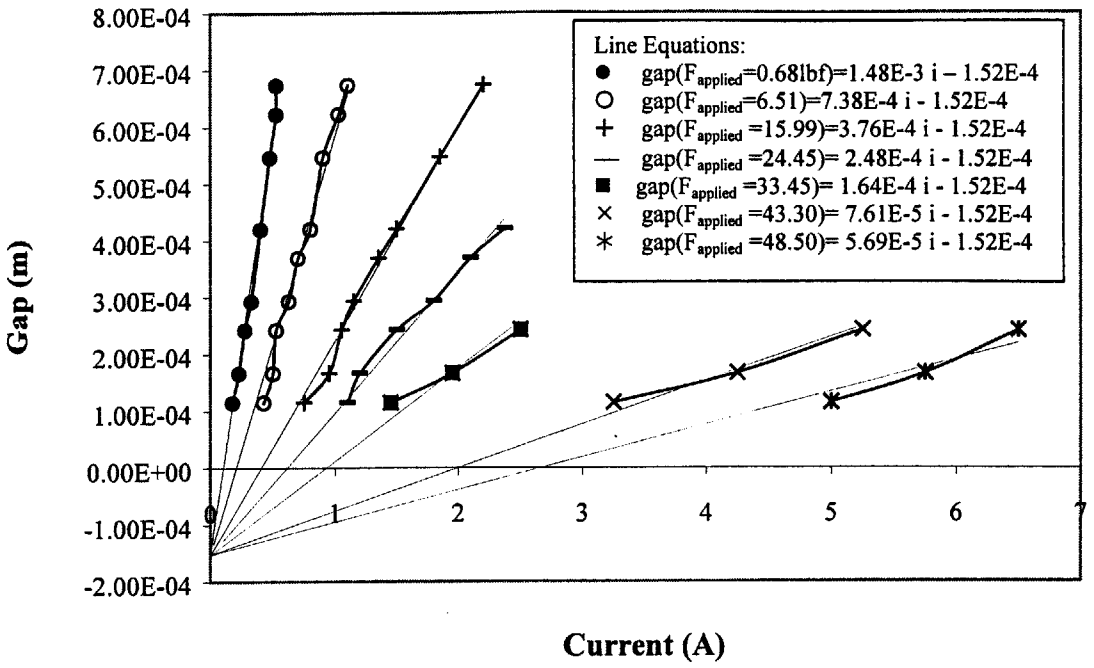

Figure 6.4 – Plot of Air Gap versus Current.

These functions were then used in Equation 6.13. Thus, the X-Factor was empirically determined as a function of the slopes of the Air Gap versus Current plots and the applied load. The resulting empirical correlation appear in Equation 6.15.

$$X = \sqrt{\frac{2F_{applied}}{\mu_0 A_{core} N^2}} \cdot 0.003\left(\frac{in}{Amp}\right) + 0.065\left(\frac{in}{Amp}\right) \cdot \exp\left[-0.115\left(\frac{1}{lbf}\right)\left(1.09lbf + F_{applied}\right)\right]$$

Eq. (6.15)

The empirical correlation defined by Equation 6.15 were the single most important relationships in characterizing the electro-mechanical behavior of the valves. This was strictly an empirical correlation and did not arise from the application of Maxwell's equations. This correlation represented the defining link between the input from the external electrical circuit and the output to the mechanical motion of the valve head. The X-Factors were plotted in Figure 6.6 for data ranging from 0.68 lbf to 50 lbf. A method for completing this analysis on a similar electromagnetic circuit appears in Appendix E-X-Factor Development.

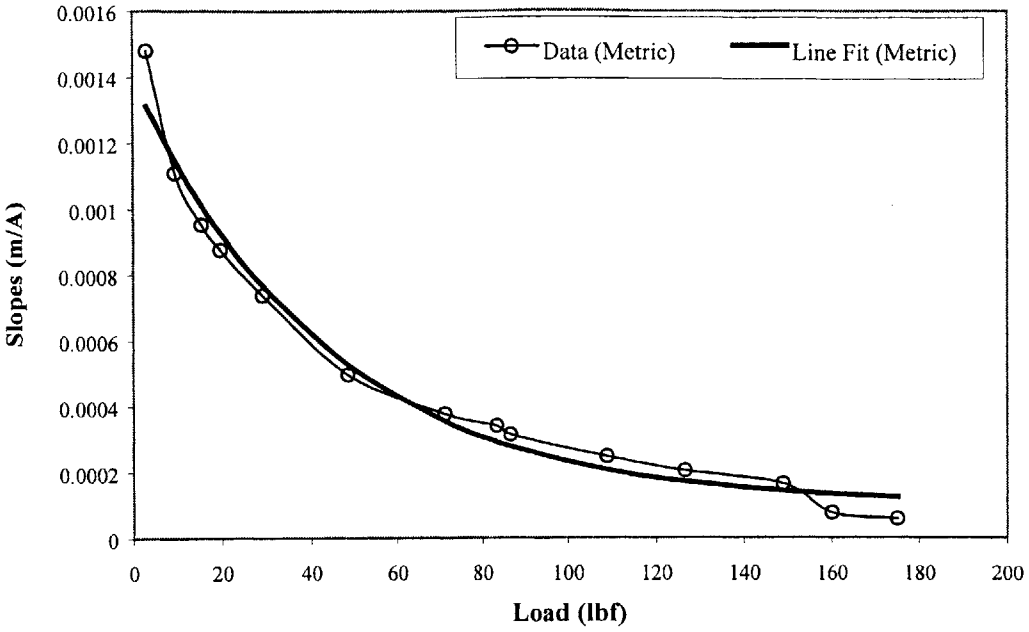

Figure 6.6 – Air Gap/Current as a function of Applied Load

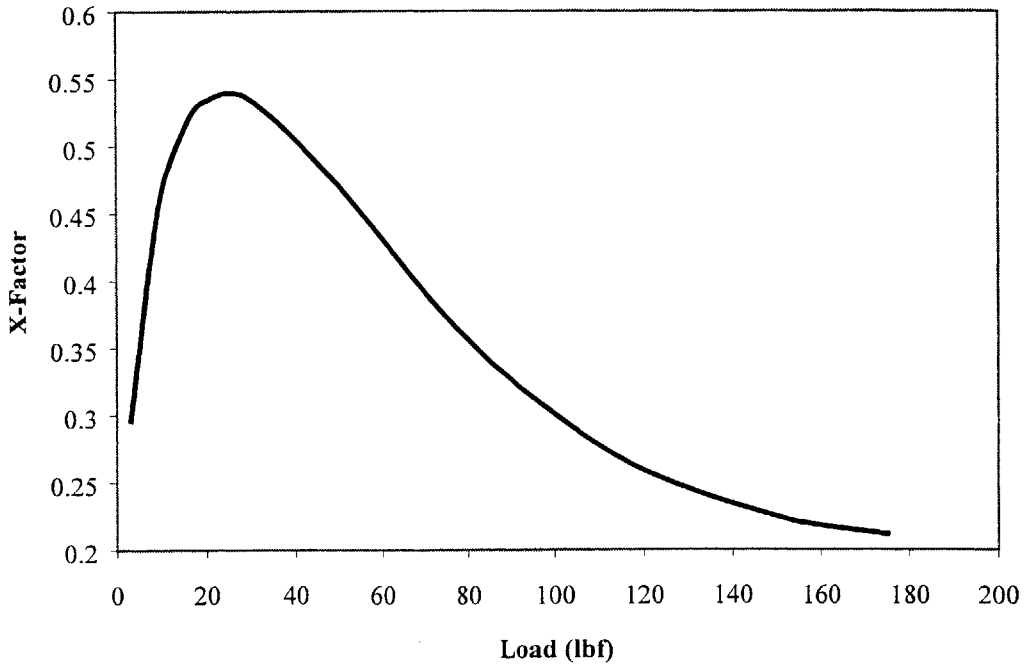

Figure 6.5 – X-Factor Correlations as function of Applied Load

6.3 Electromagnetic Characterization

With the relationship between the electrical world and the mechanical world defined by Equations 6.15, the mechanical behavior of the valve could be modeled given the electrical input. Through theoretical relationships and the application of the X-Factor, the following dynamic modeling of the valves was undergone. As was done with the pressure blow down analysis of the previous chapter, this analysis was deigned as a step-wise integration that could be completed on Excel.

According to Faraday's Law, Equation 6.16 related the voltage across an inductor to the change in magnetic flux in the gap. The voltage across the coil is defined from the electrical circuit schematic shown in Figure 6.7.

$$V_{coil} = V_{in} - i_{observed} R_{coil} = N \frac{d\phi_{total}}{dt} \qquad \text{Eq. (6.16)}$$

Applying the X-Factor correlation, the following relationship for determining the change in total magnetic flux over time was determined.

$$\frac{d\phi_{total}}{dt} = \frac{1}{N}\left[V_{in} - R_{coil}\left(\frac{gap_{theoretical}\phi_{gap}}{N\mu_0 A_{core} X} \right) \right] \qquad \text{Eq. (6.17)}$$

This relationship allowed a stepwise integration of the magnetic flux to be completed.

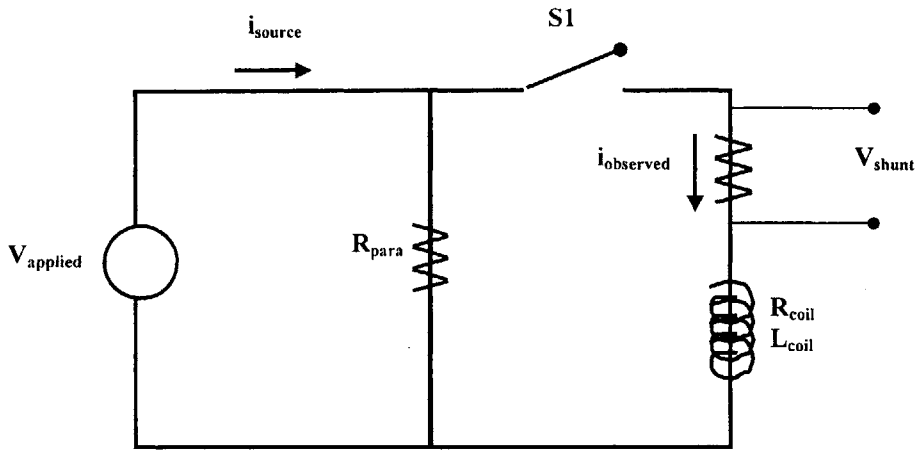

Figure 6.7 – Simple Circuit Schematic of Valve Driving Circuit

Equation 6.17 related the electrical world to the magnetic world. From this, it was simply a matter of relating in the magnetic world to the mechanical world. Using the free body schematic shown in Figure 6.8, a force balance on the Ferromagnetic Core yielded Equation 6.18

$$m_{core}\frac{dvel_{core}}{dt} = F_{mech} - F_{applied} \qquad \textbf{Eq. (6.18)}$$

Substituting the relationship between applied force and magnetic flux into Equation 6.18 resulted in Equation 6.19. This related the velocity of the ferromagnetic core to the magnetic flux in the gap and thus the applied voltage and coil current.

$$\frac{dvel_{core}}{dt} = \left[\frac{F_{mech} - \frac{\phi_{gap}^2}{2\mu_0 A_{core}}}{m_{core}}\right] \qquad \textbf{Eq. (6.19)}$$

Given the relationships of Equation 6.17 and 6.19, it was possible to apply a stepwise integration to determine the magnetic flux, core velocity and thus, the air gap geometry over time. Equation 6.20 gives the air gap geometry.

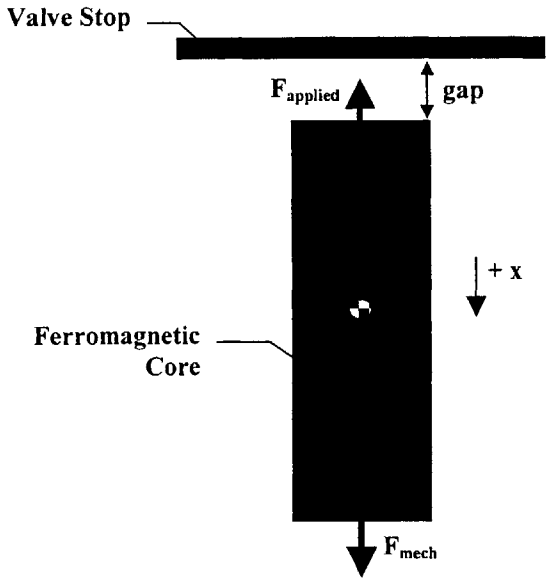

Figure 6.8 – Free Body Schematic of Ferromagnetic Core

$$gap_i = gap_{i-1} + vel_{core,i}dt \qquad \textbf{Eq. (6.20)}$$

However, for this method of integration, this equation held true only between the times after the magnetic force exceeded the applied force and before the ferromagnetic core reached the stops. The ferromagnetic core did not begin moving until $dvel_{core}$ obtained a negative value and ceased moving when the air gap reached zero.

A method for completing this analysis on a similar electromagnetic circuit appears in Appendix E- X-Factor Development. This analysis was combined with the analysis associated with section 6.2- X-Factor Correlation Development.

CHAPTER 7- Total Valve Dynamics

Several quantities factor into the total dynamics of the valve. All analysis to this point was leading to the modeling the motion of the valve while the valve operated in with the Coolpower 150. The analysis presented here and in previous chapters was intended to act as a guide for carrying out the same analysis on similar electromagnetic circuits and cryocooler combinations. Factoring into the total dynamics of the valve was the blow down dynamics, the electromagnetic dynamics and the electrical circuit dynamics. In this chapter, the blow down dynamics and electromagnetic analysis are integrated with two types of electrical circuits. Unlike the analysis of Chapter 6, this analysis incorporated the dynamic forces that acted on the valve throughout its motion. The electrical circuits are presented to act as tools for designing an external controller to drive the EM valves.

One circuit that used a step function in voltage to drive an EM valve is presented. The other used a simple RC circuit drove an EM valve. In the following pages, these two types of circuits are analyzed in concert with the preceding blow down analysis of chapter 5 and the electromagnetic analysis of chapter 6. First, the methodology of the previous chapters was combined to present a single set of equations that were used to describe the dynamics of the valve under a constant voltage input. Next, the dynamics of a simple RC circuit were incorporated into this system.

By the end of this chapter, the complete procedure for analyzing the opening motion of an EM valve operating in concert with a G-M cryocooler is presented. This methodology was then intended to be applicable to future EM valve designs of similar configuration.

7.1 Valve Dynamics Driven by a Step Input

Chapter 6 presented a free body analysis of the Ferromagnetic Core under a prescribed load. For the purpose of developing the X-Factor, this was sufficient. When operation in the cold head, several dynamic and static forces were acting on the Ferromagnetic Core. These forces arose from the dynamic pressure acting on the Valve Head, the static backpressure acting on the Valve Seat, the dynamic force required to compress the spring, the preload force in the spring and the dynamic magnetic force acting in the air gap. Figure 7.1 presents a modified free body schematic that incorporates the forces acting on the valve during operation.

Rewriting Equation 6.16 to reflect the actual forces acting on the Ferromagnetic Core results in Equation 7.1.

$$\frac{dvel_{core}}{dt} = \left[\frac{F_{preload} + k_{sp}\left(gap_{initial} - gap_i\right) + F_{DP} - F_{BP} - \frac{\phi_{gap}^2}{2\mu_0 A_{core}}}{m_{core}} \right] \quad \textbf{Eq. (7.1)}$$

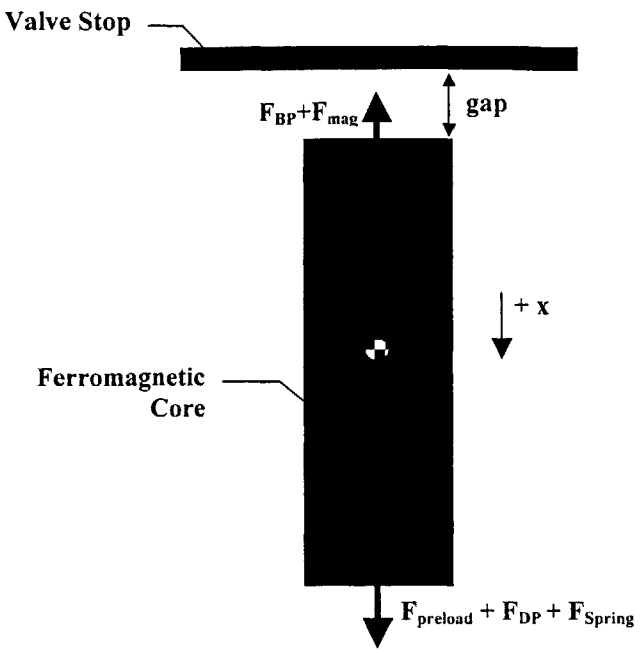

Figure 7.1 – Free body Schematic of Ferromagnetic Core using actual loads.

This defines the change in velocity over time. On the right hand side of 7.1, there are only two terms that do not very over time. These are the preload force in the spring and the force exerted by the static backpressure on the valve seat.

In chapter 6, the dynamics of the magnetic flux and air gap geometry were determined. The change in magnetic flux and the length of the air gap at any time were defined by the governing relationships of Equations 7.2.

$$\frac{d\phi_{total}}{dt} = \frac{1}{N}\left[V_{in} - R_{coil}\left(\frac{gap_{theoretical}\phi_{gap}}{N\mu_0 A_{core} X_{current}}\right)\right]$$

Eq. (7.2)

$$gap_i = gap_{i-1} + vel_{core,i}\,dt$$

The step-wise integration of these two equations defined the magnetic force and the dynamic spring force over time.

Chapter 5 presented an analysis of the blow down of the cold volume over time. The change dynamic pressure over time was defined as in Equation 7.4.

$$\frac{dP_{CV}}{dt} = \dot{m}_{CV} \cdot \gamma\left[\left(\frac{\forall}{R_{He}}\right)\left(\frac{P_H}{T_0}\right)\left(\frac{P_{CV}^{\frac{1-\gamma}{\gamma}}}{P_H^{1/\gamma}}\right)\right]^{-1}$$

Eq. (7.3)

The mass flow rate from the cold volume was defined by either a choked flow regime or a unchoked flow regime. The mass flow rates for each regime are defined in Equations 7.4.

$$\dot{m}_{choked} = \left(\frac{A_{curtain}}{\sqrt{T_0}}\right)\left[\left(\frac{\gamma}{R_{He}}\right)^{1/2}\left(\frac{\gamma+1}{2}\right)^{\frac{1-\gamma}{2(\gamma-1)}}\right]\frac{P_{CV}^{\frac{\gamma+1}{2\gamma}}}{P_H^{\frac{1-\gamma}{2\gamma}}}$$

Eq. (7.4)

$$\dot{m}_{unchoked} = A_{curtain}\left[\frac{5}{R_{He}T_0}\cdot\left(\frac{P_L^{\frac{\gamma+1}{\gamma}}}{P_H^{\frac{1-\gamma}{\gamma}}}\right)\cdot\left(\left(\frac{P_{CV}}{P_L}\right)^{\frac{\gamma-1}{\gamma}}-1\right)\right]^{1/2}$$

Recall that the flow regime was determined by the ratio of the backpressure to the dynamic pressure.

Additionally, each of the flow rates is dependant on the geometry of the air gap. The curtain area of the valve changes dynamically with the air gap geometry according to Equation 7.5.

$$A_{curtain} = \pi D_{port}(gap_{initial} - gap_i)$$

Eq. (7.5)

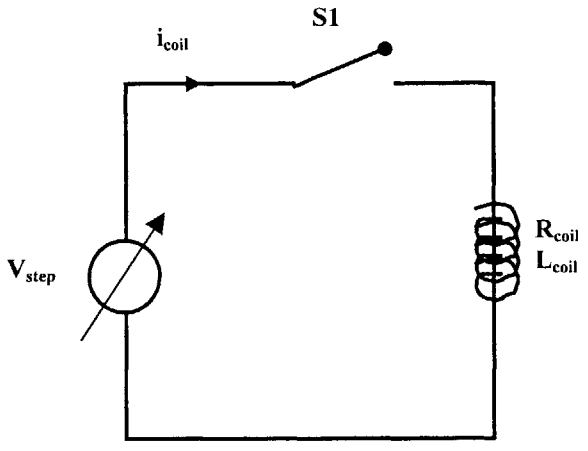

Figure 7.2 – Electrical Circuit Schematic for Step Input Analysis

Figure 7.2 repeats the circuit used to complete the Electromagnetic Dynamics. In this circuit the electrical controller is represented by the voltage source. This voltage source appears in Equation 7.1 as the term V_{in}. In this case, this quantity is treated as a step function with a variable magnitude.

Equations 7.1 through 7.4 were combined and a step-wise integration was completed for the dynamics of the valve. In successive integrations, the value of the applied voltage was varied to examine the behavior of the valve for varying inputs.

It was desired to tailor the input to the valve so that the air gap reached zero length at the same time the velocity of the Ferromagnetic Core reached zero. This provided the soft and controlled opening of the valve. This was accomplished at an input voltage of 23 Volts. With this voltage input, the air gap reaches zero length at 0.1347 second after the step input is applied. At zero length the core hits the stops with a -0.934 m/s velocity. Figure 7.3 shows the air gap geometry and the core velocity as a function of time. Figure 7.4 shows the dynamic pressure as a function of time.

A detailed examination of this analysis appears in Appendix F- EM Relationships

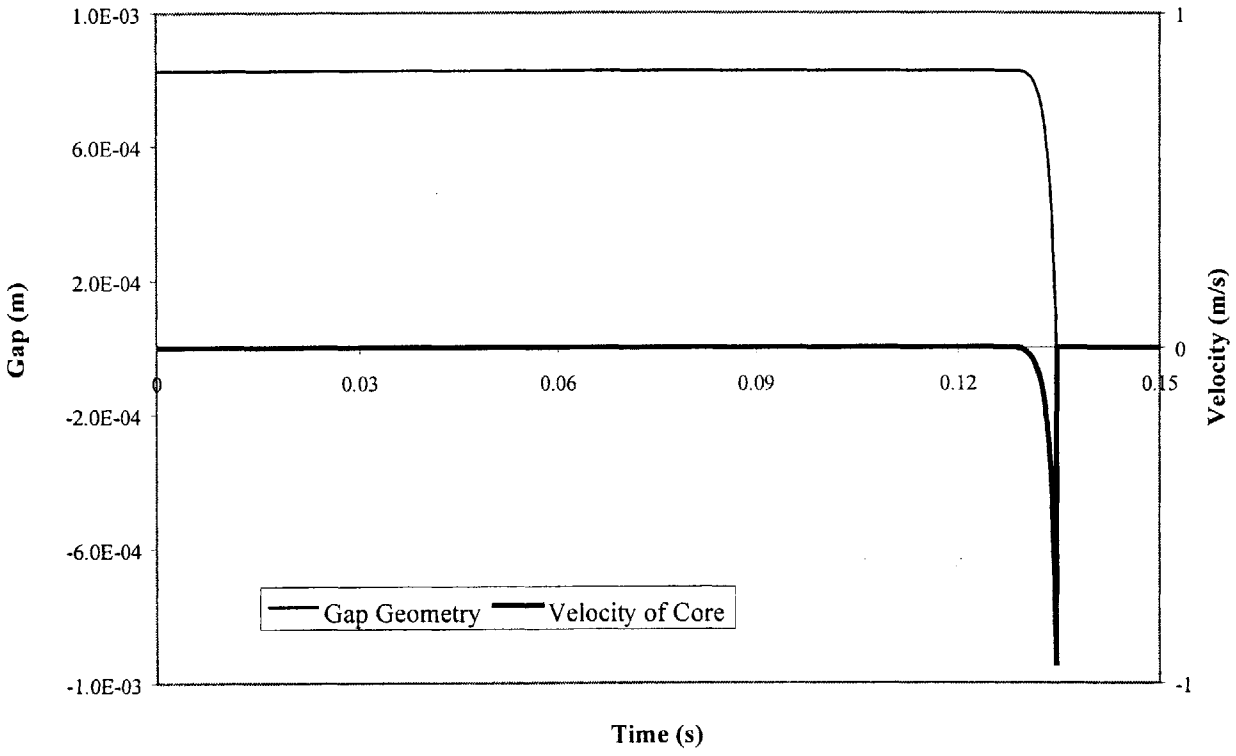

Figure 7.3 – Air Gap Geometry and Ferromagnetic Core Velocity for Step Input

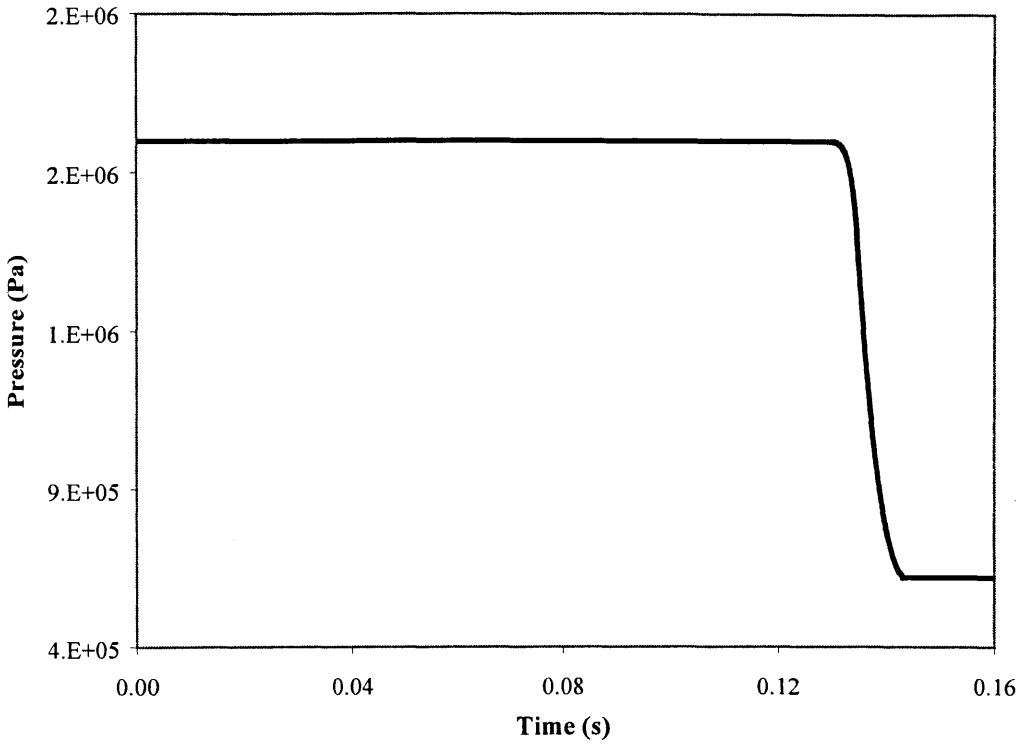

Figure 7.4 – Dynamic Pressure as a function of time for step input

7.2 Valve Dynamics Driven by an RC Circuit

In the previous section, the controller input was considered to be a constant voltage source with a perfect step input. This analysis assumes a perfect voltage source and step input. However, upon examining the behavior of the valve with varying inputs, it was also determined that the electromagnetic circuit was highly sensitive to fluctuations in voltage input and to slight variances in the magnitude of the input. The difference of a few tenths of a volt could determine whether or not the valve had enough inertia to reach a zero length air gap. This meant incorporating a more stable and predictable voltage source into the driving circuit.

Figure 7.5 presents the RC circuit schematic used to drive an EM valve. In this circuit the voltage source was replaced with a capacitor. Switches S1 and S2 were incorporated to control when the capacitor was charged by the source and when it was discharged into the electromagnetic circuit.

For this analysis, the circuit begins with switch S1 closed and switches S2 and S3 open. The capacitor was initially charged to the voltage prescribe by the voltage source. This value was treated as variable for this analysis. At time zero, simultaneously, switch S1 opens switch S2 closes and switch S3 remains open. At this time, the capacitor begins to discharge into the electromagnet. The voltage begins at the prescribed voltage and changes with time according to Equation 7.6.

$$\frac{dV_{cap}}{dt} = \frac{i_{coil}}{C} \qquad \text{Eq. (7.6)}$$

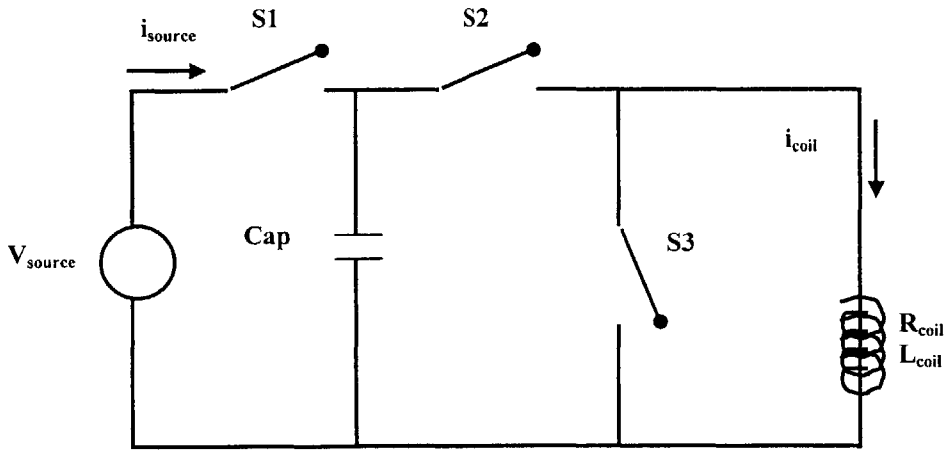

Figure 7.5 – Electrical Circuit Analysis for RC Circuit Analysis

Through a step-wise integration, Equation 7.6 allowed the voltage of the capacitor to be determined over time. Once the capacitor fully discharged and reached zero volts, switch S2 was opened, switch S3 was closed. This prevented negative voltage on the capacitor. Switch S1 was again closed to recharge the capacitor for the next cycle. This voltage was then incorporated into the total valve dynamics by replacing V_{in} with V_{cap} in Equation 7.2. This substitution appears in Equation 7.7.

$$\frac{d\phi_{total}}{dt} = \frac{1}{N}\left[V_{cap} - R_{coil}\left(\frac{gap_{theoretical}\phi}{N\mu_0 A_{core} X_{current}}\right)\right] \qquad \text{Eq. (7.7)}$$

Equation 7.7 was used in conjunction with the analysis laid out in the previous section to describe the valve dynamics when an RC circuit drove the EM valve. The source voltage and capacitor value were then varied until the gap geometry was able to reach zero from the initial input. This occurred when the capacitor was 310 μF and the source voltage was 200 Volts. As seen in Figure 7.6, the air gap reaches zero length at 0.01325 second with a velocity of –0.504 m/s. Figure 7.7 show the dynamic pressure in the cold volume as a function of time.

It was also observed that once the Ferromagnetic Core reached the stops, the coil

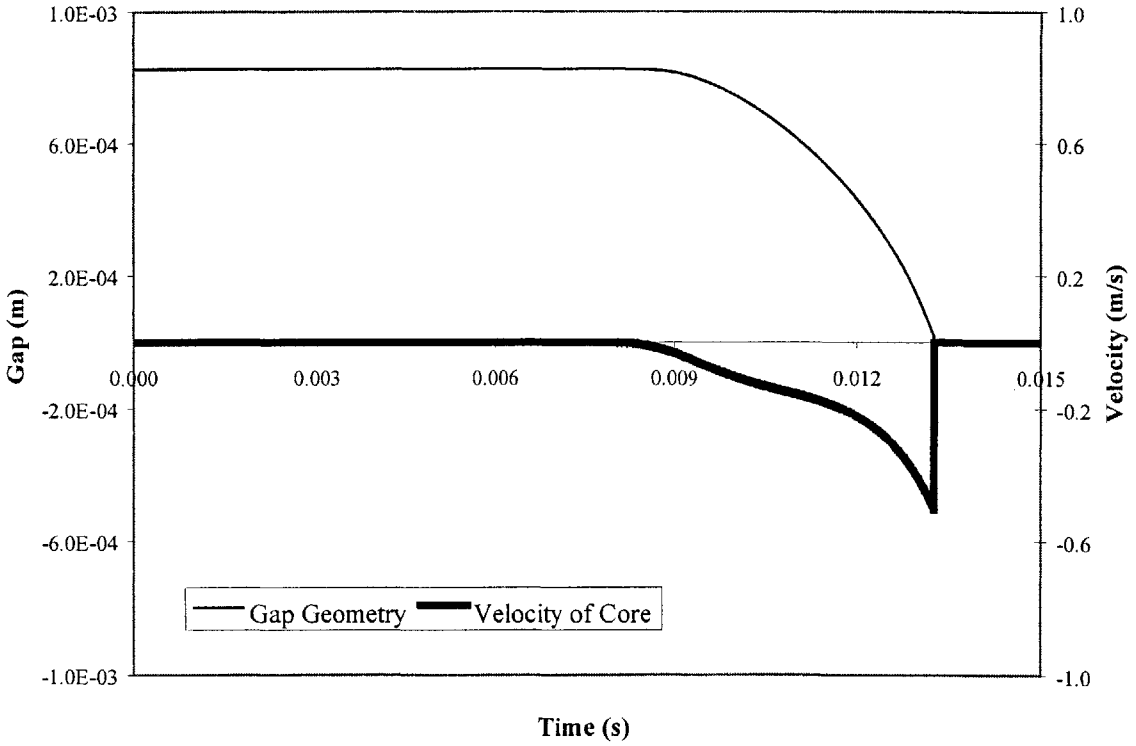

Figure 7.6 - Air Gap Geometry and Ferromagnetic Core Velocity for RC Input

current was still 1.6 A. It was determined that only approximately 0.1 A of current was required to hold the valve open against the force of the spring. Therefore, once the capacitor fully discharges and the Ferromagnetic Core reaches the stops, it was suggested that a resistor be put inline with switch S3 to remove the excess coil current while maintaining sufficient current to hold the valve in the open position. This may require an additional switch and a 'hold open source' to be added to the right of the coil in the schematic presented in Figure 7.5

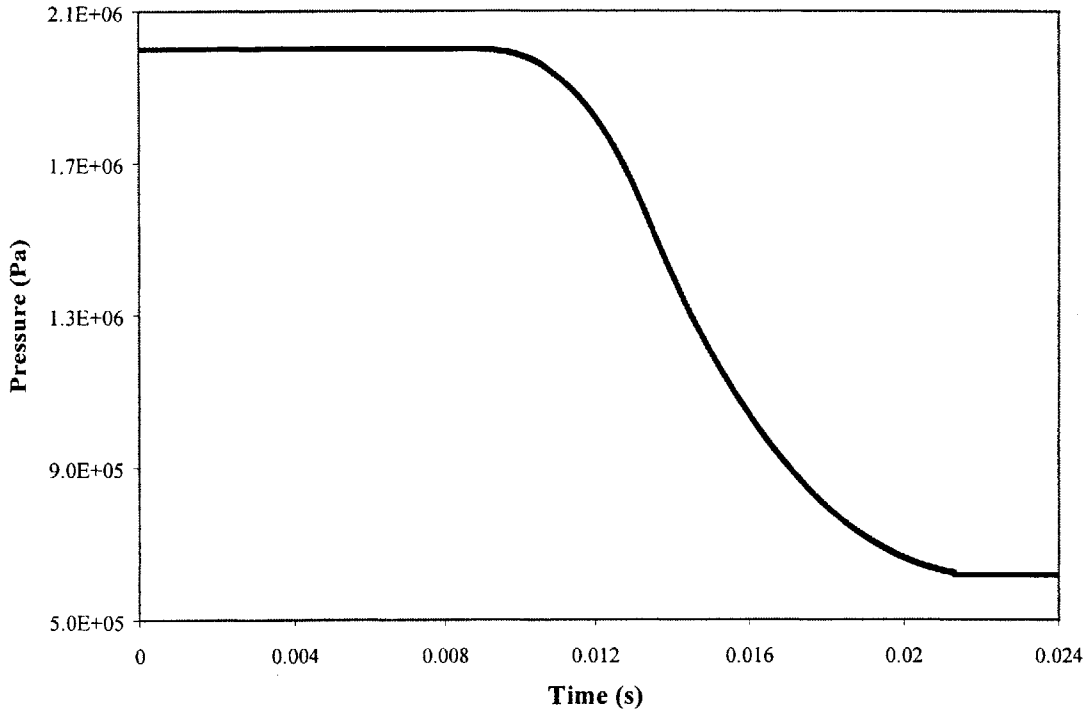

Figure 7.7 - Dynamic Pressure as a function of time for RC input

7.3 First Law Energy Balances

On of the important factors in the valve design was minimizing the resistive heating that occurred in the coil. Recall that in the Boreas Valve, excessive resistive heating meant that the coil must be continuously cooled by the low temperature working fluid. This meant that the cooler had to reach a low temperature before the valves were operated. Here, it was desired to operate the valves constantly with cryocooler operation, whether during the cool down time to once the final refrigeration temperature was reached. Therefore, in order to fully understand the behavior of the EM valves, it was necessary to understand how the energy was consumed throughout the valve motion. This was achieved again using step-wise integration techniques and applying them to the RC driven circuit. Using quantities defined in previous sections, the energy balance was derived.

This analysis consisted of balancing the energy input into the system with the useful energy used to move the core and the energy lost to various sources. Figure 7.8 presents a block diagram that depicts how the energy flowed through the system beginning with the energy input from the voltage source. From this diagram it can be seen that the Equations 7.8 must balance.

$$E_{capacitor} = E_{resistor} + E_{kinetic} + E_{F_{\Delta P}dx} + E_{spring} + E_{stored,gap} + E_{stored,other}$$

$$E_{fmag} = E_{kenetic} + E_{F_{\Delta P}dx} + E_{spring}$$

$$E_{stored,mag} = E_{stored,gap} + E_{stored,other}$$

Eq. (7.8)

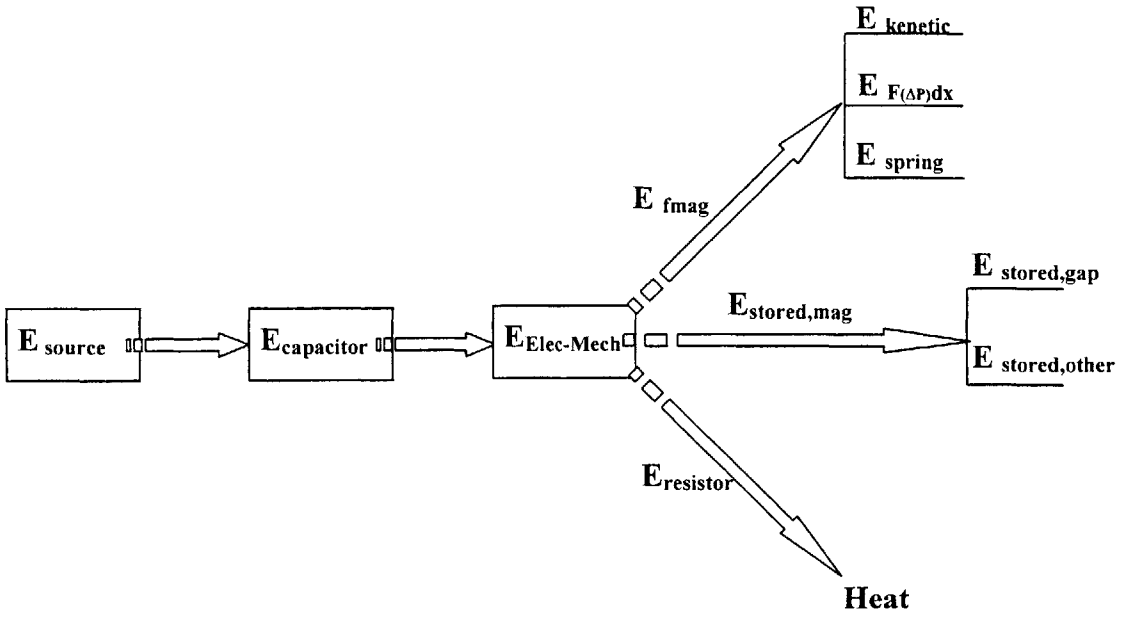

Figure 7.8 – Block Diagram of Energy Flow in the System

Each of these terms is defined in Equations 7.9 in differential form.

$$\frac{dE_{capacitor}}{dt} = V_{cap} i_{coil} \qquad dE_{kenetic} = \frac{m_{core}}{2} \Delta\left(vel_{core}^2\right)$$

$$dE_{Fmag} = F_{mag} dx \qquad dE_{spring} = k_{sp} \Delta gap$$

$$dE_{resistor} = i_{coil}^2 R_{coil} dt \qquad dE_{F_{\Delta P} dx} = \left(F_{DP} - F_{BP}\right) \Delta gap$$

$$dE_{stored} \frac{\Delta\left(\phi_{total}^2 gap\right)}{2\mu_0 A_{coil}} \qquad dE_{stored,gap} = \frac{\Delta\left(\phi_{gap}^2 gap\right)}{2\mu_0 A_{coil}}$$

$$dE_{stored,other} = dE_{stored} - dE_{stored,gap}$$

Eq. (7.9)

The capacitance and input voltage determined in the previous section were used to integrate these values over time. At the moment the core hit the stops it was found that a substantial amount of the energy produced by the capacitor discharge went to producing a non-force producing magnetic field. With a source input of 200 Volts and a capacitor specified at 310 μF, it reached the valve stops in 0.01325 seconds. This was in comparison to the completion of the blow down process taking 0.0213-second after the valve motion begins. During the opening motion, the valve loses 21% of its input energy to coil heating. At an initial temperature of 80K with a 2.3 Ω coil resistance, this translated to approximately a 1.33 joule degradation to the G-M cycle.

A detailed examination of the analysis of the previous two sections appears in Appendix G- Applying the X-Factor.

CHAPTER 8- Discussions and Conclusions

In the 1980s, Crunkleton and Smith proposed a new cryocooler design that would produce reliable 4.5 K refrigeration. This cryocooler was intended to exceed the cooling capacity of a typical G-M cryocooler to sub 10 K refrigeration capacities. This was the Boreas cryocooler. In the tradition of the Boreas cryocooler design, Smith proposed another cryocooler cycle design that was influenced by this previous work. One component of this new cycle was to incorporate cold Electro-mechanical valves to drive the flow in a unidirectional circuit within the cryocooler.

Work by Jones, proved that a free-piston expander could be successfully designed and incorporated into a cryocooler cycle to perform expansion processes. The designing and testing of the cold Electro-mechanical valves presented in this thesis was the next step that continued the development of the new cryocooler cycle. Here, phase I, cold Elerctro-mechanical valves were designed to operate in conjunction with a cryocooler. The working fluid was to be used as a cooling mechanism and thus, the valves were placed inline in a unidirectional flow loop. In this thesis and for phase I testing purposes, a donated and pre-existing G-M cryocooler was modified to drive the unidirectional external flow loop. The EM valves were incorporated into a G-M Cryocooler and placed into the system at the interface between the cold volume of the G-M cryocooler and the external flow loop. Phase II of this project will incorporate a similar and smaller version of these EM valves, which will be operated in conjunction with the free-piston expander developed by Jones.

In the preceding seven chapters, development, analysis and testing of the phase on EM valves was presented. Several design tools that can be incorporated into the phase II EM valve design were discussed and presented. From the design and testing of these valves various conclusions were drawn concerning the performance of the cold EM valves proposed here. In the remaining pages of this thesis these conclusions are presented and discussed in detail.

8.1 Valve Design and Manufacture

In the design and manufacture of the cold EM valves, several design tools and innovative manufacturing processes were developed. The overall design of the valve itself presented a configuration that improved on the Boreas valve configuration. A flexure design tool was developed for designing and manufacturing flat, thin constant radius flexures. Since these EM valves operated inline with the working fluid of the cycle, an unhindered flow passage was incorporated into the design. This required proposing a ferromagnetic cage design into the magnetic circuit. Additionally, a technique for reducing eddy currents in the electromagnetic circuit was incorporated. This entailed using a new technique for manufacturing the ferromagnetic core. In this section, each of these items will be addressed in further detail.

The Boreas valve opened into the cold volume. The valve sealing force was provided by a flexure spring that was integral with the valve disk/valve head . The major sealing force was provided by the pressure difference across the valve which acted as an exhaust valve for the expander. The limited sealing force at zero pressure difference tended to cause valve leakage until sufficient pressure was developed in the cold volume.[1,17] The

EM valves proposed in this thesis moved the valve spring and the flexure guides outside of the cold volume. A valve stem attached to the valve head allowed the external valve stem to pull the valve closed. The two flexures that guided the Ferromagnetic Core also guided the valve head on the end of the valve stem. As in the Boreas valve, the spring force added to the pressure force giving an adequate sealing force.

The EM valves proposed in this thesis moved the valve seat inside of the cold volume and presented an inward opening valve configuration. In this configuration, the pressure differential aided the sealing of the valve. Instead of the pressure force working against the valve spring the pressure worked in concert with the valve spring to seat the Valve head. Thus the sealing force required by valve spring was greatly reduced and only moderately stiff compression spring was specified for closing the valve. This design also required a pulling force to seat the Valve Head, which allowed the compression spring to act only on the Valve Stem.

In creating a low loss valve, low- and no- friction concepts were introduced in this design. As the only moving assembly in this design, the Head-Stem-Core Assembly had no sliding surfaces. This was achieved by maintaining this assembly centered in the two primary orifices of the Electromagnetic Circuit via Multi-leaf Flexure Assemblies. Through traditional thin curved beam analysis, a constant radius flexure design successfully provided enough radial stiffness to prevent the Ferromagnetic Core form being off set inside of the orifice. To prevent the flexures from interfering with the axial motion of the valve head, the flexures had an axial stiffness that was small in comparison to the stiffness of the valve spring.

The flexure analysis incorporated a significant safety factor and calculated the stress levels throughout the beam span to ensure a long life of the flexures. All stressed induced in the flexures throughout the valve motion were well within material constraints. For future EM valve designs, a methodology for undergoing a similar thin curved beam analysis was presented.

Since the valves were to be cooled by the working fluid in the cycle, it was also necessary to ensure that a complete flow path existed throughout the length of the valve. The only assembly for which this requirement proved difficult to meet was in the Electromagnetic Circuit. This assembly was a single, self-contained unit that contained the Electromagnetic Coil. Flow passages were incorporated into the assembly through a slotting procedure that produced eight 0.010-inch wide, axial flow passages at the outermost circumference of the Electromagnetic Circuit. From this procedure arose the Magnetic Cage concept. The Magnetic Cage acted as the Back Iron in the Electromagnetic Circuit where the slotting procedure introduced the fluid pathway about the Electromagnetic Coil and resulted in the 'cage' configuration of this component.

Finally, an innovative manufacturing concept was incorporated in the Ferromagnetic Core. Eddy currents can arise in an electromagnetic circuit when a circumferential path in circuit is available. Therefore, it was critical that these pathways be reduced and/or eliminated in the circuit. Slotting the Back Iron successfully broke the circumferential path in that part of the circuit. Applying a similar slotting procedure to the Ferromagnetic Core proved to degrade circuit performance by significantly reducing the cross-sectional area of the core.

To disrupt the circumferential path about the Ferromagnetic Core, a new manufacturing procedure was introduced. This procedure successfully divided the

Ferromagnetic Core into four equal radial quadrants without sacrificing the cross-sectional area of the core.

A positive consequence of incorporating this procedure was the increase in precision of the center hole in the Ferromagnetic Core. Through the alignment of the four quadrants a straight pilot hole was created. This resulted in decreased tool deflection when milling the stem clearance hole and thus, the end-to-end center hole precision was improved.

These EM valves presented greatly improved sealing over that of the Boreas valves. Parts were designed to be manufactured using traditional machining techniques that could be completed during in-house operations. The centering of the valve was achieved with two Multi-leaf Flexure Assemblies per valve. The working fluid was used to cool the electromagnetic coil by discreet flow passages about the circuit and eddy-current-eliminating circumferential current pathways about the Ferromagnetic Core reduced losses.

8.2 Thermodynamics and Fluid Dynamics

To test the EM valves, they were to operate in collaboration with a pre-existing G-M cryocooler system. The performance of this pre-existing system was understood and documented by the manufacturer. Using the oscillating pressures of the G-M cycle, these valves were to drive a flow loop external to the G-M system. This allowed for the cold EM valves to be placed inline with the external flow loop for testing. The performance of the modified system could then be compared with the known performance of the pre-existing system to quantify the performance of the EM valves. This required examining how the external flow loop affected the system parameters and how the valves themselves affected the displacement of fluid throughout the system.

First the thermodynamic performance was examined. Typically, a G-M cycle required a refrigeration load to be conduction cooled in direct contact with the expansion volume. By adding the external flow loop to the system, the refrigeration load was moved to a heat exchanger inline with the flow loop. Additionally, a large surge volume that remained at a pressure only differentially higher than the system-low pressure was placed inline with the flow loop.

In reference to the cold expansion volume, a G-M cycle consists of two constant-volume and two constant-pressure processes. The EM valves were designed to drive the external flow loop during the constant volume expansion process. This added two new states and a new process to the cycle. When the exhaust valve was opened, the cold volume adiabatically expands into the surge volume. The flow proceeds through the surge volume to the heat exchanger. Once the surge volume pressure was reached, the intake EM valve opened and the exhaust EM valve closed and the circulating mass is returned to the G-M system.

The combination of adding new equipment to the cycle, changing the cycle itself and moving the refrigeration load results in degrading the performance of the original system. The Leybold Coolpower 150 was designed to provide 150 Watts of cooling capacity at 77 K. A first order thermodynamic analysis of the original G-M system and the system modified with the external flow loop yielded an approximation for how the system was degraded through the modifications.

On a first approximations basis, the regenerator performance and mass circulating at the cold end of the regenerator were considered unchanged by the modifications. This allowed the refrigeration capacity to be maintained at 150 Watts. The degradation in the system was realized in the refrigeration temperature. Opening the exhaust at near system-high pressure and closing it at near system-low pressure resulted in raising the refrigeration temperature from 77 K to 82 K. It was believed that this was not so much a result of the additional adiabatic expansion process but more so an affect that resulted from moving the refrigeration load away from the cold expansion volume.

Integrally related to the thermodynamic performance of the system was the fluid dynamic behavior of the fluid throughout the process. The new process proposed that the fluid to be adiabatically blown down from the expansion volume through the small orifice of the valve. The performance of this process was calculated, but the time to complete the adiabatic blow down was undefined. This time was necessary in evaluating the action of the valves in comparison with the dynamics of the flow. This analysis also established the pressure differential across the valve head. The dynamic force resulting from this pressure differential acted directly on the Ferromagnetic Core and factored into the total dynamic behavior of the valve.

To quantify the dynamic pressure in the cold volume it was necessary to understand whether the flow regime was choked or unchoked. Developing a set of equations for each flow regime and establishing the pressure ratio at which the flow would change from choked to unchoked flow established a method for modeling the blow down dynamics of the process. All equations incorporated adiabatic relationships for the analysis.

This initial analysis started with the fluid at system-high pressure and proceeded to system-low pressure. The pressure in the cold volume estimated with a step-wise integration that evaluated the change in pressure in the cold volume differentially with 0.1 ms time steps. The cross-sectional area of the orifice was taken as the full open curtain area of the valve. Under these conditions the process took 0.01001 second. The flow remained choked for 0.00284 second. These calculations were also incorporated in a design tool that can be applied to the performance of valves with similar configurations.

Overall, from first order approximations, the addition of an external flow loop degraded the system performance by raising the refrigeration temperature to 79K at a capacity of 150 Watts. This indicated not only that the external flow loop would not seriously degrade the performance of the G-M system used here but also that it was feasible to incorporate the EM valves with minimal thermodynamic loss. The blow down analysis also factors into the dynamics of the valve motion and was incorporated into the total valve dynamics package.

8.3 Electromagnetic Circuit

Given the geometry of the valves and understanding that it was feasible to drive these valves with the oscillating pressures of a G-M cycles, it was necessary to understand the physical characteristics of the Electromagnetic Circuit. As stated previously, this cold EM valve configuration resembled configurations typically used in solenoid valves. However, the defining difference between the cold EM valves and solenoid valves, is that position, velocity, acceleration and jerk profiles of the EM valves were to be controllable and predictable.

A typical solenoid operated on a 'slam-slam' philosophy. This philosophy being that the electromagnetic circuit was initially given enough voltage to open the valve, slamming the core into the valve stops. The voltage was then cut and the valve was allowed to simply slam shut under the action of a compression spring. The only electromagnetic characteristic necessary in solenoid valve design was the amount of voltage required to give the core enough initial velocity to reach the valve stops. This caused solenoid valves to be inefficient with large impact forces. The result is that most solenoid valves have a short operating life.

On the other hand, this thesis sought to understand and characterize the physical behavior of the electromagnetic circuit. This characterization led to the development of relationships that could be applied along with control theory concepts to design a controller for the EM valves. Unlike solenoid design, this process attempted to understand the behavior of the valve for all possible gap geometries. Here, the electromagnetic circuit's behavior throughout its motion was understood so that a prescribed and shaped input could be input to the valve. The result of this input would be a prescribed and shaped output valve motion. This would eliminate the 'slam-slam' motion associated with a typical solenoid valve.

In order to begin shaping the output motion of the valve head, the electromagnetic circuit had to be characterized experimentally. It was known that magnetic field losses caused by imperfect magnetic flux linkage, eddy currents, electromagnetic circuit geometry and orifice air gaps existed. These losses were termed the non-force producing magnetic fluxes. No simple lumped parameter theory existed to specifically characterize these non-force producing magnetic fluxes. Initially, these non-force producing magnetic fluxes were believed to exist in one of two categories. Either a series flux loss or a parallel flux loss.

Initially, relationships were developed that specifically quantified these two categories of non-force producing magnetic flux. It was then attempted to fit these relationships to experimental data and design empirical relationships for the series and the parallel non-force producing magnetic flux. These attempts failed to derive linearly independent relationships. Instead, it was determined that the two non-force producing magnetic fluxes and the force producing magnetic flux were indeed linearly dependent upon each other. Thus, it was not possible to specifically quantify independent formulas for each of these terms.

Understanding that the three flux paths were linearly dependant upon each other meant that the data needed to be correlated into a different empirical formula. Rather than attempting to examine each of the three fluxes independently, it was attempted to characterize a ratio of the force producing magnetic flux to the non-force producing magnetic flux.

The non-force producing flux was compared to the force producing flux by designing the X-Factor. The X-Factor characterized the empirical ratio between the observed coil current and the theoretical coil current required to provide a given load at a given air gap. The observed current came from experimental data. The theoretical current arose from calculating the current that was expected given the external load force applied to the Ferromagnetic Core. This empirical X-Factor was derived from the experimental current-air gap relationship. It was observed that for a given applied load force, the current-air gap relationship was linear. Examination of the slopes of the current-air gap

plots versus external load force yielded the following two empirical relationships for the X-Factor. The first applies to the English system of units and the second applies to the Metric system of units.

$$X = \sqrt{\frac{2F_{applied}}{\mu_0 A_{core} N^2}} \cdot 0.003\left(\frac{in}{Amp}\right) + 0.065\left(\frac{in}{Amp}\right) \cdot \exp\left[-0.115\left(\frac{1}{lbf}\right)\left(1.09lbf + F_{applied}\right)\right]$$

Eq. (8.1)

Equations 8.1 were the definitive result characterizing the physical behavior of the electromagnetic circuit. For a given external load force, these empirical relationships quantify a relationship that defines how the electromagnetic circuit performed in comparison to the how the electromagnetic circuit was theoretically expected to perform. The next step in the design process was to apply X-Factor relationships to the Electro-mechanical dynamics of the EM valves. A procedure was also defined for designing the X-Factor for similar electromagnetic circuits in future design work.

8.4 Total Valve Dynamics

Up to this point all mechanical and magnetic factors influencing the dynamic behavior of the EM valves were defined. These factors included the adiabatic blow down dynamics, the compression spring dynamic and the electromagnetic behavior or the valve. So far, each of these components was defined as separated entity. It was also necessary to define the electrical circuit that was to drive the EM valves. The electrical circuit characteristics were to be defined as the input into the EM valve. Now, to fully define the dynamics of the EM valves, it was just a matter of incorporating the mechanical, magnetic and electrical components into a single system.

To begin the integration, an electrical circuit that provided a simple step voltage input was applied to electro-mechanical relationships that incorporated the empirical X-Factor relationship into the equations. This allowed the motion of the valve to be examined given a specified constant voltage input. This first step incorporated the electrical circuit with the magnetic circuit. A prescribed load was applied to the Ferromagnetic Core.

The next step in the integration process was to add the actual dynamic forces to the model. The simplest of these forces is the load resulting from the compression spring acting on the Ferromagnetic Core. Since this was a linear spring this step was simply a matter of calculating the preload on the spring and using linear spring relationship in conjunction with the air gap dynamics to determine the dynamic spring force.

It was known that another force acting on the Ferromagnetic Core arose from the dynamic differential pressure across the valve head and thus, influenced the motion of the valve. It was also recognized that the motion of the valve also related to the curtain area of the valve. The curtain area of the valve was dynamically linked to the air gap geometry. This was taken into account and the dynamic pressure in the cold volume was incorporated into the design.

All of these components were integrated into a single set of differential equations. These equations were then integrated in a step-wise manner with 0.1 ms time steps. Given a step voltage input of 23 Volts, the valve began to move 0.1287-second after the

initial input and the core reached the stops in 0.1345 second (0.0058 second after motion began) with an inertial velocity of -0.934 m/s. The fluid flow remained choked for 0.0114-seconds after valve motion begin. The blow down process was completed 0.0142 second after the initial voltage input.

Finally, a slightly more complex and dynamic RC circuit was incorporated into the design. This circuit replaced the step input to the EM valve with an input resulting from a capacitor discharge. In this final step, the energy flow through the system was examined at successive time steps throughout the process. This allowed an examination of how much work was going into creating the force producing magnetic field versus the amount of energy lost to coil heating and the amount of energy going into non-force producing magnetic field.

This circuit configuration replaced the step input and again, all components were integrated into a single set of differential equations. This set of differential equations included differential calculations of the energy flows in the system. The equations were then integrated in a step-wise manner with 0.1 ms time steps. For this set up the voltage source of 200 Volts and a capacitor of 310 μF allowed the valve to begin moving 0.00813-second. The core then reached the stops at 0.01325-second (0.00512-second after motion began) with an inertial velocity of –0.504 m/s. The fluid flow remained choked for 0.00652-second after valve motion began. The blow down process was completed 0.0213-second after the initial voltage input or 0.02049-second after motion began. Additionally, at the moment the valve reached the stops, approximately 3.5% of the energy input to the system went to the force producing magnetic field, while nearly 72% went to the non-force producing magnetic field and approximately 21.5% of the energy went to heating. 2.4% of the energy consumption went to the mechanical work of moving the core against the spring force and pressure. The remaining .6% of the energy went into inertial impact with the valve stops.

The integration of all components of the system yielded a design tool that described the dynamics and performance of the EM valves for a given electrical input. When an RC circuit drove this particular EM valve, the energy input to the system was primarily went to generating the non-force producing magnetic field and into the energy stored in the electromagnetic coil. Only a small fraction of the energy went into the force-producing magnetic field. This indicated that this particular valve configuration still exhibited significant inefficiencies. However, with such low velocities at the end of valve travel, it was also indicated that this configuration was an improvement over the typical solenoid configuration.

8.5 Conclusions

As stated in Chapter 1- Introduction, the original motivation of this project was to design a cold electro-mechanical valves that improved on the performance to of the Boreas valve. This EM valve design was intended to present the following three items:

1) A fully self-contained cold electro-mechanical valve with a single moving core using the working fluid of the cycle for cooling.
2) A new flexure bearing design to maintain friction-free valve displacement.

3) An analysis of physical characteristics of electromagnetic circuit that can be applied to designing controlled valve motion to minimize electrical inefficiencies.

The design itself presented a two-assembly valve design. First was the Valve Housing. This component was permanently fixed to the given system. Second was the Valve Assembly itself. Once fully assembled, the Valve Assembly presented a single fully self-contained unit that could be examined, tested and modified independent of the Valve Housing.

Integral in the Valve Assembly design was the flexure bearing design. Multi-leaf Flexure Assemblies were the basis for a friction free valve design. These Multi-leaf Flexure Assemblies held the only moving assembly, the Head-Stem-Core Assembly, centered in the two primary orifices of the Electromagnetic Circuit. Through basic stress analysis, the flexure design exhibited a high radial stiffness to maintain the Head-Stem-Core Assembly in a centered position while having a low enough axial stiffness as to not interfere with the motion of the valve. The stress analysis of each individual flexure also indicated that the flexures are sure to enjoy a long operating life.

The valve design itself is a nice outcome to this thesis. However, perhaps the most significant outcome of this thesis was the development of a procedure for characterizing the overall electro-mechanical dynamics of this valve. Through extensive experimentation and development, a methodology for collecting, correlating and organizing experimental data on electro-mechanical valves was designed. The procedure set forth in this thesis and detailed in the attached appendices was designed for application to future cold EM valve design work.

Pertaining to this particular EM valve design, the valve presented was fast-acting and the inertia of the Ferromagnetic Core play no significant role in the dynamics of the valve. With a source input of 200 Volts and a capacitor specified at 310 μF, it reached the valve stops in 0.01325 seconds. This was in comparison to the completion of the blow down process taking 0.2130-second after the valve motion begins. During the opening motion, the valve loses 21% of its input energy to coil heating. This translated to approximately a 1.33 joule degradation to the G-M cycle. The addition of an external flow loop itself degraded the cycle by increasing its refrigeration load to 79 K. Overall, the proposed valve design was feasible in obtaining the objective of presenting a low-loss cold EM valve. Phase II of this valve design incorporates designing a smaller version of this design to be used in conjunction with the Free-Piston Expander proposed by Jones. It is suggested that the design tools developed in this thesis for evaluating the electro-mechanical behavior of cold EM valves should be applied to this future design. These design tools can then be applied for designing the external controller intended to drive these valves in the flow loop.

References

1. Smith, J.L. Jr.; High Efficiency Modular Cryocooler with Floating Piston Expander; U.S. Patent No. 6,205,791, 2001

2. Crunkleton, J.A.; "A New Configuration for a Small-Capacity, Liquid-Helium-Temperature Cryocooler," *Cryocooler 7,* Plenum Press, New York (1992), pp. 187-196

3. Jones, R.E., Smith, J.L. Jr.; "Design of Experimental Free Piston Cryogenic Expander," *Advances in Cryogenic Engineering*, Vol 45, Plenum Press, New York (2000), p. 1485-1491.

4. Leybold Cyrogenics; Helium Compressor Manual; Leybold Cryogenics, 8 Sagamore Park Road, Hudson, NH 03051.

5. Leybold Cryogenics; Coolpower Coldhead, Operating Manual; Leybold Cryogenics, 8 Sagamore Park Road, Hudson, NH 03051.

6. Mischke, C.R. & Shigley, J.E.; Mechanical Engineering Design, 5th Edition, McGraw-Hill Inc, New York (1989).

7. Roark, R. & Young, W.C.; Formulas for Stress and Strain, 5th Edition, McGraw-Hill Inc., New York (1975).

8. Ceridon, K.M., Smith, J.L. Jr.; "Remote Cooling with a G-M Cryocooler by Use of Cold Electromagnetic Valves Driving an External Flow Loop," Presented June 2000 at the International Cryocoolers Conference in Keystone, CO; to be published in *Advances in Cryogenic Engineering*, Vol 46, Plenum Press, New York (2001).

9. Sonnetag, R.E. & Van Wylen, G.; Introduction to Thermodynamics, Classical and Statistical, 2nd Edition, John Wiley & Sons Inc., New York (1971).

10. Cravalho, E.G. and Smith, J.L. Jr.; Engineering Thermodynamics, Massachusetts Institute of Technology, Cambridge, MA (1992)

11. White, F.M.; Fluid Mechanics, 3rd Edition, McGraw-Hill Inc., New York (1994).

12. Fay, J.A.; Introduction to Fluid Mechanics, Massachusetts Institute of Technology, Cambridge, MA (1994).

13. Fitzgerald, A.E., Kinsley, C. Jr. and Kusko, A.; Electric Machinery, The Processes, Devices and Systems of Electromechanical Energy Conversion, 3rd Edition, McGraw-Hill Inc, New York (1961).

14. Hayt, W.H. Jr.; Engineering Electromagnetics, 4th Edition, McGraw-Hill Inc, New York (1981).

15. Cook, A.L. & Carr, C.C.; Elements of Electrical Engineering, John Wiley & Sons Inc, New York (1924).

16. F.K. Miller and J.G. Brisson, "Development of a low-dissipation valve for use in a cold-cycle dilution refrigerator." *Cryogenics*, vol. 39, Elsevier Science, Oxford, UK (1999), pp. 859-863.

17. Smith, J.L. Jr.; Exhaust Valve for a Gas Expansion System; U.S. Patent No. 5,211,372, May 18, 1993.

APPENDIX A- Flexure Analysis

A-I Curved Beam Loaded Perpendicular to the Plane of Curvature

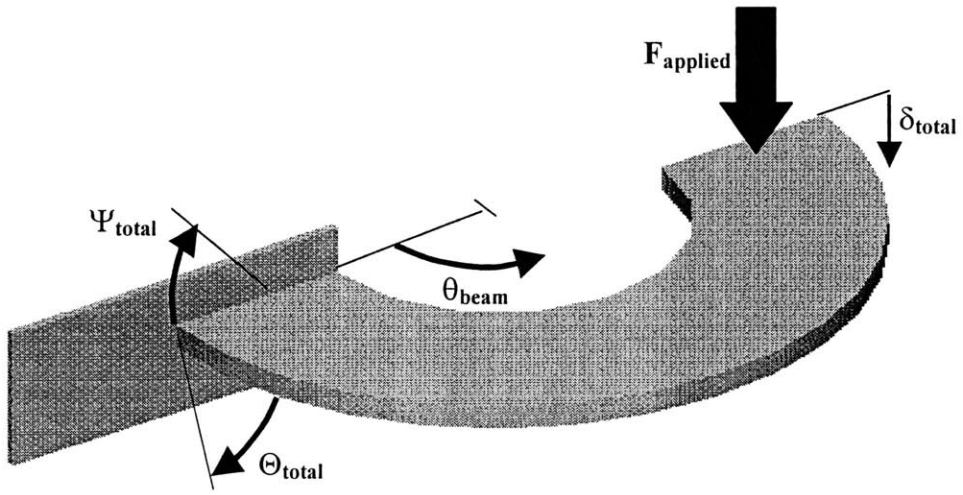

The above figure appeared in Section 3.4- Multi-leaf Flexure Assembly Design. The following development is in relation to this figure. All Equations were derived for Curved Beam Analysis from Roark and Young's Formulas for Stress and Strain and Mischke's Mechanical Engineering Design. The applied force arises from the axial deflection of 0.031 inches. Since the beam was considered clamped at both ends, the angle of rotation and the angle of twist the beam was defined by curved beams with one end fixed and one end free. To define a clamped end, the free end angle of rotation and angle of twist were limited to zero. The restoring moment and restoring torque were defined as the moment and torque that arose from returning the beam to these conditions once deflected by the applied force. The reactionary force, reactionary moment and reactionary torque at the fixed end were calculated and applied to the internal bending stress and internal shear stress calculations.

Case 1:Concentration Intermediate Lateral Load. One end fixed and one end free.

$$\delta_1 = \frac{-F_{axial}R^3}{E_{ss}I_{xx}}\left(C_{\alpha 6}\sin\theta_b - C_{\alpha 9}(1-\cos\theta_b) - C_{\alpha 3}\right)$$

$$\Theta_1 = \frac{F_{axial}R^2}{E_{ss}I_{xx}}\left(C_{\alpha 6}\cos\theta_b - C_{\alpha 9}\sin\theta_b\right) \qquad \textbf{Eq. (A.1)}$$

$$\Psi_1 = \frac{F_{axial}R^2}{E_{ss}I_{xx}}\left(C_{\alpha 9}\cos\theta_b + C_{\alpha 6}\sin\theta_b\right)$$

$$
\begin{aligned}
C_{\alpha 9} &= \frac{1+\beta}{2}\left[(\theta_b - \varphi)\sin(\theta_b - \varphi) - \sin(\theta_b - \varphi)\right] \\
C_{\alpha 6} &= \frac{1+\beta}{2}\left[(\theta_b - \varphi)\sin(\theta_b - \varphi)\right] - \beta(1 - \cos(\theta_b - \varphi)) \\
C_{\alpha 3} &= -\beta\left[\theta_b - \varphi - \sin(\theta_b - \varphi)\right] - \frac{1-\beta}{2}(1 - \cos(\theta_b - \varphi)) \\
\beta &= \frac{E_{ss} I_{xx}}{G_{ss} K}
\end{aligned}
\qquad \textbf{Eq. (A.2)}
$$

In the case of the flexures, the force was applied to the free end of the beam. φ=0 and,

$$
\begin{aligned}
C_{\alpha 9} &= \frac{1+\beta}{2}\left[\theta_b \sin\theta_b - \sin\theta_b\right] \\
C_{\alpha 6} &= \frac{1+\beta}{2}\left[\theta_b \sin\theta_b\right] - \beta(1 - \cos\theta_b) \\
C_{\alpha 3} &= -\beta\left[\theta_b - \sin\theta_b\right] - \frac{1-\beta}{2}(1 - \cos\theta_b) \\
\beta &= \frac{EI}{GK}
\end{aligned}
\qquad \textbf{Eq. (A.3)}
$$

Substituted into Equations A.1 to get,

$$
\begin{aligned}
\delta_1 &= \frac{-F_{axial} R^3}{E_{ss} I_{xx}}\left(\theta_b - \beta\theta_b + 2\beta\sin\theta_b + \beta\sin\theta_b\cos\theta_b - \sin\theta_b\cos\theta_b + 2\beta\theta\sin\theta_b\right) \\
\Theta_1 &= \frac{F_{axial} R^2}{E_{ss} I_{xx}}\left(-2\beta\cos\theta_b + \beta\cos^2\theta_b + 1 - \cos^2\theta_b + \beta\right) \\
\Psi_1 &= \frac{F_{axial} R^2}{E_{ss} I_{xx}}\left(-\cos\theta_b\sin\theta_b + \beta\cos\theta_b\sin\theta_b + \theta_b + \theta_b\beta - 2\beta\sin\theta_b\right)
\end{aligned}
\qquad \textbf{Eq. (A.4)}
$$

Case 2:Concentration Intermediate Bending Moment. One end fixed and one end free.

$$
\begin{aligned}
\delta_2 &= \frac{M_0 R^2}{E_{ss} I_{xx}}\left(C_{\alpha 4}\sin\theta_b - C_{\alpha 7}(1 - \cos\theta_b) - C_{\alpha 1}\right) \\
\Theta_2 &= \frac{M_0 R}{E_{ss} I_{xx}}\left(C_{\alpha 7}\sin\theta_b - C_{\alpha 4}\cos\theta_b\right) \\
\Psi_2 &= \frac{-M_0 R}{E_{ss} I_{xx}}\left(C_{\alpha 4}\sin\theta_b + C_{\alpha 7}\cos\theta_b\right)
\end{aligned}
\qquad \textbf{Eq. (A.5)}
$$

$$
\begin{aligned}
C_{\alpha 4} &= \frac{1+\beta}{2}(\theta_b - \varphi)\cos(\theta_b - \varphi) + \frac{1-\beta}{2}\sin(\theta_b - \varphi) \\
C_{\alpha 7} &= -\frac{1+\beta}{2}(\theta_b - \varphi)\sin(\theta_b - \varphi) \\
C_{\alpha 1} &= \frac{1+\beta}{2}(\theta_b - \varphi)\sin(\theta_b - \varphi) - \beta(1 - \cos(\theta_b - \varphi)) \\
\beta &= \frac{E_{ss} I_{xx}}{G_{ss} K}
\end{aligned}
\qquad \textbf{Eq. (A.6)}
$$

In the case of the flexures, the force was applied to the free end of the beam. φ=0 and,

$$
\begin{aligned}
C_{\alpha 4} &= \frac{1+\beta}{2}\theta_b \cos\theta_b + \frac{1-\beta}{2}\sin\theta_b \\
C_{\alpha 7} &= -\frac{1+\beta}{2}\theta_b \sin\theta_b \\
C_{\alpha 1} &= \frac{1+\beta}{2}\theta_b \sin\theta_b - \beta(1 - \cos\theta_b) \\
\beta &= \frac{E_{ss} I_{xx}}{G_{ss} K}
\end{aligned}
\qquad \textbf{Eq. (A.7)}
$$

Substituted into Equations A.5 to get,

$$
\begin{aligned}
\delta_2 &= \frac{M_0 R^2}{E_{ss} I_{xx}}\left(1 - \cos^2\theta_b + \beta + \beta\cos^2\theta_b + 2\beta\cos\theta_b\right) \\
\Theta_2 &= -\frac{M_0 R}{E_{ss} I_{xx}}(\theta_b + \theta_b\beta + \sin\theta_b\cos\theta_b - \beta\sin\theta_b\cos\theta_b) \\
\Psi_2 &= -\frac{M_0 R}{E_{ss} I_{xx}}\left(1 - \cos^2\theta_b - \beta - \beta\cos^2\theta_b\right)
\end{aligned}
\qquad \textbf{Eq. (A.8)}
$$

Case 3:Concentration Intermediate Twisting Torque. One end fixed and one end free.

$$
\begin{aligned}
\delta_3 &= \frac{T_0 R^2}{E_{ss} I_{xx}}(C_{\alpha 5}\sin\theta_b - C_{\alpha 8}(1 - \cos\theta_b) - C_{\alpha 2}) \\
\Theta_3 &= \frac{-T_0 R}{E_{ss} I_{xx}}(C_{\alpha 5}\cos\theta_b - C_{\alpha 8}\sin\theta_b) \\
\Psi_3 &= \frac{-T_0 R}{E_{ss} I_{xx}}(C_{\alpha 8}\cos\theta_b + C_{\alpha 5}\sin\theta_b)
\end{aligned}
\qquad \textbf{Eq. (A.9)}
$$

$$C_{\alpha 8} = \frac{1-\beta}{2}\sin(\theta_b - \varphi) - \frac{1+\beta}{2}(\theta_b - \varphi)\cos(\theta_b - \varphi)$$
$$C_{\alpha 5} = -\frac{1+\beta}{2}(\theta_b - \varphi)\sin\theta_b(\theta - \varphi)$$
$$C_{\alpha 1} = \frac{1+\beta}{2}[(\theta_b - \varphi)\cos(\theta_b - \varphi) - \sin(\theta_b - \varphi)] \qquad \textbf{Eq. (A.10)}$$
$$\beta = \frac{E_{ss}I_{xx}}{G_{ss}K}$$

In the case of the flexures, the force was applied to the free end of the beam. φ=0 and,

$$C_{\alpha 8} = \frac{1-\beta}{2}\sin\theta_b - \frac{1+\beta}{2}\theta_b\cos\theta_b$$
$$C_{\alpha 5} = -\frac{1+\beta}{2}\theta_b\sin\theta_b$$
$$C_{\alpha 1} = \frac{1+\beta}{2}[\theta_b\cos\theta_b - \sin\theta_b] \qquad \textbf{Eq. (A.11)}$$
$$\beta = \frac{E_{ss}I_{xx}}{G_{ss}K}$$

Substituted into Equations A.5 to get,

$$\delta_3 = -\frac{T_0R^2}{E_{ss}I_{xx}}(\theta_b + \theta_b\beta - \sin\theta_b\cos\theta_b - 2\beta\sin\theta_b + \beta\cos\theta_b\sin\theta_b)$$
$$\Theta_3 = \frac{T_0R}{E_{ss}I_{xx}}\left(1 - \cos^2\theta_b - \beta + \beta\cos^2\theta_b\right) \qquad \textbf{Eq. (A.12)}$$
$$\Psi_3 = \frac{T_0R}{E_{ss}I_{xx}}(-\cos\theta_b\sin\theta_b + \beta\cos\theta_b\sin\theta_b + \theta_b + \beta\theta_b)$$

The Boundary Condition of Θ_{total}=0 was applied to Equations A.4, A.8 and A.12.

$$\Theta_1 = \frac{F_{axial}R^2}{E_{ss}I_{xx}}\left(-2\beta\cos\theta_b + \beta\cos^2\theta_b + 1 - \cos^2\theta_b + \beta\right)$$
$$\Theta_2 = -\frac{M_0R}{E_{ss}I_{xx}}(\theta_b + \theta_b\beta + \sin\theta_b\cos\theta_b - \beta\sin\theta_b\cos\theta_b) \qquad \textbf{Eq. (A.13)}$$
$$\Theta_3 = \frac{T_0R}{E_{ss}I_{xx}}\left(1 - \cos^2\theta_b - \beta + \beta\cos^2\theta_b\right)$$
$$\Theta_{total} = \Theta_1 + \Theta_2 + \Theta_3 = 0$$

M_0 was then isolated in terms of F_{axial} and T_0 to get:

$$M_0 = \frac{F_{axial} R\left[-\cos\theta_b \sin\theta_b + \beta\cos\theta_b \sin\theta_b + \theta_b + \theta_b\beta - 2\beta\sin\theta_b\right] + T_0\left[1 - \cos^2\theta_b - \beta + \beta\cos^2\theta_b\right]}{\theta_b + \theta_b\beta + \cos\theta_b \sin\theta_b + \beta\cos\theta_b \sin\theta_b}$$

Eq. (A.14)

The Boundary Condition of Ψ_{total}=0 was applied to Equations A.4, A.8 and A.12.

$$\Psi_1 = \frac{F_{axial} R^2}{E_{ss} I_{xx}}\left(-\cos\theta_b \sin\theta_b + \beta\cos\theta_b \sin\theta_b + \theta_b + \theta_b\beta - 2\beta\sin\theta_b\right)$$

$$\Psi_2 = -\frac{M_0 R}{E_{ss} I_{xx}}\left(1 - \cos^2\theta_b - \beta - \beta\cos^2\theta_b\right)$$

$$\Psi_3 = \frac{T_0 R}{E_{ss} I_{xx}}\left(-\cos\theta_b \sin\theta_b + \beta\cos\theta_b \sin\theta_b + \theta_b + \beta\theta_b\right)$$

$$\Psi_{total} = \Psi_1 + \Psi_2 + \Psi_3 = 0$$

Eq. (A.15)

Equation A.14 as then substituted into A.15 and T_0 was calculated in terms of F_{axial} to get:

$$T_0 = -\left[F_{axial} R \frac{-1 + \beta^2 + \cos^2\theta_b + {\theta_b}^2 + (\theta_b\beta)^2 + 2{\theta_b}^2\beta + (\beta\cos\theta_b)^2 - 2\beta\theta_b \sin\theta_b - 2\beta^2\theta_b \sin\theta_b}{-1 + (\beta\theta_b)^2 + 2\beta{\theta_b}^2 + (\beta\cos\theta_b)^2 - 2\beta\cos^2\theta_b + \cos^2\theta_b - \beta^2 + {\theta_b}^2 + 2\beta}\right]$$

Eq. (A.16)

This expression was returned to equation A.16 to solve M_0 in terms of F_{axial} to get:

$$M_0 = \frac{-2F_{axial} R\beta\left[\cos\theta_b - 1\right]\left[\theta_b\beta - \beta\sin\theta_b + \theta_b + \sin\theta_b\right]}{-1 + (\theta_b\beta)^2 + 2{\theta_b}^2\beta + (\beta\cos\theta_b)^2 - 2\beta\cos^2\theta_b + \cos^2\theta_b - \beta^2 + {\theta_b}^2 + 2\beta}$$

Eq. (A.17)

The last boundary conditions of δ_{total}=0.031 inch was then applied to Equations A.4, A.8 and A.12.

$$\delta_1 = \frac{-F_{axial}R^3}{E_{ss}I_{xx}}\left(\theta_b - \beta\theta_b + 2\beta\sin\theta_b + \beta\sin\theta_b\cos\theta_b - \sin\theta_b\cos\theta_b + 2\beta\theta_b\sin\theta_b\right)$$

$$\delta_2 = \frac{M_0R^2}{E_{ss}I_{xx}}\left(1 - \cos^2\theta_b + \beta + \beta\cos^2\theta_b + 2\beta\cos\theta_b\right) \qquad \textbf{Eq. (A.18)}$$

$$\delta_3 = -\frac{T_0R^2}{E_{ss}I_{xx}}\left(\theta_b + \theta_b\beta - \sin\theta_b\cos\theta_b - 2\beta\sin\theta_b + \beta\cos\theta_b\sin\theta_b\right)$$

$$\delta_{total} = \delta_1 + \delta_2 + \delta_3 = 0.0031$$

Equations A.16 and A.17 were substituted into Equation A.18 to get the total deflection in terms of F_{axial}.

Equation A.16, A.17 and A.18 defined the restoring moment, restoring torque and deflection in terms of the applied force. It was not possible to isolate F_{axial} in Equation A.18; therefore F_{axial} was approximated and M_0, T_0 and δ_{total} were calculated. Once the appropriate δ_{total} was achieved. At this point, M_0, F_{axial} and T_0 were noted. This point was highlighted on the following spreadsheet.

Reactionary force, reactionary moment, reactionary torque, bending stress and shear stress were calculated according to the rules of superposition. The following applied.

$$V = -F_{axial}$$

$$M_{react} = -F_{axial}R\sin\theta_b - M_0\cos\theta_b - T_0\sin\theta_b$$

$$T_{react} = -F_{axial}R\sin\theta_b - M_0\sin\theta_b + T_0\cos\theta_b \qquad \textbf{Eq. (A.19)}$$

$$\sigma_{bending} = \frac{M_{react}h}{2I_{xx}}$$

$$\tau_{shear} = \frac{T_{react}}{bh^2}\left(3 + 1.8\frac{h}{b}\right)$$

A-II Curved Beam Loaded in the Plane of Curvature

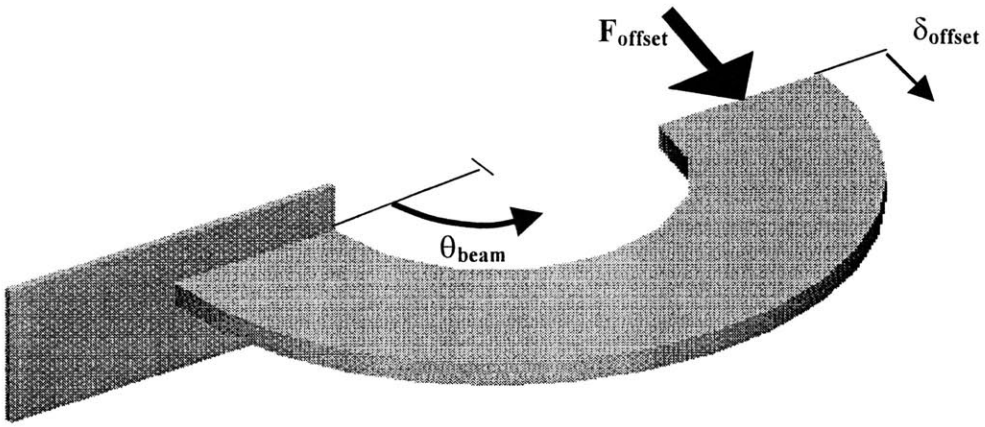

The above figure appeared in Section 3.4- Multi-leaf Flexure Assembly Design. The following development is in relation to this figure. All Equations were derived for Curved Beam Analysis from Roark and Young's *Formulas for Stress and Strain* and Mischke's *Mechanical Engineering Design*. The applied force arises from the magnetic offsetting force in the radial direction when the flexure deflects radially 0.031 inch. The development of the magnetic offsetting force and the stiffness of the flexure appear here.

When the Ferromagnetic Core is offset by 0.003 inches in the air gap geometry varies according to:

$$gap(\theta) = gap_{offset} - gap_{offset}\cos\left(\theta - \frac{\pi}{2}\right) \qquad \textbf{Eq. (A.20)}$$

This is the gap that the offsetting magnetic field sets up in.

Most carbon steels have a saturation point of approximately 1.8 T, so this values was used to determine the saturation current according to Equation A.21.

$$i_{sat}(\theta_c) = \frac{B_{sat,\theta=0}\left(\frac{l_{ckt}}{\mu_{ci}} + gap(\theta_c)\right)}{N\mu_0} \qquad \textbf{Eq. (A.21)}$$

the $l_{ckt}/\mu_{castiron}$ term arose because the entire magnetic was considered in this analysis rather than just the length of the gap. This is the reluctance of the cast iron part of the magnetic circuit.

This expression is then used to determine the offsetting magnetic force according to Equations A.22.

$$F_{offset} = \int_0^{2\pi} \frac{B(\theta_c)^2 A_{circum}}{2\mu_0} \cdot \cos(\theta_c) d\theta_c$$

$$F_{offset} = \int_0^{\pi} B_{sat}^2 \frac{A_{circumference}}{2\mu_0} \sin(\theta_c) d\theta_c + \int_{\pi}^{2\pi} \left[\frac{Ni_{sat}(\pi)\mu_0}{\frac{l_{ckt}}{\mu_{ci}} + gap(\theta_c)}\right]^2 \frac{A_{circum}}{2\mu_0} \sin(\theta_c) d\theta_c$$

Eq. (A.22)

From this integration it was found that for a circumferential area of 4.032e-5 m^2 and a 700-turn coil with the length of the circuit approximated at 5 inches, the offsetting force was found to be approximately 9.3 lbf.

Castigliano's Theorem for strain energy was used to solve for a curved member loaded in the plane of curvature. This method superimposed the strain energies that arose form each of the reactionary forces in the member. The strain energies are as follows:

$$U_{bending} = \int \frac{M^2 d\theta_c}{2A_{cross} ecc E_{ss}}$$

$$U_{F_{\theta 1}} = \int \frac{F_\theta^2 R d\theta_c}{2A_{cross} E_{ss}}$$

$$U_{F_{\theta 2}} = -\int \frac{MF_\theta \, d\theta_c}{A_{cross} E_{ss}} \qquad \textbf{Eq. (A.23)}$$

$$U_{F_r} = \int \frac{C_{rect} F_r^2 R d\theta_c}{2A_{cross} G_{ss}}$$

$$U_{total} = U_{F_r} + U_{F_{\theta 2}} + U_{F_{\theta 1}} + U_{bending}$$

The terms M, F_θ and F_r were the reactionary terms that arose from the applied force. Equation A.24 defined the eccentricity.

$$ecc = R - r_n$$

$$R_b = \frac{h}{\ln\left[\frac{r_o}{r_i}\right]} \qquad \textbf{Eq. (A.24)}$$

Finally the constant C was a strain energy correction factor for shear. For a rectangular beam C was 1.5.

Equation A.25 defined the deflection of the beam, which was 0.003-inch in this case.

$$\delta_{offset} = \frac{\partial U_{total}}{\partial F_{offset}} \qquad \textbf{Eq. (A.25)}$$

Equations A.23 were integrated then differentiated with respect to F_{offset} substituted into this expression. Finally, after rearranging and simplifying, Equation A.26 defined the offsetting force.

$$F_{offset} = \frac{2\delta_{offset} E_{ss} A_{cross}}{R_b}\left[\left(\frac{R_b}{ecc} - 1\right)\left(\theta_c - \cos\theta_c \sin\theta_c\right) + \frac{C_{rect} E_{ss}}{G_{ss}}\left(\theta_c + \cos\theta_c \sin\theta_c\right)\right]^{-1}$$

Eq. (A.26)

Equation A.26 was then used in the spreadsheet that appears in the following pages. The lateral rigidity or lateral stiffness was defined as the resulting force that occurred when the beam was offset by 0.003-inch. This force was compared to the magnetic offsetting force of 9.3 lbf. Each flexure was to withstand a minimum of one-third of this force. The force was calculated for various combinations of flexure beam spans and flexure thickness. It was chosen to have a beam span of 300° and a thickness of 0.010-inch. The results of this analysis appear in the included printout.

Flexure Angle	Flexure Angle	Lateral Rigidity h=5mil	Lateral Rigidity h=8mil	Lateral Rigidity h=10mil	Lateral Rigidity h=12mil	Lateral Rigidity h=13mil	Lateral Rigidity h=14mil	Lateral Rigidity h=15mil
Span of Beam	Span of Beam	0.005	0.008	0.01	0.012	0.013	0.014	0.015
degrees	radians	lbf	lbf	lbf	lbf	lbf	lbf	lbf
ba=	0.1							
360	6.28	0.70	1.13	1.41	1.69	1.83	1.97	2.11
330	5.76	0.72	1.16	1.45	1.74	1.88	2.02	2.17
300	5.24	0.79	1.27	1.58	1.90	2.06	2.21	2.37
270	4.71	0.94	1.50	1.88	2.25	2.44	2.63	2.81
240	4.19	1.15	1.84	2.30	2.76	3.00	3.23	3.46
210	3.67	1.33	2.13	2.67	3.20	3.47	3.74	4.00
180	3.14	1.41	2.25	2.81	3.38	3.66	3.94	4.22
bb=	0.15							
360	6.28	1.06	1.69	2.11	2.53	2.74	2.95	3.17
330	5.76	1.08	1.74	2.17	2.60	2.82	3.04	3.25
300	5.24	1.19	1.90	2.37	2.85	3.08	3.32	3.56
270	4.71	1.41	2.25	2.81	3.38	3.66	3.94	4.22
240	4.19	1.73	2.76	3.46	4.15	4.49	4.84	5.18
210	3.67	2.00	3.20	4.00	4.80	5.20	5.60	6.00
180	3.14	2.11	3.38	4.22	5.06	5.49	5.91	6.33
bc=	0.20							
360	6.28	1.41	2.25	2.81	3.38	3.66	3.94	4.22
330	5.76	1.45	2.31	2.89	3.47	3.76	4.05	4.34
300	5.24	1.58	2.53	3.16	3.80	4.11	4.43	4.75
270	4.71	1.88	3.00	3.75	4.50	4.88	5.25	5.63
240	4.19	2.30	3.69	4.61	5.53	5.99	6.45	6.91
210	3.67	2.67	4.27	5.34	6.40	6.94	7.47	8.00
180	3.14	2.81	4.50	5.63	6.75	7.32	7.88	8.44
bd=	0.25							
360	6.28	1.76	2.81	3.52	4.22	4.57	4.92	5.28
330	5.76	1.81	2.89	3.62	4.34	4.70	5.06	5.42
300	5.24	1.98	3.16	**3.95**	4.75	5.14	5.54	5.93
270	4.71	2.34	3.75	4.69	5.63	6.10	6.57	7.03
240	4.19	2.88	4.61	5.76	6.91	7.49	8.06	8.64
210	3.67	3.34	5.34	6.67	8.00	8.67	9.34	10.01
180	3.14	3.52	5.63	7.03	8.44	9.14	9.85	10.55
be=	0.3							
360	6.28	2.11	3.38	4.22	5.06	5.49	5.91	6.33
330	5.76	2.17	3.47	4.34	5.21	5.64	6.07	6.51
300	5.24	2.37	3.80	4.75	5.69	6.17	6.64	7.12
270	4.71	2.81	4.50	5.63	6.75	7.32	7.88	8.44
240	4.19	3.46	5.53	6.91	8.29	8.99	9.68	10.37
210	3.67	4.00	6.40	8.00	9.61	10.41	11.21	12.01

180	3.14	4.22	6.75	8.44	10.13	10.97	11.82	12.66
bf=	**0.35**							
360	6.28	2.46	3.94	4.92	5.91	6.40	6.89	7.39
330	5.76	2.53	4.05	5.06	6.07	6.58	7.09	7.59
300	5.24	2.77	4.43	5.54	6.64	7.20	7.75	8.30
270	4.71	3.28	5.25	6.57	7.88	8.54	9.19	9.85
240	4.19	4.03	6.45	8.06	9.68	10.48	11.29	12.10
210	3.67	4.67	7.47	9.34	11.21	12.14	13.07	14.01
180	3.14	4.92	7.88	9.85	11.82	12.80	13.79	14.77

$F_{applied}$=	0.034	lb			
$T_{applied}$=	0.01581	lb-in			
$M_{applied}$=	2.17E-06	lb-in			
Angle on Beam	**Transverse Shear**	**Transverse Moment**	**Transverse Torque**	**Bending Stress**	**Torsional Stress (Shear)**
radians	**lbs**	**lb-in**	**lb-in**	**Psi**	**Psi**
0.0000	-0.0340	0.0000	0.0158	0.5208	1942.7328
0.0942	-0.0340	-0.0030	0.0157	-713.6507	1925.5141
0.1885	-0.0340	-0.0059	0.0153	-1421.4877	1873.9605
0.2827	-0.0340	-0.0088	0.0146	-2116.7076	1788.5297
0.3770	-0.0340	-0.0116	0.0136	-2793.1394	1669.9799
0.4712	-0.0340	-0.0144	0.0124	-3444.7791	1519.3635
0.5655	-0.0340	-0.0169	0.0109	-4065.8427	1338.0172
0.6597	-0.0340	-0.0194	0.0092	-4650.8175	1127.5508
0.7540	-0.0340	-0.0216	0.0072	-5194.5114	889.8323
0.8482	-0.0340	-0.0237	0.0051	-5692.0985	626.9717
0.9425	-0.0340	-0.0256	0.0028	-6139.1620	341.3023
1.0367	-0.0340	-0.0272	0.0003	-6531.7340	35.3596
1.1310	-0.0340	-0.0286	-0.0023	-6866.3298	-288.1407
1.2252	-0.0340	-0.0297	-0.0051	-7139.9796	-626.3274
1.3195	-0.0340	-0.0306	-0.0079	-7350.2544	-976.1985
1.4137	-0.0340	-0.0312	-0.0109	-7495.2878	-1334.6487
1.5080	-0.0340	-0.0316	-0.0138	-7573.7925	-1698.4963
1.6022	-0.0340	-0.0316	-0.0168	-7585.0717	-2064.5117
1.6965	-0.0340	-0.0314	-0.0198	-7529.0253	-2429.4462
1.7907	-0.0340	-0.0309	-0.0227	-7406.1507	-2790.0606
1.8850	-0.0340	-0.0301	-0.0256	-7217.5386	-3143.1541
1.9792	-0.0340	-0.0290	-0.0284	-6964.8631	-3485.5925
2.0735	-0.0340	-0.0277	-0.0310	-6650.3670	-3814.3365
2.1677	-0.0340	-0.0262	-0.0336	-6276.8418	-4126.4679
2.2619	-0.0340	-0.0244	-0.0360	-5847.6029	-4419.2163
2.3562	-0.0340	-0.0224	-0.0382	-5366.4602	-4689.9833
2.4504	-0.0340	-0.0202	-0.0402	-4837.6845	-4936.3655
2.5447	-0.0340	-0.0178	-0.0420	-4265.9691	-5156.1760
2.6389	-0.0340	-0.0152	-0.0435	-3656.3887	-5347.4638
2.7332	-0.0340	-0.0126	-0.0448	-3014.3539	-5508.5309
2.8274	-0.0340	-0.0098	-0.0459	-2345.5635	-5637.9478
2.9217	-0.0340	-0.0069	-0.0467	-1655.9537	-5734.5656
3.0159	-0.0340	-0.0040	-0.0472	-951.6455	-5797.5269
3.1102	-0.0340	-0.0010	-0.0474	-238.8905	-5826.2728
3.2044	-0.0340	0.0020	-0.0474	475.9849	-5820.5481
3.2987	-0.0340	0.0049	-0.0470	1186.6355	-5780.4036
3.3929	-0.0340	0.0079	-0.0464	1886.7534	-5706.1957
3.4872	-0.0340	0.0107	-0.0456	2570.1243	-5598.5830
3.5814	-0.0340	0.0135	-0.0444	3230.6827	-5458.5207

3.6757	-0.0340	0.0161	-0.0430	3862.5652	-5287.2521
3.7699	-0.0340	0.0186	-0.0414	4460.1634	-5086.2972
3.8642	-0.0340	0.0209	-0.0395	5018.1728	-4857.4399
3.9584	-0.0340	0.0230	-0.0375	5531.6406	-4602.7114
4.0527	-0.0340	0.0250	-0.0352	5996.0092	-4324.3728
4.1469	-0.0340	0.0267	-0.0328	6407.1567	-4024.8945
4.2412	-0.0340	0.0282	-0.0302	6761.4339	-3706.9349
4.3354	-0.0340	0.0294	-0.0275	7055.6961	-3373.3160
4.4296	-0.0340	0.0304	-0.0246	7287.3314	-3026.9992
4.5239	-0.0340	0.0311	-0.0217	7454.2839	-2671.0584
4.6181	-0.0340	0.0315	-0.0188	7555.0716	-2308.6529
4.7124	-0.0340	0.0316	-0.0158	7588.8000	-1942.9994
			σ_{max}=	7588.8000	1942.7328
			σ_{min}=	-7585.0717	-5826.2728

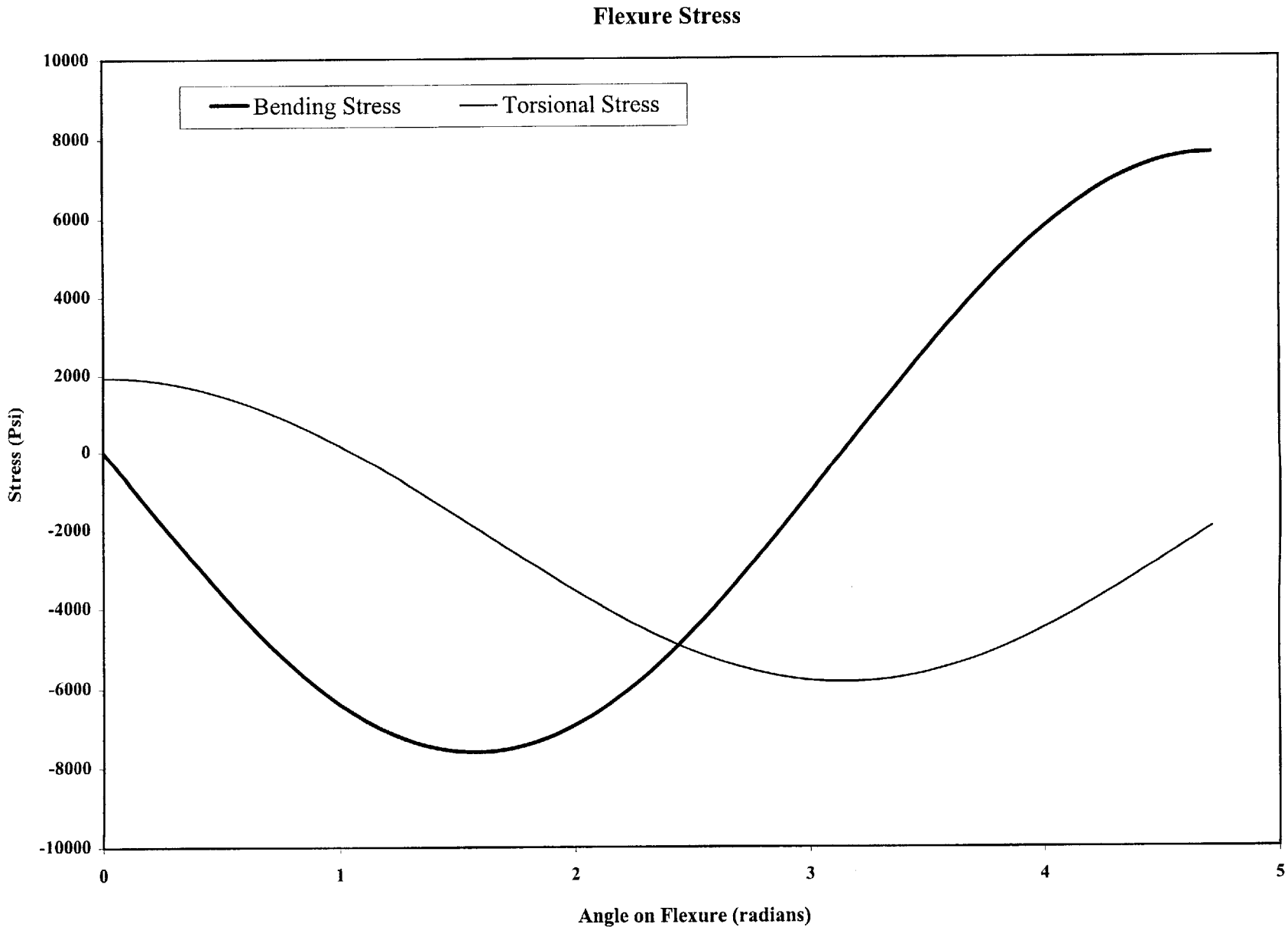
Flexure Stress
Bending Stress
Torsional Stress
10000
8000
6000
4000
2000
0
-2000
-4000
-6000
-8000
-10000
Stress (Psi)
0
1
2
3
4
5
Angle on Flexure (radians)

APPENDIX B- Thermodynamic Analysis

B-I Unmodified G-M Cycle Analysis

The original G-M cycle consisted of 4 states and 4 discreet processes.

State 1: Warm Volume, Regenerator and Cold Volume all at Low Pressure
Warm Volume at maximum volume, Cold Volume at zero

Process 1-2: Close valve V2, open valve V1, charge Warm Volume, Regenerator and Cold Volume to High Pressure

State 2: Warm Volume, Regenerator and Cold Volume at High Pressure
Warm Volume at maximum volume, Cold Volume at zero

Process 2-3 Move displacer from TDC to BDC; Warm Volume goes from maximum to zero and Cold volume goes from zero to maximum

State 3 Warm Volume, Regenerator and Cold Volume at Low Pressure
Warm Volume at zero and Cold Volume at maximum

Process 3-4 Close valve V1, open valveV2 to blow down to Warm Volume, Regenerator and Cold Volume to Low Pressure

State 4 Warm Volume, Regenerator and Cold Volume at Low Pressure
Warm Volume at zero and Cold Volume at maximum

Process 4-1 Move displacer from BDC to TDC; Warm Volume goes from zero to maximum and Cold Volume goes from maximum to zero

System Pressures:

$Ph := 275 \cdot psi$ $Pl := 75\ psi$

Temperatures from G-M Standard Cycle, defined by manufacturer. Tref was the refrigeration temperature, Tinf was ambient and Twin was the temperature entering the warm end throught valve V1.

$Tref := 77 \cdot K$ $Tinf := 298 \cdot K$ $Twin := Tinf$

Constants for Cycle defined by manufacturer and equipment specifications. Vr wa: the regenerator Volume and Vc was the Cold VolumeΔ T was the temperature difference between the upflow and downflow at the warm end of the regenerator.

$$Vr := 0.75 \cdot 4.5 \cdot in \cdot \left[\frac{\pi \cdot (2 \cdot in)^2}{4} \right]$$

$$Vc := \frac{5}{8} \cdot in \cdot \frac{\pi \cdot (3 \cdot in)^2}{4}$$

$$freq := 2.4 \cdot \left(\frac{1}{sec} \right)$$

$$i := 1, 2 .. 100$$

$$\Delta T_i := \frac{i}{10} \cdot K$$

$$Cpo := 5192.6 \cdot \frac{J}{kg \cdot K}$$

$$Cvo := 3115.6 \cdot \frac{J}{kg \cdot K}$$

$$R := 2077.03 \cdot \frac{J}{kg \cdot K}$$

$$\gamma := \frac{Cpo}{Cvo}$$

Applying energy conservation where the change in enthalpy plus the heat generated for the cycle must equal the work put into the cycle.
Overall System Energy Balance:

$$\int \dot{} \; hdm + Q = Work$$

$$Cpo \cdot \left[\frac{Ph \cdot Vc}{R \cdot (Tref + \Delta T)} + \frac{(Ph - Pl) \cdot Vr}{R \cdot \left(\frac{1}{Twin - Tref} \cdot \ln\left(\frac{Twin}{Tref} \right) \right)^{-1}} \right] \cdot \Delta T + Q = (Ph - Pl) \cdot Vc$$

$$Q_i := (Ph - Pl) \cdot Vc - Cpo \cdot \left[\frac{Ph \cdot Vc}{R \cdot (Tref + \Delta T_i)} + \frac{(Ph - Pl) \cdot Vr}{R \cdot \left(\frac{1}{Twin - Tref} \cdot \ln\left(\frac{Twin}{Tref} \right) \right)^{-1}} \right] \cdot \Delta T_i$$

$$Qdot_i := Q_i \cdot freq$$

Since the capacity of the cycle was known to be 150 W, the operating point of the cycle occured when Qdot was 150 Watts. This was matched to a T and a Q.

$Q_i =$

99.018
98.208
97.398
96.59
95.782
94.976
94.171
93.367
92.565
91.763
90.962
90.163
89.365
88.567
87.771
86.976

J

Qdot =

	0
0	0
1	237.644
2	235.699
3	233.756
4	231.815
5	229.878
6	227.943
7	226.011
8	224.082
9	222.155
10	220.231
11	218.31
12	216.391
13	214.475
14	212.562
15	210.651

W

$\Delta T =$

	0
0	0
1	0.1
2	0.2
3	0.3
4	0.4
5	0.5
6	0.6
7	0.7
8	0.8
9	0.9
10	1
11	1.1
12	1.2
13	1.3
14	1.4
15	1.5

K

$Q_{47} = 62.85$ J $Qdot_{47} = 150.839$ W $\Delta T_{47} = 4.7$ K

$\Delta Thigh := 4.7$ K

Next a mass balance in the regenerator was defined for the low pressure and high pressure states. An Average temperature in the regenerator was also established.

$$Tregav := \left(\frac{1}{Twin - Tref}\cdot\ln\left(\frac{Twin}{Tref}\right)\right)^{-1}$$

$Tregav = 163.306$ K

$$mcharge := \frac{Ph\cdot Vr}{R\cdot Tregav}$$

$mcharge = 9.713\cdot10^{-4}$ kg

$$mreg := \frac{Pl\cdot Vr}{R\cdot Tregav}$$

$mreg = 2.649\cdot10^{-4}$ kg

The regenerator was defined as a balanced heat exchanger. It had an ineffectiveness throughout the span, but the enthalpy flow through top equals that of through the bottom. This was used to define the temperature difference between the upflow and the downflow at the cold end.

$Cpo(dmtop \cdot T) = Cpo(dmbot \cdot T)$

$$\frac{Ph \cdot Vc}{(Tref + \Delta Tlow) \cdot R} \cdot \Delta Tlow = \left[mcharge + \frac{Ph \cdot Vc}{R \cdot (Tref + \Delta Tlow)} - mreg \right] \cdot \Delta Thigh$$

$$\Delta Tlow := \Delta Thigh \frac{(mcharge R \cdot Tref + Vc \cdot Ph - mreg R \cdot Tref)}{(Vc \cdot Ph - \Delta Thigh mcharge R + \Delta Thigh mreg R)}$$

$\Delta Tlow = 9.021\ K$

The mass flow through warm end of the regenerator wa defined for each process. These flow rates were to be applied to the enthalpy flow in and out of the regenerator and ultimately to the energy balance of the system.

$$dmwin12 := \frac{(Ph - Pl) \cdot Vr}{R \cdot Tregav} \qquad dmwin12 = 7.064 \cdot 10^{-4}\ kg$$

$$dmwin23 := \frac{Ph \cdot Vc}{R \cdot (Tref + \Delta Tlow)} \qquad dmwin23 = 7.683 \cdot 10^{-4}\ kg$$

$$dmwout34 := \frac{(Ph - Pl) \cdot Vr}{R \cdot Tregav} + \frac{Ph \cdot Vc}{R} \cdot \left(\frac{1}{Tref + \Delta Tlow} - \frac{1}{Tref} \right) \qquad dmwout34 = 6.164 \cdot 10^{-4}\ kg$$

$$dmwout41 := \frac{Ph \cdot Vc}{R \cdot Tref} \qquad dmwout41 = 8.583 \cdot 10^{-4}\ kg$$

$dmout := dmwout41 + dmwout34 \qquad dmout = 1.475 \cdot 10^{-3}\ kg$

$dmin := dmwin12 + dmwin23 \qquad dmin = 1.475 \cdot 10^{-3}\ kg$

Finally, to recheck the math, the energy in (Work) was compared with the total energy change in the system for the process

$Workin := Vc \cdot (Ph - Pl)$ $Workin = 99.83\ J$

$Energy2 := Cpo \cdot \Delta Thighdmin + Q_{47}$ $Energy2 = 98.839\ J$

Slight difference occurs due to the approximations in ΔT and Q

B-II Modified G-M Cycle Analysis

The modified G-M cycle consisted of 5 states and 5 discreet processes.

State 1: Warm Volume, Regenerator and Cold Volume all at Low Pressure
Surge Volume at Low Pressure, valves V3 and V4 off.
Warm Volume at maximum volume, Cold Volume at zero

Process 1-2: Close valve V2, open valve V1, charge Warm Volume, Regenerator and Cold Volume to High Pressure.

State 2: Warm Volume, Regenerator and Cold Volume at High Pressure
Surge Volume at Low Pressure, valves V3 and V4 off.
Warm Volume at maximum volume, Cold Volume at zero

Process 2-3 Move displacer from TDC to BDC; Warm Volume goes from maximum to zero and Cold volume goes from zero to maximum

State 3 Warm Volume, Regenerator and Cold Volume at Low Pressure
Surge Volume at Low Pressure, valves V3 and V4 off.
Warm Volume at zero and Cold Volume at maximum

Process 3-4 Close valve V1, open valve V2 to blow down to Warm Volume, Regenerator and Cold Volume to Intermediate Pressure

State 4 Warm Volume, Regenerator and Cold Volume at Intermediate Pressure
Surge Volume at Low Pressure, valves V3 and V4 off.
Warm Volume at zero and Cold Volume at maximum

Process 4-5 With V2 closed, open V3 to equalize Warm Volume, Regenerator and Cold Volume with Surge Volume at Low Pressure

State 5 Warm Volume, Regenerator, Cold Volume and Surge Volume at pressure differentially larger than Low Pressure
Warm Volume at zero and Cold Volume at maximum

Process 5-1 Close V3, open V4 and V2 to equalize Warm Volume, Regenerator, Cold Volume and Surge Volume to Low Pressure
Move the displacer from BDC to TDC,Warm Volume goes from zero to maximum and Cold volume goes from maximum to zero

System Pressures:

$Ph := 275 \cdot psi$ $Pl := 75\ psi$ $Px := 275\ psi$

As a starting point, the temperatures from were initially defined by the temperature from the previous analysis of a G-M Standard Cycle. Later Δ Thigh was varied to match the refrigeration capacity.

$Tref := 77 \cdot K$ $Tinf := 298 \cdot K$ $Tnom := 76.18 \cdot K$

$\Delta Tlow := \frac{9.021}{2} \cdot K$ $\Delta Thigh := 4.75 \cdot K$

$Twin := Tinf$ $Twout := Twin - \Delta Thigh$

$Tcout := Tnom + \Delta Tlow$ $Tcin := Tnom - \Delta Tlow$

$$Tregav := \left(\frac{1}{Twin - Tcout} \cdot \ln\left(\frac{Twin}{Tcout} \right) \right)^{-1}$$

Constants for Cycle defined by manufacturer. Same constants as defined in the GM Standard Analysis.

$$Vr := 0.75 \cdot 4.5 \cdot in \cdot \left[\frac{\pi \cdot (2 \cdot in)^2}{4} \right]$$

$$Vc := \frac{5}{8} \cdot in \cdot \frac{\pi \cdot (3 \cdot in)^2}{4}$$

$$freq := 2.4 \cdot \left(\frac{1}{sec} \right)$$

$i := 1, 2 .. 100$

$$\Delta T_i := \frac{i}{10} \cdot K$$

$$Cpo := 5192.6 \cdot \frac{J}{kg \cdot K}$$

$$Cvo := 3115.6 \cdot \frac{J}{kg \cdot K}$$

$$R := 2077.03 \cdot \frac{J}{kg \cdot K}$$

$$\gamma := \frac{Cpo}{Cvo}$$

The masses and mass flows about the ends of the regenerator were defined for each process systematically. mreg and dmreg refer to the regenerator mass and mass flow. mw and dmw refer to the warm end mass and flow and mc and dmc refer to the cold end mass and flow.

Process 1-2: Charge with High Pressure Helium

$$mreg1 := \frac{Pl \cdot Vr}{R \cdot Tregav} \qquad mreg1 = 2.601 \cdot 10^{-4}\ kg$$

$$mreg2 := \frac{Ph \cdot Vr}{R \cdot Tregav} \qquad mreg2 = 9.536 \cdot 10^{-4}\ kg$$

$$dmwin12 := (mreg2 - mreg1) \qquad dmwin12 = 6.935 \cdot 10^{-4}\ kg$$

Process 2-3: Move Displacer

$$mc3 := \frac{Ph \cdot Vc}{R \cdot Tcout} \qquad mc3 = 8.19 \cdot 10^{-4}\ kg$$

$$mreg3 := mreg2 \qquad mreg3 = 9.536 \cdot 10^{-4}\ kg$$

Process 3-4: Discharge into Compressor to Px

$$Tc4 := Tcout \cdot \left(\frac{Px}{Ph}\right)^{\frac{\gamma - 1}{\gamma}} \qquad Tc4 = 80.691\ K$$

$$mc4 := \frac{Vc \cdot Px}{R \cdot Tc4} \qquad mc4 = 8.19 \cdot 10^{-4}\ kg$$

$$dmR34 := (mc3 - mc4) \qquad dmR34 = 0\ kg$$

$$mreg4 := \frac{Px \cdot Vr}{R \cdot Tregav} \qquad mreg4 = 9.536 \cdot 10^{-4}\ kg$$

Process 3a-4: Equalize into the infinite Surge Volume (Integration)

$a := Vr \cdot \frac{1}{m^3}$ $\quad b := Vc \cdot \frac{1}{m^3}$

$f(t, Y) := \left[\left(1 - \frac{1}{\gamma} \right) - \frac{(Tcout - Y)}{Tregav} \cdot \frac{a}{b} \right] \cdot \frac{Y}{t}$

$x := Tc4 \cdot \frac{1}{K}$ $\quad z := Px \cdot \frac{1}{Pa}$

$Y0 := x$ $\quad ic_0 := Y0$ $\quad t0 := z$ $\quad t1 := 5.171 \cdot 10^5$ $\quad N := 100$

$D(t, Y) := f(t, Y_0)$ $\quad S := rkfixed(ic, t0, t1, N, D)$

$P := S^{<0>}$ $\quad T := S^{<1>}$

$T_1 = 80.456$ $\quad T_{100} = 60.693$

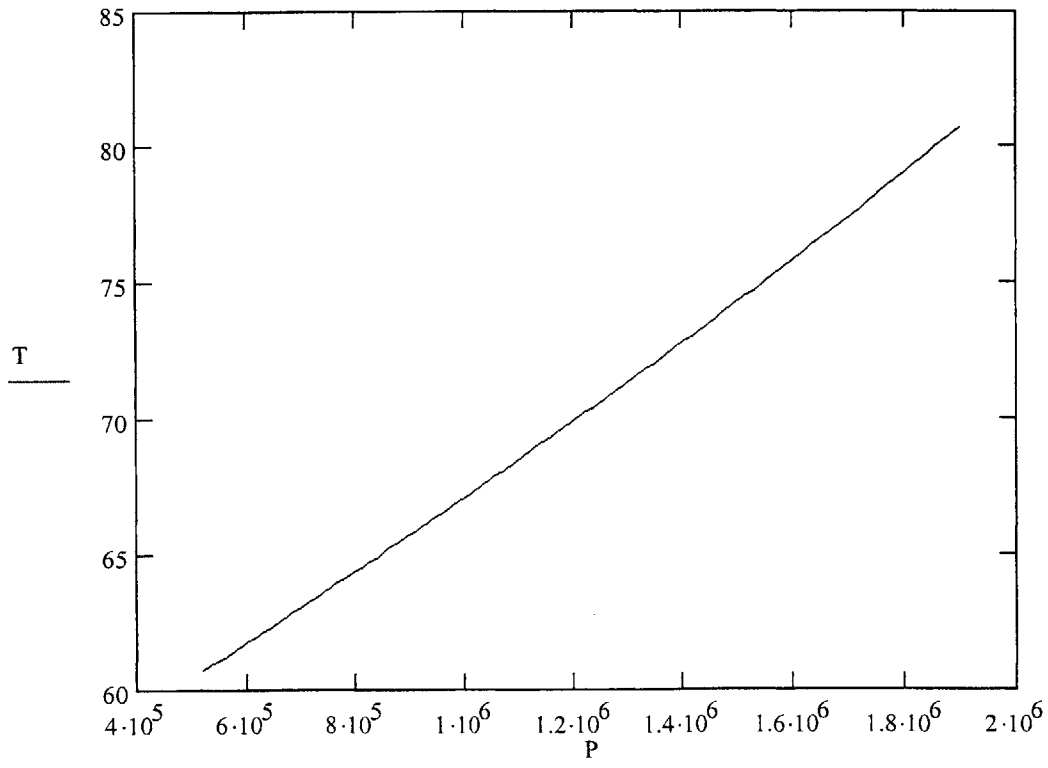

$Tc5 := T_{100} \cdot K$

$$mc5 := \frac{Pl \cdot Vc}{R \cdot Tc5} \qquad mc5 = 2.97 \cdot 10^{-4}\ kg$$

$$mreg5 := \frac{Pl \cdot Vr}{R \cdot Tregav} \qquad mreg5 = 2.601 \cdot 10^{-4}\ kg$$

$$dmR45 := \frac{(Px - Pl) \cdot Vr}{R \cdot Tregav} \qquad dmR45 = 6.935 \cdot 10^{-4}\ kg$$

$dms := -mc5 + mc4 + dmR45$ $\qquad dms = 1.216 \cdot 10^{-3}\ kg$

Using the mass flows in and out of each of the components it was now possible to perform a enthalpy flow balance on the regenerator. Equations for the enthalpy flow into and out of the warm and cold ends were formulated. From this balance the only unknown was the refrigeration temperature. The Thigh was then varied until the refrigeration load equaled 150 W. This was repeated for various values of Px.

$$hdmo := \frac{Cpo \cdot Vc}{R} \cdot \left(\frac{-1}{\gamma} - \frac{Tcin}{Tregav} \cdot \frac{Vr}{Vc} \right) \cdot (Px - Pl) \qquad hdmo = -407.839\ J$$

$hdmw := Cpo \cdot \Delta Thigh(dmwin12 + mc3)$ $\qquad hdmw = 37.307\ J$

$$hdmci := Cpo \cdot \left[\frac{Vc \cdot (Ph - Px)}{R \cdot \gamma} + Tcin \cdot ((mc3 - dmR34) + dmR45) \right] \qquad hdmci = 562.893\ J$$

$hdmco := Cpo \cdot (mc3 \cdot Tcout + dmR45 \cdot Tcout)$ $\qquad hdmco = 633.745\ J$

$hdmc := hdmco - hdmci$ $\qquad hdmc = 70.851\ J$

$$hdmw := \left[-Cpo \cdot \left[\frac{Vc \cdot (Ph - Px)}{R \cdot \gamma} + Tc4 \cdot mc5 \right] + Cpo \cdot (mc3 \cdot Tcout + dmR45 \cdot Tcout) \right] - hmdr$$

$$hdmr := \left[-hdmw + \frac{Cpo}{R} \cdot \left(\frac{Vc \cdot Px}{\gamma} - \frac{Ph \cdot Vc}{\gamma} - Tc5 \cdot mc5 \cdot R + Tcout \cdot R \cdot mc3 + Tcout \cdot R \cdot dmR45 \right) \right]$$

$$hdmo1 := \frac{Cpo}{R} \cdot \left[\sum_{i=1}^{100} \left[-\left(\frac{Vr}{Tregav} \cdot T_i \cdot K + Vc \right) \cdot \left(P_i - P_{i-1} \right) \cdot Pa + \frac{Vc \cdot P_i \cdot Pa}{T_i \cdot K} \cdot \left(T_i - T_{i-1} \right) \cdot K \right] \right]$$

$$Tref := \frac{hdmr}{Cpo \cdot dms} \qquad Tref = 79.665\ K$$

$$Qref := hdmr - hdmo1 \qquad Qref = 62.613\ J$$

$$Qrefdot := Qref \cdot freq \qquad Qrefdot = 150.27\ W$$

Intermediate Pressure vs. Refligeration Temperature

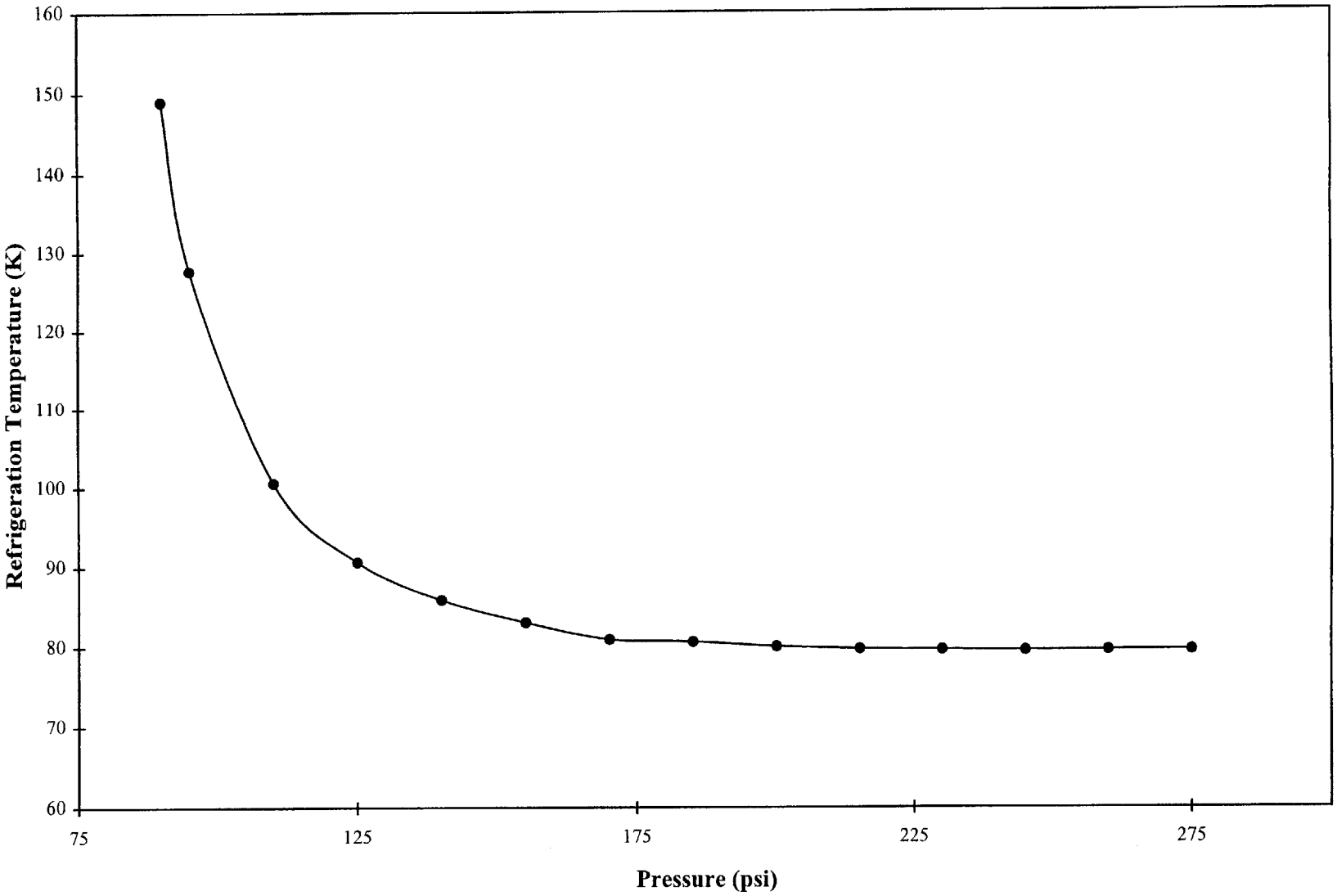

APPENDIX C- Fluid Dynamic Analysis

C-I Blow Down Analysis

The flow through the valve resembles the flow through a converging-diverging nozzle. The critical pressure ration for an ideal gas was defined by the following relationship.

$$\frac{P_{low}}{P_{critical}} = \left[\frac{2}{\gamma+1}\right]^{\frac{\gamma}{\gamma-1}} \qquad \textbf{Eq. (C.1)}$$

For Helium, this ratio was 0.487. This pressure ratio defined the pressure at which the flow regime changed from choked to unchoked. When the ratio of the backpressure (P_L) to the internal pressure in the cold volume was less than this value, the flow was choked. Otherwise, the flow is unchoked.

The entire process was adiabatic and isentropic. The following relations define the states of an isentropic process.

$$\frac{T_{CV}}{T_i} = \left(\frac{P_{CV}}{P_i}\right)^{\frac{\gamma-1}{\gamma}} = \left(\frac{v_{CV}}{v_i}\right)^{\gamma-1}$$
$$\frac{P_{CV}}{P_i} = \left(\frac{v_{CV}}{v_i}\right)^{\gamma} \qquad \textbf{Eq. (C.2)}$$

Here, the subscript i refers to the initial states at t=0. Therefore,

$$P_i = P_H$$
$$T_i = T_0 \qquad \textbf{Eq. (C.3)}$$
$$v_i = v_{P=P_H}$$

C-II Mass Flow Rate for Choked Flow

According to that one Fluid Dynamics Book by that One Guy[7], the maximum mass flow rate defined by the throat cross sectional area was defined by the following.

$$\dot{m}_{choked} = \frac{P_{CV}}{\sqrt{T}} A_{curtain}\left[\left(\frac{\gamma}{R_{He}}\right)^{1/2}\left(\frac{\gamma+1}{2}\right)^{\frac{-(\gamma+1)}{2(\gamma-1)}}\right]$$

Let **Eq. (C.4)**

$$K_M = \left[\left(\frac{\gamma}{R_{He}}\right)^{1/2}\left(\frac{\gamma+1}{2}\right)^{\frac{-(\gamma+1)}{2(\gamma-1)}}\right]$$

The adiabatic relations and K were then substituted into this mass flow rate to get:

$$\dot{m}_{choked} = \frac{K_M A_{curtian}}{\sqrt{T_0}} P_H^{\frac{\gamma-1}{2\gamma}} P_{CV}^{\frac{\gamma+1}{2\gamma}} \qquad \textbf{Eq. (C.5)}$$

C-III Mass Flow Rate for Unchoked Flow

From the first law of thermodynamics, we know

$$\frac{Vel^2}{2} = h_{CV} - h_t = C_{po}\left(T_{CV} - T_t\right) \qquad \textbf{Eq. (C.6)}$$

In this case, the subscript t refers to the time when the flow switched from the choked regime to the unchoked regime.

By definition,

$$\begin{aligned} \dot{m}_{unchoked} &= \rho_t A_t Vel \\ Vel &= \left[2C_{po} T_t \left(\frac{T_{CV}}{T_t} - 1 \right) \right]^{1/2} \\ \rho_t &= \frac{P_t}{RT_t} \end{aligned} \qquad \textbf{Eq. (C.7)}$$

The adiabatic relations were substituted into the mass flow rate expression to eliminate T_t and T. The following expression was achieved after simplification.

$$\dot{m}_{unchoked} = \frac{A_{curtain}}{R_{He}} \left(\frac{2C_{po}}{T_0} \right)^{1/2} \left(\frac{P_L^{\frac{\gamma+1}{2\gamma}}}{P_H^{\frac{1-\gamma}{2\gamma}}} \right) \left[\left(\frac{P_{CV}}{P_L} \right)^{\frac{\gamma-1}{\gamma}} - 1 \right]^{1/2} \qquad \textbf{Eq. (C.8)}$$

C-IV Mass Flow Rate in the Cold Volume

Looking at the mass in the cold volume, the ideal gas laws stated that

$$m_{CV} = \frac{P_{CV} \forall_{CV}}{R_{He} T_{CV}} \qquad \textbf{Eq. (C.9)}$$

Using adiabatic relations to eliminate the temperature from this relationship resulted in the following:

$$m_{CV} = \left(\frac{\forall_{CV}}{R_{He}} \right) \left(\frac{P_H}{T_{CV}} \right) \left(\frac{P_{CV}}{P_H} \right)^{1/\gamma} \qquad \textbf{Eq. (C.10)}$$

This expression was then differentiated to find the mass flow rate in the cylinder as a function of the pressure in the cylinder.

$$\dot{m}_{CV} = \frac{dm_{CV}}{dt} = \left(\frac{\forall_{CV}}{R_{He}}\right)\left(\frac{P_H}{T_0}\right)\frac{d}{dt}\left(\frac{P_{CV}}{P_H}\right)^{1/\gamma}$$

Eq. (C.11)

$$\dot{m}_{CV} = \left(\frac{\forall_{CV}}{R_{He}}\right)\left(\frac{P_H}{T_0}\right)\frac{1}{\gamma}\left(\frac{P_{CV}^{\frac{1-\gamma}{\gamma}}}{P_H^{1/\gamma}}\right)\frac{dP_{CV}}{dt}$$

C-V Dynamic Pressure in the Cold Volume

According to mass conservation, the mass exiting the cylinder must equate to the mass flowing through the orifice. This was expressed as follows:

$$\dot{m}_{CV}\begin{cases} = -\dot{m}_{choked} & for\ P_{CV} \geq P_{crit} \\ = -\dot{m}_{unchoked} & for\ P_{CV} < P_{crit} \end{cases}$$

Eq. (C.12)

These two equalities then defined two differential pressures for the process in each regime.

For choked flow:

$$dP_{choked} = \frac{-\gamma K_M R_{He} A_{curtain}}{\forall_{CV}}\sqrt{T_0}\left[\frac{P_H^{\frac{1-\gamma}{2\gamma}}}{P_{CV}^{\frac{1+\gamma}{2\gamma}}}\right]dt$$

Eq. (C.13)

For unchoked flow:

$$dP_{unchoked} = \frac{-\gamma A_{curtain}}{\forall_{CV}}\sqrt{5R_{He}T_0}\left[\left(\frac{P_H}{P_{CV}}\right)^{\frac{1-\gamma}{\gamma}} P_L^{\frac{1+\gamma}{\gamma}}\left(\left(\frac{P_{CV}}{P_L}\right)^{\frac{\gamma-1}{\gamma}} - 1\right)\right]^{1/2} dt$$

Eq. (C.14)

These two relations were then used to calculate the change in pressure in the cold volume for each time step. The pressure in the cylinder was differentially calculated according to:

$$P_{CV,i} = P_{CV,i-1} + dP_{CV,i}$$

Eq. (C.15)

The subscripts here refer to the current values and the previous values. The new pressure ratio was then compared to the critical pressure ratio to define the point that the

flow switched from choked to unchoked. This calculation was carried out in the attached spreadsheet on the following pages. This is a sample of the spreadsheet. The time step chosen was 0.0001 second.

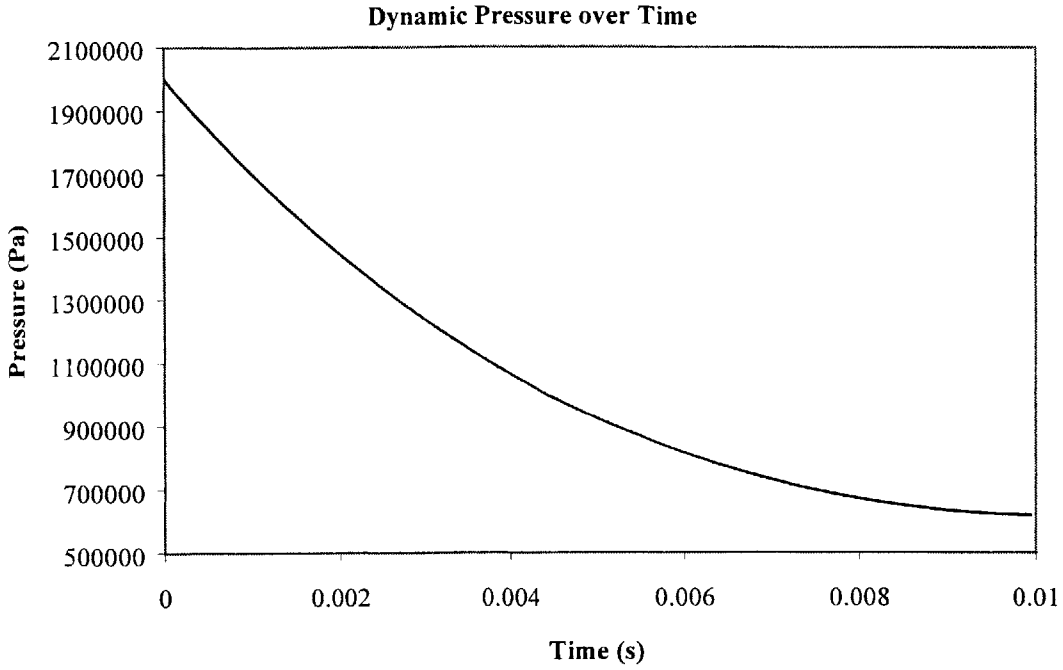

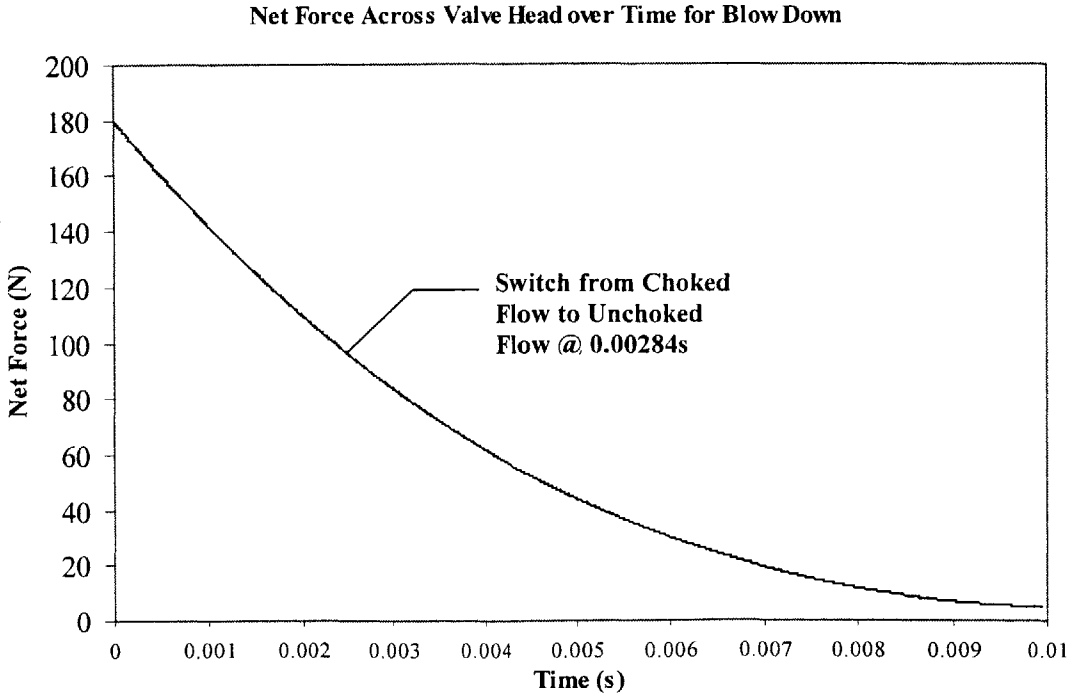

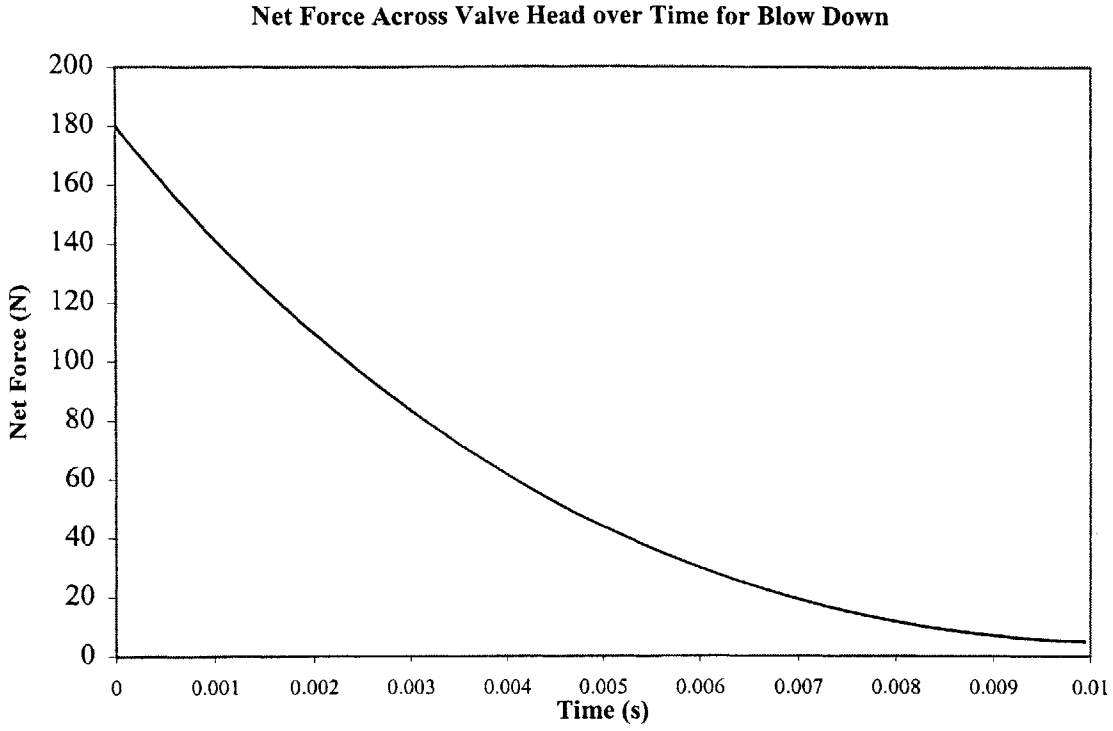
Net Force Across Valve Head over Time for Blow Down
Net Force (N)
200
180
160
140
120
100
80
60
40
20
0
0
0.001
0.002
0.003
0.004
0.005
0.006
0.007
0.008
0.009
0.01
Time (s)

APPENDIX D- Trial Data

Applied load	Spacer Thickness	Shunt Voltage	Applied Voltage	Actual Gap	Metric Gap	Metric Applied load	Current	Calculated Resistance
W	t	V s	Va	g	g	W	I	R
lbf	in	mVolts	Volts	in	m	N	Amp	Ω
0.6837	0	1.05	1.23	0.0265	6.73E-04	3.0	0.525	2.34
0.6837	0.002	1.05	1.24	0.0245	6.22E-04	3.0	0.525	2.36
0.6837	0.005	0.95	1.09	0.0215	5.46E-04	3.0	0.475	2.29
0.6837	0.01	0.8	0.99	0.0165	4.19E-04	3.0	0.4	2.48
0.6837	0.015	0.65	0.74	0.0115	2.92E-04	3.0	0.325	2.28
0.6837	0.017	0.55	0.64	0.0095	2.41E-04	3.0	0.275	2.33
0.6837	0.02	0.45	0.53	0.0065	1.65E-04	3.0	0.225	2.36
0.6837	0.022	0.35	0.39	0.0045	1.14E-04	3.0	0.175	2.23
2.1	0	1.75	2.12	0.0265	6.73E-04	9.3	0.875	2.42
2.1	0.005	1.45	1.84	0.0215	5.46E-04	9.3	0.725	2.54
2.1	0.01	1.2	1.56	0.0165	4.19E-04	9.3	0.6	2.60
2.1	0.015	0.95	1.17	0.0115	2.92E-04	9.3	0.475	2.46
2.1	0.017	0.75	1.02	0.0095	2.41E-04	9.3	0.375	2.72
2.1	0.02	0.65	0.88	0.0065	1.65E-04	9.3	0.325	2.71
2.1	0.022	0.55	0.81	0.0045	1.14E-04	9.3	0.275	2.95
2.11	0	1.4	1.57	0.0265	6.73E-04	9.4	0.7	2.24
2.11	0.002	1.3	1.58	0.0245	6.22E-04	9.4	0.65	2.43
2.11	0.005	1.3	1.47	0.0215	5.46E-04	9.4	0.65	2.26
2.11	0.01	1.05	1.23	0.0165	4.19E-04	9.4	0.525	2.34
2.11	0.015	0.9	0.99	0.0115	2.92E-04	9.4	0.45	2.20
2.11	0.017	0.7	0.85	0.0095	2.41E-04	9.4	0.35	2.43
2.11	0.02	0.6	0.7	0.0065	1.65E-04	9.4	0.3	2.33
2.11	0.022	0.55	0.6	0.0045	1.14E-04	9.4	0.275	2.18
3.46	0	1.7	1.91	0.0265	6.73E-04	15.4	0.85	2.25
3.46	0.005	1.35	1.5	0.0215	5.46E-04	15.4	0.675	2.22
3.46	0.01	1.25	1.42	0.0165	4.19E-04	15.4	0.625	2.27
3.46	0.012	1	1.14	0.0145	3.68E-04	15.4	0.5	2.28
3.46	0.015	1	1.12	0.0115	2.92E-04	15.4	0.5	2.24
3.46	0.017	0.9	1.01	0.0095	2.41E-04	15.4	0.45	2.24
3.46	0.02	0.7	0.79	0.0065	1.65E-04	15.4	0.35	2.26
3.46	0.022	0.68	0.75	0.0045	1.14E-04	15.4	0.34	2.21
4.4	0	1.85	2.13	0.0265	6.73E-04	19.6	0.925	2.30
4.4	0	1.9	2.47	0.0265	6.73E-04	19.6	0.95	2.60
4.4	0.002	1.7	1.9	0.0245	6.22E-04	19.6	0.85	2.24
4.4	0.005	1.65	1.86	0.0215	5.46E-04	19.6	0.825	2.25
4.4	0.005	1.75	2.33	0.0215	5.46E-04	19.6	0.875	2.66
4.4	0.01	1.35	1.52	0.0165	4.19E-04	19.6	0.675	2.25
4.4	0.01	1.5	1.92	0.0165	4.19E-04	19.6	0.75	2.56
4.4	0.012	1.1	1.25	0.0145	3.68E-04	19.6	0.55	2.27
4.4	0.015	1	1.1	0.0115	2.92E-04	19.6	0.5	2.20
4.4	0.015	1.15	1.6	0.0115	2.92E-04	19.6	0.575	2.78

4.4	0.017	0.85	0.85	0.0095	2.41E-04	19.6	0.425	2.00
4.4	0.017	0.95	1.48	0.0095	2.41E-04	19.6	0.475	3.12
4.4	0.02	0.8	0.8	0.0065	1.65E-04	19.6	0.4	2.00
4.4	0.02	0.9	1.32	0.0065	1.65E-04	19.6	0.45	2.93
4.4	0.022	0.75	0.75	0.0045	1.14E-04	19.6	0.375	2.00
4.4	0.022	0.8	1.21	0.0045	1.14E-04	19.6	0.4	3.03
6.51	0	2.2	2.47	0.0265	6.73E-04	29.0	1.1	2.25
6.51	0.002	2.05	2.29	0.0245	6.22E-04	29.0	1.025	2.23
6.51	0.005	1.8	2.04	0.0215	5.46E-04	29.0	0.9	2.27
6.51	0.01	1.6	1.8	0.0165	4.19E-04	29.0	0.8	2.25
6.51	0.012	1.4	1.53	0.0145	3.68E-04	29.0	0.7	2.19
6.51	0.015	1.25	1.43	0.0115	2.92E-04	29.0	0.625	2.29
6.51	0.017	1.05	1.12	0.0095	2.41E-04	29.0	0.525	2.13
6.51	0.02	1	1.09	0.0065	1.65E-04	29.0	0.5	2.18
6.51	0.022	0.85	0.94	0.0045	1.14E-04	29.0	0.425	2.21
8.8	0	2.8	3.52	0.0265	6.73E-04	39.1	1.4	2.51
8.8	0.005	2.55	3.14	0.0215	5.46E-04	39.1	1.275	2.46
8.8	0.01	2.05	2.6	0.0165	4.19E-04	39.1	1.025	2.54
8.8	0.015	1.7	2.29	0.0115	2.92E-04	39.1	0.85	2.69
8.8	0.017	1.5	1.9	0.0095	2.41E-04	39.1	0.75	2.53
8.8	0.02	1.4	1.78	0.0065	1.65E-04	39.1	0.7	2.54
8.8	0.022	1.15	1.41	0.0045	1.14E-04	39.1	0.575	2.45
10.9	0	3.15	3.47	0.0265	6.73E-04	48.5	1.575	2.20
10.9	0	3.5	4.28	0.0265	6.73E-04	48.5	1.75	2.45
10.9	0.005	2.8	2.96	0.0215	5.46E-04	48.5	1.4	2.11
10.9	0.005	3.1	3.6	0.0215	5.46E-04	48.5	1.55	2.32
10.9	0.01	2.3	2.38	0.0165	4.19E-04	48.5	1.15	2.07
10.9	0.01	2.4	3.12	0.0165	4.19E-04	48.5	1.2	2.60
10.9	0.012	2.05	2.12	0.0145	3.68E-04	48.5	1.025	2.07
10.9	0.015	1.8	1.92	0.0115	2.92E-04	48.5	0.9	2.13
10.9	0.015	1.9	2.48	0.0115	2.92E-04	48.5	0.95	2.61
10.9	0.017	1.7	1.71	0.0095	2.41E-04	48.5	0.85	2.01
10.9	0.017	1.7	2.07	0.0095	2.41E-04	48.5	0.85	2.44
10.9	0.02	1.5	1.5	0.0065	1.65E-04	48.5	0.75	2.00
10.9	0.02	1.5	1.95	0.0065	1.65E-04	48.5	0.75	2.60
10.9	0.022	1.3	1.33	0.0045	1.14E-04	48.5	0.65	2.05
10.9	0.022	1.3	1.71	0.0045	1.14E-04	48.5	0.65	2.63
15.9	0	4.85	5.91	0.0265	6.73E-04	70.7	2.425	2.44
15.9	0.005	4	4.72	0.0215	5.46E-04	70.7	2	2.36
15.9	0.01	3.15	3.83	0.0165	4.19E-04	70.7	1.575	2.43
15.9	0.015	2.5	3.16	0.0115	2.92E-04	70.7	1.25	2.53
15.9	0.017	2.05	2.6	0.0095	2.41E-04	70.7	1.025	2.54
15.9	0.02	1.85	2.39	0.0065	1.65E-04	70.7	0.925	2.58
15.9	0.022	1.7	2.09	0.0045	1.14E-04	70.7	0.85	2.46
15.99	0	4.4	4.93	0.0265	6.73E-04	71.1	2.2	2.24
15.99	0.005	3.7	4.04	0.0215	5.46E-04	71.1	1.85	2.18
15.99	0.01	3	3.26	0.0165	4.19E-04	71.1	1.5	2.17
15.99	0.012	2.7	2.92	0.0145	3.68E-04	71.1	1.35	2.16

15.99	0.015	2.3	2.5	0.0115	2.92E-04	71.1	1.15	2.17
15.99	0.017	2.1	2.25	0.0095	2.41E-04	71.1	1.05	2.14
15.99	0.02	1.9	1.95	0.0065	1.65E-04	71.1	0.95	2.05
15.99	0.022	1.5	1.51	0.0045	1.14E-04	71.1	0.75	2.01
18.72	0	5	5.58	0.0265	6.73E-04	83.3	2.5	2.23
18.72	0.005	4.1	4.5	0.0215	5.46E-04	83.3	2.05	2.20
18.72	0.01	3.3	3.62	0.0165	4.19E-04	83.3	1.65	2.19
18.72	0.012	2.9	3.11	0.0145	3.68E-04	83.3	1.45	2.14
18.72	0.015	2.6	2.75	0.0115	2.92E-04	83.3	1.3	2.12
18.72	0.017	2.2	2.3	0.0095	2.41E-04	83.3	1.1	2.09
18.72	0.02	1.9	1.95	0.0065	1.65E-04	83.3	0.95	2.05
18.72	0.022	1.7	1.75	0.0045	1.14E-04	83.3	0.85	2.06
19.45	0	5.5	6.17	0.0265	6.73E-04	86.5	2.75	2.24
19.45	0.005	4.6	5.11	0.0215	5.46E-04	86.5	2.3	2.22
19.45	0.01	3.6	4.02	0.0165	4.19E-04	86.5	1.8	2.23
19.45	0.012	2.9	3.23	0.0145	3.68E-04	86.5	1.45	2.23
19.45	0.015	2.8	2.99	0.0115	2.92E-04	86.5	1.4	2.14
19.45	0.017	2.3	2.4	0.0095	2.41E-04	86.5	1.15	2.09
19.45	0.02	2	2.06	0.0065	1.65E-04	86.5	1	2.06
19.45	0.022	1.7	1.75	0.0045	1.14E-04	86.5	0.85	2.06
24.45	0.01	4.75	5.45	0.0165	4.19E-04	108.8	2.375	2.29
24.45	0.012	4.2	4.7	0.0145	3.68E-04	108.8	2.1	2.24
24.45	0.015	3.6	4.01	0.0115	2.92E-04	108.8	1.8	2.23
24.45	0.017	3	3.32	0.0095	2.41E-04	108.8	1.5	2.21
24.45	0.02	2.4	2.63	0.0065	1.65E-04	108.8	1.2	2.19
24.45	0.022	2.2	2.3	0.0045	1.14E-04	108.8	1.1	2.09
25	0	8.25	9.27	0.0265	6.73E-04	111.2	4.125	2.25
25	0	8	9.31	0.0265	6.73E-04	111.2	4	2.33
25	0.005	7.25	8.07	0.0215	5.46E-04	111.2	3.625	2.23
25	0.005	6.6	7.86	0.0215	5.46E-04	111.2	3.3	2.38
25	0.01	6	6.32	0.0165	4.19E-04	111.2	3	2.11
25	0.01	5.3	6.14	0.0165	4.19E-04	111.2	2.65	2.32
25	0.015	4.5	4.5	0.0115	2.92E-04	111.2	2.25	2.00
25	0.015	3.7	4.18	0.0115	2.92E-04	111.2	1.85	2.26
25	0.017	4	3.9	0.0095	2.41E-04	111.2	2	1.95
25	0.017	3.3	3.75	0.0095	2.41E-04	111.2	1.65	2.27
25	0.02	3.25	3.37	0.0065	1.65E-04	111.2	1.625	2.07
25	0.02	2.7	3.27	0.0065	1.65E-04	111.2	1.35	2.42
25	0.022	3	2.55	0.0045	1.14E-04	111.2	1.5	1.70
25	0.022	2.5	2.75	0.0045	1.14E-04	111.2	1.25	2.20
28.45	0.01	5.7	6.51	0.0165	4.19E-04	126.5	2.85	2.28
28.45	0.012	5	5.8	0.0145	3.68E-04	126.5	2.5	2.32
28.45	0.015	4.4	5.02	0.0115	2.92E-04	126.5	2.2	2.28
28.45	0.017	3.7	4.25	0.0095	2.41E-04	126.5	1.85	2.30
28.45	0.02	3.1	3.45	0.0065	1.65E-04	126.5	1.55	2.23
28.45	0.022	2.7	2.95	0.0045	1.14E-04	126.5	1.35	2.19
29.4	0	10.15	13.23	0.0265	6.73E-04	130.8	5.075	2.61
29.4	0.005	9.1	11.26	0.0215	5.46E-04	130.8	4.55	2.47

29.4	0.01	6.3	7.76	0.0165	4.19E-04	130.8	3.15	2.46
29.4	0.015	5.4	6.45	0.0115	2.92E-04	130.8	2.7	2.39
29.4	0.017	4.6	5.54	0.0095	2.41E-04	130.8	2.3	2.41
29.4	0.02	3.7	4.48	0.0065	1.65E-04	130.8	1.85	2.42
29.4	0.022	2.75	3.53	0.0045	1.14E-04	130.8	1.375	2.57
33.45	0.017	5	5.8	0.0095	2.41E-04	148.8	2.5	2.32
33.45	0.02	3.9	4.49	0.0065	1.65E-04	148.8	1.95	2.30
33.45	0.022	2.9	3.33	0.0045	1.14E-04	148.8	1.45	2.30
33.8	0.005	11	14.81	0.0215	5.46E-04	150.3	5.5	2.69
33.8	0.01	8.4	12.06	0.0165	4.19E-04	150.3	4.2	2.87
33.8	0.015	6	8.09	0.0115	2.92E-04	150.3	3	2.70
33.8	0.017	5.5	7.29	0.0095	2.41E-04	150.3	2.75	2.65
33.8	0.02	4.4	5.97	0.0065	1.65E-04	150.3	2.2	2.71
33.8	0.022	3.7	4.92	0.0045	1.14E-04	150.3	1.85	2.66
43.3	0.017	10.5	12.1	0.0095	2.41E-04	192.6	5.25	2.30
43.3	0.02	8.5	9.6	0.0065	1.65E-04	192.6	4.25	2.26
43.3	0.022	6.5	7.5	0.0045	1.14E-04	192.6	3.25	2.31
48.5	0.017	13	17.0000	0.0095	2.41E-04	215.7	6.5	2.62
48.5	0.02	11.5	15.0000	0.0065	1.65E-04	215.7	5.75	2.61
48.5	0.022	10.0000	13.3000	0.0045	1.14E-04	215.7	5	2.66

APPENDIX E- X-Factor Development

In a perfect world the magnetic circuit would be represented by the following figure.

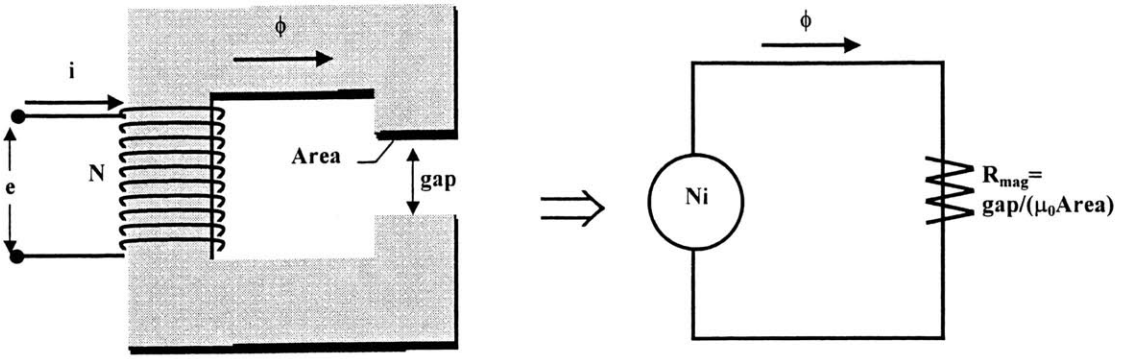

(a) Electromagnetic Circuit **(b) Equivalent Electrical Circuit Analogy**

This model would consist of a single loop circuit with just one source and just on resistance. In this case the magnetic force would be easily calculated by:

$$F_{magnetic} = \frac{B^2 A_{core}}{2\mu_0} \qquad \textbf{Eq. (E.1)}$$

and the magnetic field would be

$$B = \frac{Ni_{observed}\mu_0}{gap} \qquad \textbf{Eq. (E.2)}$$

The reluctance was defined as

$$\mathrm{Re}\, l = \frac{gap}{\mu_0 A_{core}} \qquad \textbf{Eq. (E.3)}$$

These relations gave

$$B = Ni_{observed}\left(\frac{A_{core}}{\mathrm{Re}\, l}\right) \qquad \textbf{Eq. (E.4)}$$

However, in the not so perfect world that we live in, is was known that the single loop circuit was not the correct representation of the actual physical circuit. This physical circuit was better represented by the following figure.

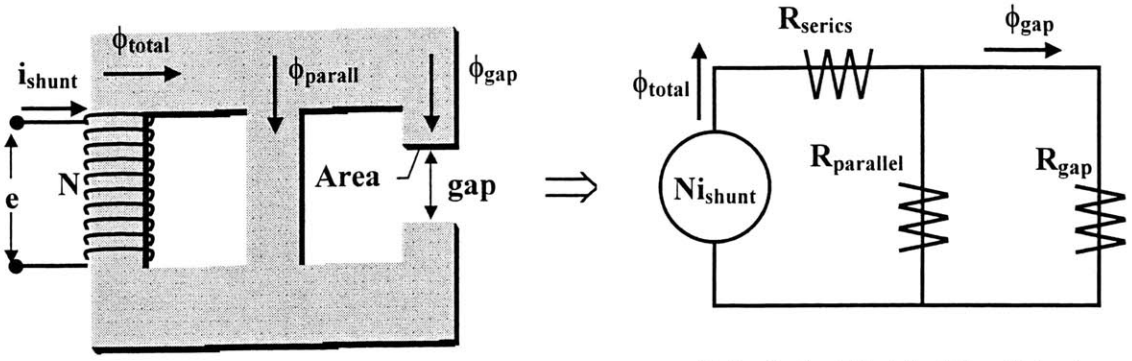

(a) Electromagnetic Circuit

(b) Equivalent Electrical Circuit Analogy

In this figure the equivalent electrical circuit reveals that i is represented by ϕ, V by Ni and R by Rel.

Kirkoff's and Amperes laws were applied to this circuit to get:

$$\phi_{total} = Ni_{observed}\left[R_{series} + \left[\frac{1}{\frac{1}{R_{para}} + \frac{1}{R_{gap}}}\right]\right] \qquad \textbf{Eq. (E.5)}$$

or

$$Ni = \phi_{total}\left[R_{series} + \left[\frac{1}{\frac{1}{R_{para}} + \frac{1}{R_{gap}}}\right]\right]^{-1}$$

In a similar examination is was also found that

$$\phi_{para} + \phi_{gap} = \phi_{series} = \phi_{total}$$

which yeilds

$$Ni_{observed} - \left(\phi_{para} + \phi_{gap}\right)R_{series} = R_{para}\phi_{para} \qquad \textbf{Eq. (E.6)}$$

and

$$Ni_{observed} - \left(\phi_{para} + \phi_{gap}\right)R_{series} = R_{gap}\phi_{gap}$$

Finally, after substitution and simplification, we arrive at

$$\phi_{gap}R_{gap} = Ni_{observed} - R_{series}\left(\frac{Ni_{observed} - \phi_{para}R_{para}}{R_{para}}\right)$$

$$\phi_{gap}R_{gap} = N\ i_{observed} - \frac{R_{series}}{R_{paral}}Ni_{observed} - R_{series}\phi_{para} \qquad \textbf{Eq. (E.7)}$$

All of this was substituted into the force equation to arrive at the following.

$$\sqrt{\frac{2F_{applied}}{(A_{core}\mu_0)^3}}gap^3 = Ni_{observed}\left[1 - \frac{R_{series}}{R_{para}}\right] - R_{series}\phi_{para} \qquad \textbf{Eq. (E.8)}$$

In this equation, the term on the left hand side was fully defined by the measured values. Ni was also measured. This left R_{series}, $R_{parallel}$ and $\phi_{parallel}$ to be determined. The data was then used to extrapolate the values of each of these unknowns between consecutive points.

From this relation, it was not possible to solve for R_{series}, $R_{parallel}$ or $\phi_{parallel}$ independently. From this information it was determined that the three unknowns were not independent, but were instead linear in the measure force, current and gap geometry. Thus a correlation had to be developed in order to relate the three quantities $i_{applied}$, $F_{applied}$, and gap.

Referring again to figure G.2, the relationship between the three reluctances was defined as:

$$Ni_{observed} - (\phi_{para} + \phi_{gap})R_{series} = R_{gap}\phi_{gap} \qquad \textbf{Eq. (E.9)}$$

As before, i in this equation is the current through the shunt resistor, which is also the current through the coil. However, applying Kirkoff's Laws in a different manner, the following equalities were found.

$$\phi_{total} = \phi_{gap} + \phi_{para}$$
$$(Ni)_{gap} = (Ni)_{para} \qquad \textbf{Eq. (E.10)}$$

Adding the reluctances to these two expressions, we had:

$$\phi_{gap}\left(\frac{l}{A\mu}\right)_{gap} = \phi_{para}\left(\frac{l}{A\mu}\right)_{para}$$

to get

$$\frac{\phi_{total}}{\phi_{gap}} = \left[1+\frac{\left(\frac{l}{A\mu}\right)_{gap}}{\left(\frac{l}{A\mu}\right)_{para}}\right] \qquad \textbf{Eq. (E.11)}$$

$$\frac{\phi_{total}}{\phi_{gap}} = \left[1+\frac{\left(\frac{gap}{A_{core}}\right)_{gap}\left(\frac{\mu_{para}}{\mu_0}\right)}{\left(\frac{l}{A}\right)_{para}}\right]$$

It was then attempted to characterize the right hand side of this equation. However, that data did not come in the flavor of flux and reluctance; it tasted more like force and current. So, we moved in the direction of defining this relationship in terms of force and current.

From the constitutive relations, the expected current was defined in terms of the applied force.

$$F_{applied} = \frac{\mu_0 A_{core}}{2}\left[\frac{Ni_{theoretical}}{gap_{theoretical}}\right]^2 \qquad \textbf{Eq. (E.12)}$$

From this, t was observed that three factors had to be characterized; $F_{applied}$, i_{obs}, and gap.

Next, examination of the plots of gap versus current at constant force revealed a linear relationship between the two quantities. It was further seen that each of the curves converged on the same y intercept of 0.006-inch. This indicated that the current did not appear to be zero when the actual gap was zero. The 0.006-inch mark indicated the amount by which the gap appeared to be larger in the circuit, thus:

$$gap_{theoretical} = gap_{actual} + 0.006 - inch \qquad \textbf{Eq. (E.13)}$$

Now, noting that the linear relationship between gap and current existed, see the attached 'Gap vs. Current' plots, the following relationship was defined.

$$\left(\frac{i_{observed}}{gap_{theoretical}}\right) = \sqrt{\frac{2F_{applied}}{N^2\mu_0 A_{core}}} \qquad \textbf{Eq. (E.14)}$$

This relationship defined the correlation between the force, current and gap as the X-Factor or the ratio of the theoretical current to the observed current.

$$\frac{i_{theoreticl}}{i_{observed}} = \mathrm{X} = \sqrt{\frac{2F_{applied}}{N^2 \mu_0 A_{core}}} \frac{gap_{theoretical}}{i_{observed}}$$

and

$$\frac{gap_{theoretical}}{i_{obvserved}} = \sqrt{\frac{N^2 \mu_0 A_{core}}{2F_{applied}}} \cdot \mathrm{X}$$

Eq. (E.15)

The slopes of each of the Gap versus current lines was noted. Since the theoretical gap was simply a linear shift of the actual gap, the same slope applied. These slopes were plotted versus applied load and two functions were defined.

$$f(F_{applied}) = 0.003\left(\frac{in}{Amp}\right) + 0.065\left(\frac{in}{Amp}\right) \cdot \exp\left[-0.115\left(\frac{1}{lbf}\right)\left(1.09lbf + F_{applied}\right)\right]$$

Eq. (E.16)

The final result is two equations for the X-factors.

$$\mathrm{X} = \sqrt{\frac{2F_{applied}}{\mu_0 A_{core} N^2}} \cdot 0.003\left(\frac{in}{Amp}\right) + 0.065\left(\frac{in}{Amp}\right) \cdot \exp\left[-0.115\left(\frac{1}{lbf}\right)\left(1.09lbf + F_{applied}\right)\right]$$

Eq. (E.17)

Slopes	Applied load	Equation Fit	X-Factor	Metric Slopes	Metric Applied load	Equation Fit	X-Factor
in/A	lbf	in/A		m/A	N	m/A	
0.0581	0.68	0.056029	3211.18	0.001480	3.025	0.0013126	0.2962
0.0439	2.11	0.047988	4844.72	0.001110	9.385	0.0011476	0.4561
0.0375	3.46	0.041518	5367.57	0.000953	15.390	0.0010125	0.5153
0.0345	4.40	0.037572	5477.55	0.000877	19.571	0.0009288	0.5331
0.0291	6.51	0.030123	5341.82	0.000738	28.956	0.0007679	0.5361
0.0195	10.90	0.019371	4445.01	0.000495	48.483	0.0005262	0.4754
0.0148	15.99	0.012117	3367.70	0.000376	71.124	0.0003532	0.3865
0.0134	18.72	0.009661	2905.12	0.000340	83.267	0.0002915	0.3451
0.0124	19.45	0.009124	2796.82	0.000314	86.514	0.0002777	0.3352
0.0098	24.45	0.006446	2215.36	0.000248	108.754	0.0002066	0.2795
0.008	28.45	0.005176	1918.66	0.000204	126.546	0.0001708	0.2493
0.0064	33.45	0.004224	1698.01	0.000164	148.786	0.0001424	0.2254
0.003	43.50	0.003385	1551.86	0.000076	160.000	0.0001328	0.2179
0.00224	48.50	0.003217	1557.05	0.000057	175.000	0.0001232	0.2115

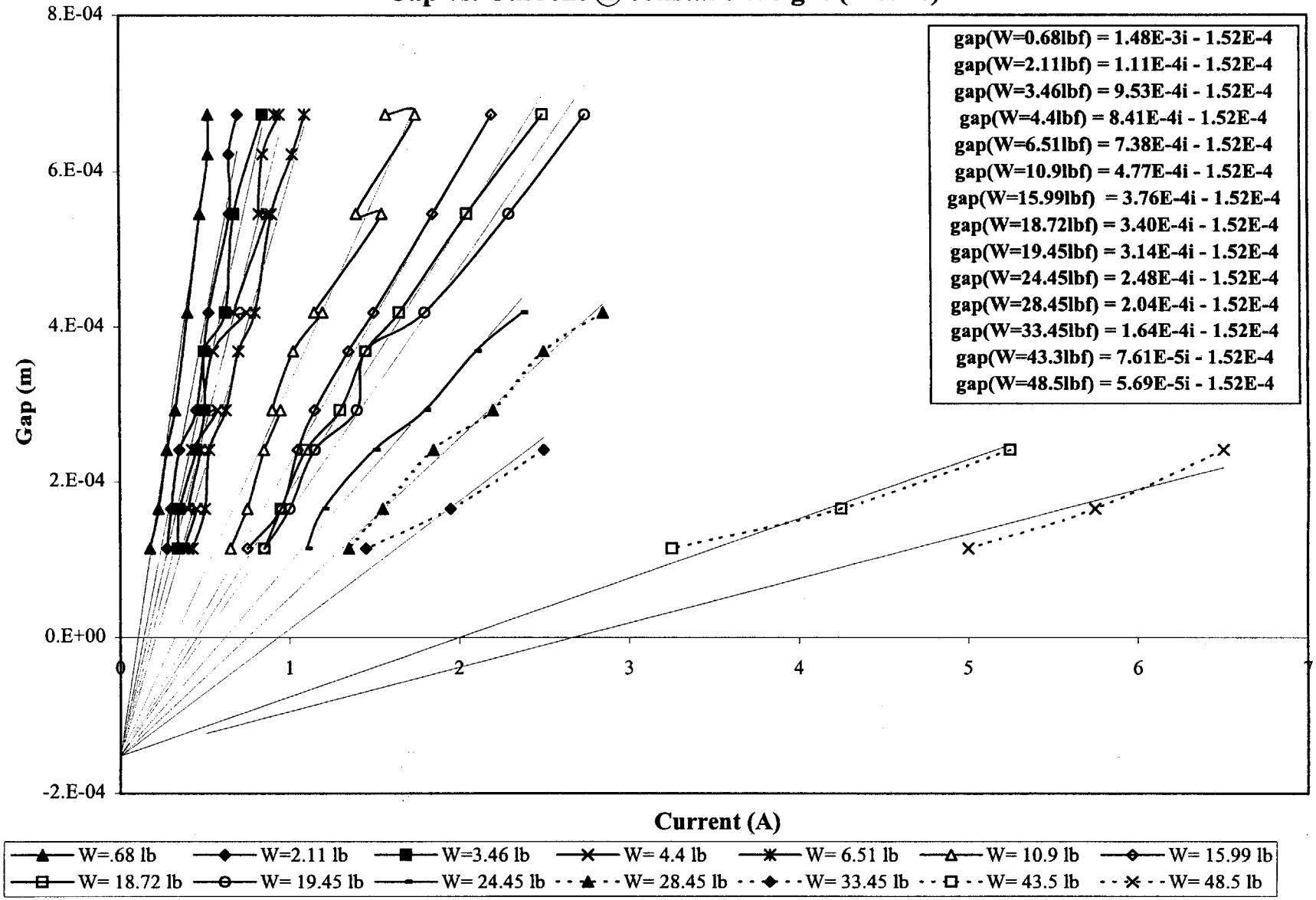
Gap vs. Current @ constant Weight (Metric)
8.E-04
6.E-04
4.E-04
2.E-04
0.E+00
-2.E-04
Gap (m)
0
1
2
3
4
5
6
7
Current (A)
gap(W=0.68lbf) = 1.48E-3i - 1.52E-4
gap(W=2.11lbf) = 1.11E-4i - 1.52E-4
gap(W=3.46lbf) = 9.53E-4i - 1.52E-4
gap(W=4.4lbf) = 8.41E-4i - 1.52E-4
gap(W=6.51lbf) = 7.38E-4i - 1.52E-4
gap(W=10.9lbf) = 4.77E-4i - 1.52E-4
gap(W=15.99lbf) = 3.76E-4i - 1.52E-4
gap(W=18.72lbf) = 3.40E-4i - 1.52E-4
gap(W=19.45lbf) = 3.14E-4i - 1.52E-4
gap(W=24.45lbf) = 2.48E-4i - 1.52E-4
gap(W=28.45lbf) = 2.04E-4i - 1.52E-4
gap(W=33.45lbf) = 1.64E-4i - 1.52E-4
gap(W=43.3lbf) = 7.61E-5i - 1.52E-4
gap(W=48.5lbf) = 5.69E-5i - 1.52E-4
W=.68 lb
W=2.11 lb
W=3.46 lb
W= 4.4 lb
W= 6.51 lb
W= 10.9 lb
W= 15.99 lb
W= 18.72 lb
W= 19.45 lb
W= 24.45 lb
W= 28.45 lb
W= 33.45 lb
W= 43.5 lb
W= 48.5 lb

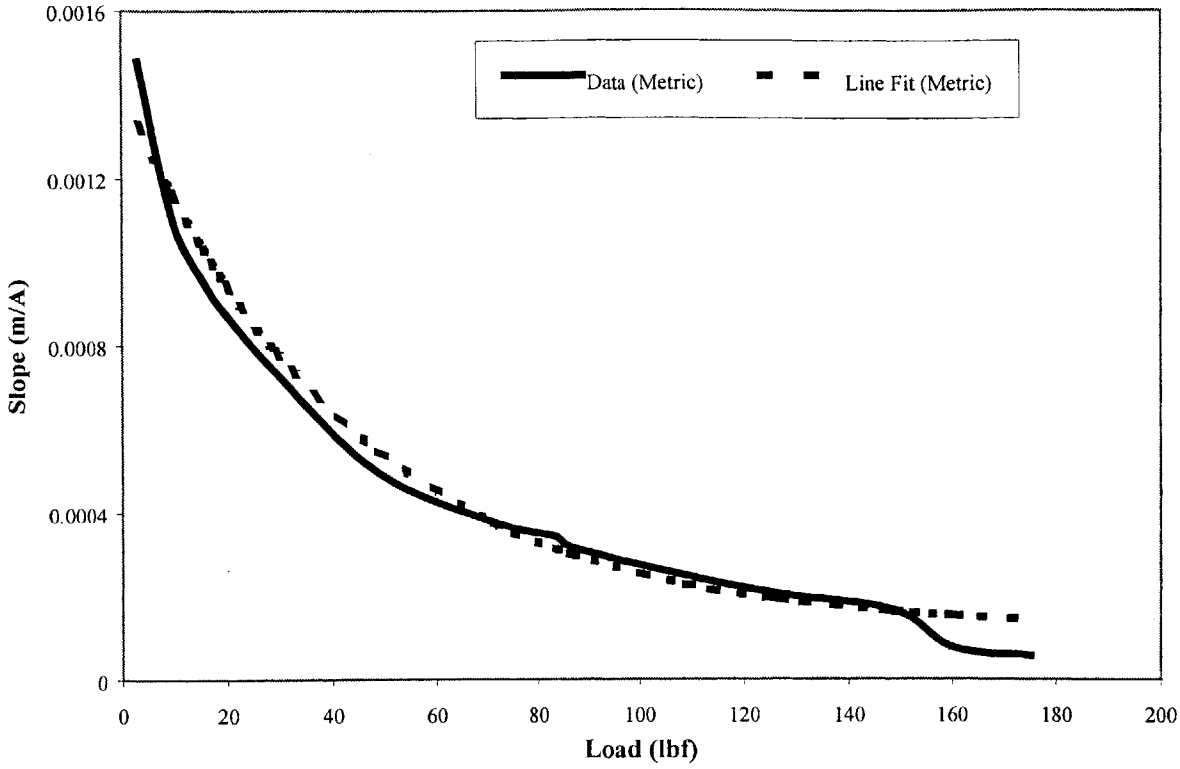

X-Factor (Metric)

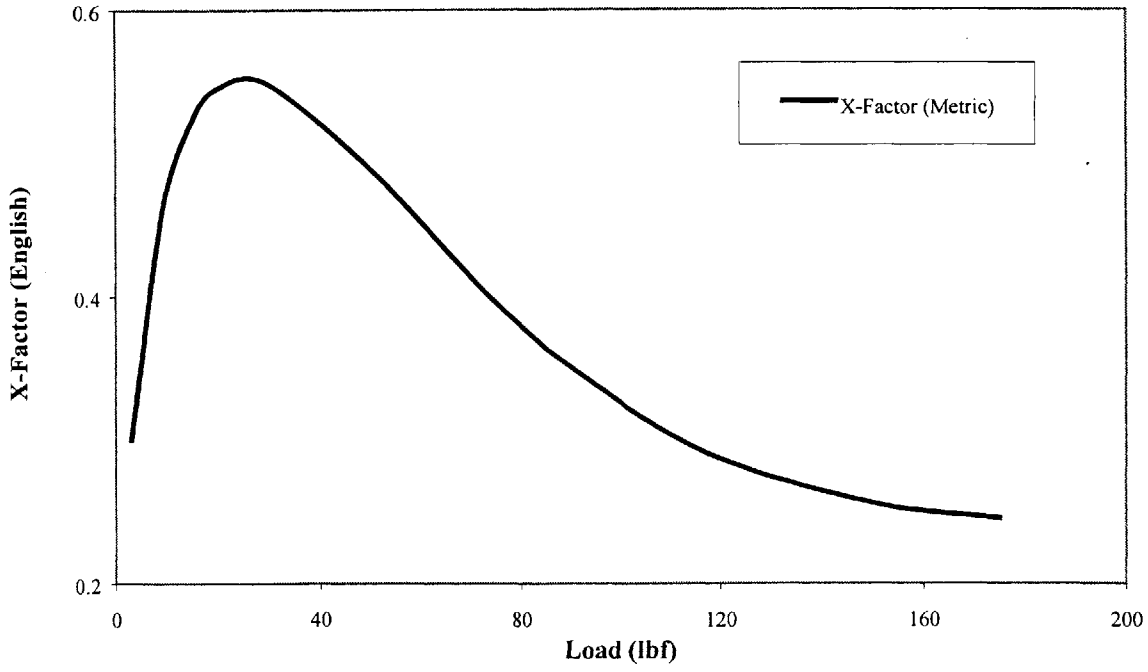

APPENDIX F- EM Relationships

F-I Applying the X-Factor

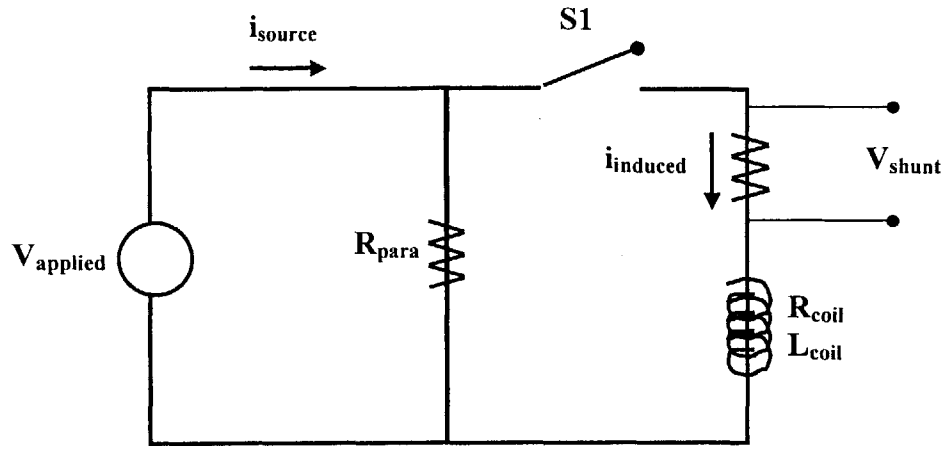

From the above circuit, shunt voltage and applied voltage were noted for various combinations of applied load and gap geometry. This data was then correlated to formulated the following two correlations.

$$X = \sqrt{\frac{2F_{applied}}{\mu_0 A_{core} N^2}} \cdot 0.003\left(\frac{in}{Amp}\right) + 0.065\left(\frac{in}{Amp}\right) \cdot \exp\left[-0.115\left(\frac{1}{lbf}\right)\left(1.09lbf + F_{applied}\right)\right]$$

Eq. (F.1)

The X-Factor was then related to the flux in the magnetic circuit.. From theory, the flux across the gap was:

$$\phi_{gap} = \sqrt{2\mu_0 A_{core} F_{applied}} = \frac{N i_{theoretical} \mu_0 A_{core}}{gap} \qquad \textbf{Eq. (F.2)}$$

Applying the X-Factor correlations to this equation yields:

$$i_{observed} = \frac{gap\phi_{gap}}{N\mu_0 A_{core}} \cdot \frac{1}{X_{current}} \qquad \textbf{Eq. (F.3)}$$

From theory, it is also know that the voltage across the inductor was related to flux by:

$$V_{inductor} = N\frac{d\phi_{total}}{dt} \qquad \textbf{Eq. (F.4)}$$

Where, from the above circuit, the voltage across the inductor was defined as:

$$V_{inductor} = V_{applied} - i_{observed} R_{shunt} \qquad \textbf{Eq. (F.5)}$$

Solving for the change in flux over time to get:

$$\frac{d\phi_{total}}{dt} = \frac{1}{N}\left(V_{applied} - R_{shunt}\left(\frac{gap\phi_{gap}}{N\mu_0 A_{coil}} \cdot \frac{1}{X}\right)\right) \qquad \textbf{Eq. (F.6)}$$

For simplification, the constant C_ϕ was defined as:

$$C_\phi = \frac{R_{shunt}}{N\mu_0 A_{core}} \qquad \textbf{Eq. (F.7)}$$

The end result is a differential equation in terms of time. This differential was then used to characterize the flux in the gap over time by a step-wise integration.

$$d\phi_{total} = \frac{1}{N}\left(V_{applied} - C_\phi \frac{gap\phi_{gap}}{X}\right)dt$$

$$\phi_{total,i} = \phi_{total,i-1} + d\phi_{total,i-1} \qquad \textbf{Eq. (F.8)}$$

This relationship is fine for simply determining the flux in a stationary gap over time. However, what we had here was in fact a changing gap geometry- a dynamic situation. This warranted the use of mechanics to characterize the actual motion of the core. The following free body diagram was used for this purpose.

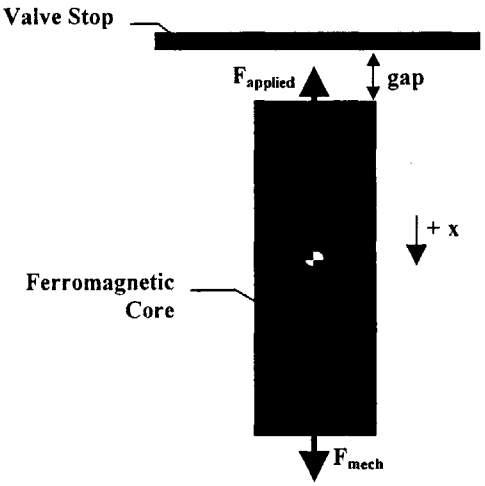

From a force balance on the Ferromagnetic Core, we get:

$$m_{core}a_{core} = m_{core}\frac{dvel_{core}}{dt} = F_{mag} - F_{applied} \qquad \textbf{Eq. (F.9)}$$

From theory the expression for $F_{applied}$ was as follows:

$$F_{mech} = \frac{\phi_{gap}^2}{2\mu_0 A_{core}}$$

$$let \qquad \text{Eq. (F.10)}$$

$$C_{vel} = \frac{1}{2\mu_0 A_{core}}$$

If the Equation E.9 was used in solving for $F_{applied}$, then the X-Factor was already factored into the expression.
$F_{applied}$ was substituted and the change in velocity over time was determined.

$$dvel_{core} = \left(\frac{F_{mech} - \phi_{gap}^2 C_{vel}}{m_{core}} \right) dt$$

Eq. (F.11)

$$vel_{core,i} = vel_{core,i-1} + dvel_{core,i-1}$$

The gap geometry and thus the head position could then be found by

$$gap_i = vel_{core,i} dt$$

Eq. (F.12)

$$Lift = gap_0 - gap_i$$

F-II Driven by a step input

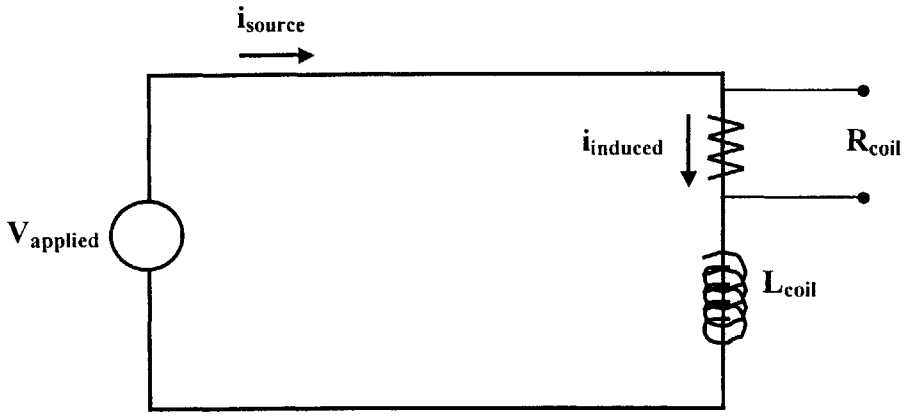

Now, that the dynamics of the experimental circuit were determined it was time to apply this knowledge to the valve as it would operate in the cold head. The previous circuit is a representation of how the valve would appear in a step input circuit.

From this circuit and from the previous development it is obvious that the change in flux over time appeared as:

$$C_\phi = \frac{R_{coil}}{N\mu_0 A_{core}}$$

$$d\phi_{gap} = \frac{1}{N}\left(V_{applied} - C_\phi \frac{gap\phi_{gap}}{X}\right)dt \qquad \textbf{Eq. (F.13)}$$

$$\phi_{gap,i} = \phi_{gap,i-1} + d\phi_{gap,i-1}$$

The only difference between this and Equation E.8, was the value of the series resistance.

The major difference arose in the development of the velocity. Again, a free body diagram was consulted for the analysis.

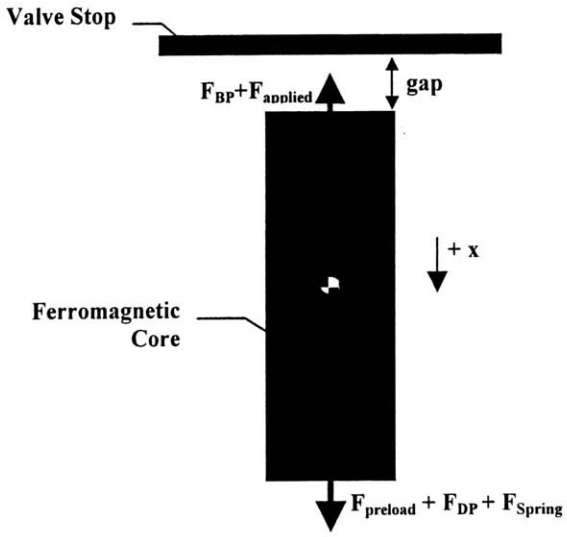

From this new free body diagram the force balance turns out as:

$$dvel_{core} = \left[\frac{F_{preload} + k_{sp}(gap_{initial} - gap_i) + F_{DP} - F_{BP} - C_{vel}\phi_{gap}{}^2}{m_{core}}\right]dt \qquad \textbf{Eq. (F.14)}$$

Where the change in Dynamic Pressure over time were defined in the fluid dynamic analysis as:

$$dP_{CV} = \left[\left(\frac{\forall_{CV}}{R_{He}}\right)\left(\frac{P_H}{T_0}\right)\frac{1}{\gamma}\left(\frac{P_{CV}^{\frac{1-\gamma}{\gamma}}}{P_H^{1/\gamma}}\right)\right]^{-1} \dot{m}_{CV}\,dt \qquad \textbf{Eq. (F.15)}$$

The Back Pressure remained constant throughout the process.

The spring force was broken into the preload force, which arose from the amount the spring is compressed when the valve was in the closed position. The amount the spring was compressed throughout the valve motion then defined the dynamic spring force as:

$$F_{spring} = F_{preload} + k_{sp}\left(gap_{initial} - gap_i\right) \qquad \textbf{Eq. (F.16)}$$

Thus, when the input to the circuit was a step voltage, the motion of the valve head was again defined as:

$$vel_{core,i} = vel_{core,i-1} + dvel_{core,i-1}$$

$$gap_i = vel_{core,i}dt \qquad \textbf{Eq. (F.17)}$$

$$Lift = gap_0 - gap_i$$

F-III Changing the Source to an RC Circuit

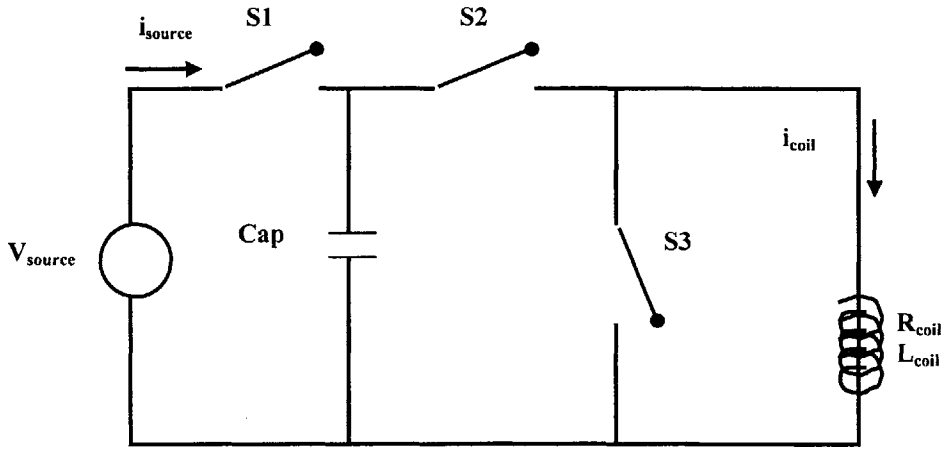

Looking at this new circuit, the valve was to be driven by the discharge of a large capacitance into the valve circuit. This was to be achieved by closing switch S1 and charging the capacitor to V_{source}. Once this was complete, switch S1 is opened and switch S2 is closed allowing the capacitor to discharge into the coil. In this case the source appears as a time varying input rather than the step input as defined previously. Now, the change in flux over time appears as:

$$C_\phi = \frac{R_{coil}}{N\mu_0 A_{core}}$$

$$d\phi_{gap} = \frac{1}{N}\left(V_{capacitor} - C_\phi \frac{gap\phi_{gap}}{X}\right)dt \qquad \textbf{Eq. (F.18)}$$

$$\phi_{gap,i} = \phi_{gap,i-1} + d\phi_{gap,i-1}$$

Now, things are made interesting by the dynamics of $V_{capacitor}$. A capacitor's charge, current and change in voltage over time are defined as:

$$charge = V_{capacitor} C$$

$$\frac{dcharge}{dt} = i_{observed} = C\frac{dV_{capacitor}}{dt} \qquad \textbf{Eq. (F.19)}$$

$$so$$

$$dV_{caacitor} = \frac{i_{observed}}{C}dt$$

Taking a step-wise integration over time of this results in:

$$V_{capacitor,i} = V_{capacitor,i-1} + dV_{capacitor,i-1} \qquad \textbf{Eq. (F.20)}$$

This expression was then used in Equations E.18 to solve for the flux. Again, the same equations for the change in velocity over time were used to examine the valve dynamics.

To review from the top the equations integrated over time to define the dynamics of the valve head are as follows:

$$C_\phi = \frac{R_{coil}}{N\mu_0 A_{core}}$$

$$d\phi_{gap} = \frac{1}{N}\left(V_{capacitor} - C_\phi \frac{gap\phi_{gap}}{X}\right)dt \qquad \textbf{Eq. (F.21)}$$

$$\phi_{gap,i} = \phi_{gap,i-1} + d\phi_{gap,i-1}$$

$$F_{applied} = \frac{\phi_{gap}^2}{2\mu_0 A_{core}}$$

$$dvel_{core} = \left[\frac{F_{preload} + k_{sp}(gap_{initial} - gap_i) + F_{DP} - F_{BP} - C_{vel}\phi^2}{m_{core}} \right] dt$$

$$vel_{core,i} = vel_{core,i-1} + dvel_{core,i-1}$$

$$gap_i = vel_{core,i} dt$$

$$Lift = gap_0 - gap_i$$

Eq. (F.22)

$$dP_{unchoked} = \frac{-\gamma A_{curtain}}{\forall_{CV}} \sqrt{5 R_{He} T_0} \left[\left(\frac{P_H}{P_{CV}} \right)^{\frac{1-\gamma}{\gamma}} P_L^{\frac{1+\gamma}{\gamma}} \left(\left(\frac{P_{CV}}{P_L} \right)^{\frac{\gamma-1}{\gamma}} - 1 \right) \right]^{1/2} dt$$

Eq. (F.23)

$$dP_{choked} = \frac{-\gamma K R_{He} A_{curtain}}{\forall_{CV}} \sqrt{T_0} \left[\frac{P_H^{\frac{1-\gamma}{2\gamma}}}{P_{CV}^{\frac{1+\gamma}{2\gamma}}} \right] dt$$

These equations were used in the attached spreadsheet to calculate the valve dynamics over time.

F-IV Energy of system over time

Given the dynamics of the valve over time, it was also desired to know the energy consumption of the valve at each time step. Examination of the flow chart below defined the energy flows in the system.

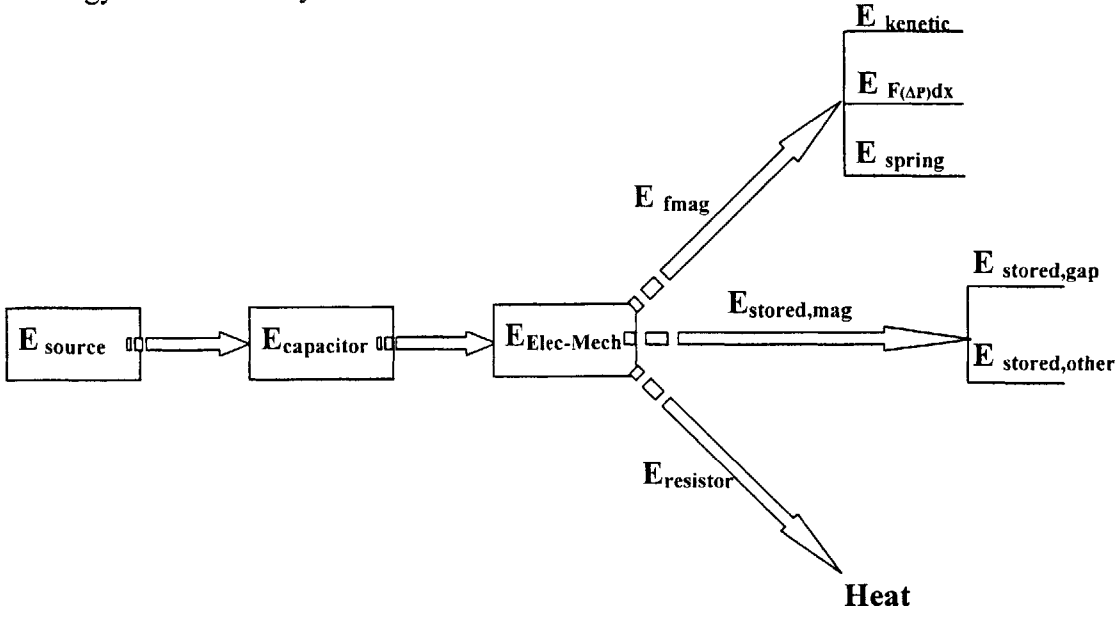

From theory and the previous development, each of these energies was defined.

The Energy produced by the capacitor was:

$$dE_{capacitor} = V_{cap} i_{coil} dt$$

$$E_{capacitor,i} = E_{capacitor,i-1} - dE_{capacitor,i} \qquad \textbf{Eq. (F.24)}$$

The instantaneous kinetic energy of any moving mass is defined as:

$$dE_{kenetic} = \frac{m_{core}}{2} \Delta\left(vel_{core}^2\right)$$

$$E_{kinetic,i} = E_{kinetic,i-1} + dE_{kenetic,i} \qquad \textbf{Eq. (F.25)}$$

The energy stored in the compression spring was:

$$dE_{spring} = k_{sp} \Delta gap$$

$$E_{spring} = E_{spring,i} + dE_{spring,i} \qquad \textbf{Eq. (F.26)}$$

The energy used to displace the fluid under pressure was:

$$dE_{F_{\Delta P} dx} = \left(F_{DP} - F_{BP}\right) \Delta gap$$

$$E_{F_{\Delta P} dx,i} = E_{F_{\Delta P} dx,i-1} + dE_{F_{\Delta P} dx,i} \qquad \textbf{Eq. (F.27)}$$

The energy lost to dissipative resistance was defined as:

$$dE_{resistor} = i_{observed}^2 R_{coil} dt$$

$$E_{resistor,i} = E_{resistor,i-1} + dE_{resistor,i} \qquad \textbf{Eq. (F.28)}$$

The energy stored in the magnetic coil was composed of two components; the storage in the gap and the storage in the leakage field:

$$dE_{stored}\ \frac{\Delta\left(\phi_{total}^{2}\, gap\right)}{2\mu_0 A_{coil}}$$

$$dE_{stored,gap} = \frac{\Delta\left(\phi_{gap}^{2}\, gap\right)}{2\mu_0 A_{coil}} \qquad \textbf{Eq. (F.29)}$$

$$dE_{stored,other} = dE_{stored} - dE_{stored,gap}$$

$$E_{stored,i} = E_{stored,i-1} - dE_{stored,i}$$

Finally, it was known that part of the magnetic field generated went into a force producing field and part went into a non-force producing field, also termed the flux leakage.

$$dE_{Fmag} = F_{mag}\, dx^2$$

Eq. (F.30)

$$\frac{dE_{leakage}}{dt} = V_{cap} i_{coil} \mathrm{X}$$

Where the first equation describes the energy generating the force producing magnetic field and the second describes the energy generating the non-force producing magnetic field.

All of these energies were equated to satisfy the first law of thermodynamics as follows:

$$E_{capacitor} = E_{resistor} + E_{kinetic} + E_{F_{\Delta P}dx} + E_{spring} + E_{stored,gap} + E_{stored,other}$$

$$E_{fmag} = E_{kenetic} + E_{F_{\Delta P}dx} + E_{spring} \qquad \textbf{Eq. (F.31)}$$

$$E_{stored,mag} = E_{stored,gap} + E_{stored,other}$$

Each energy was examined to determine the amounts dissipated and the amounts used for producible work. The following spreadsheets describe these numbers over time.

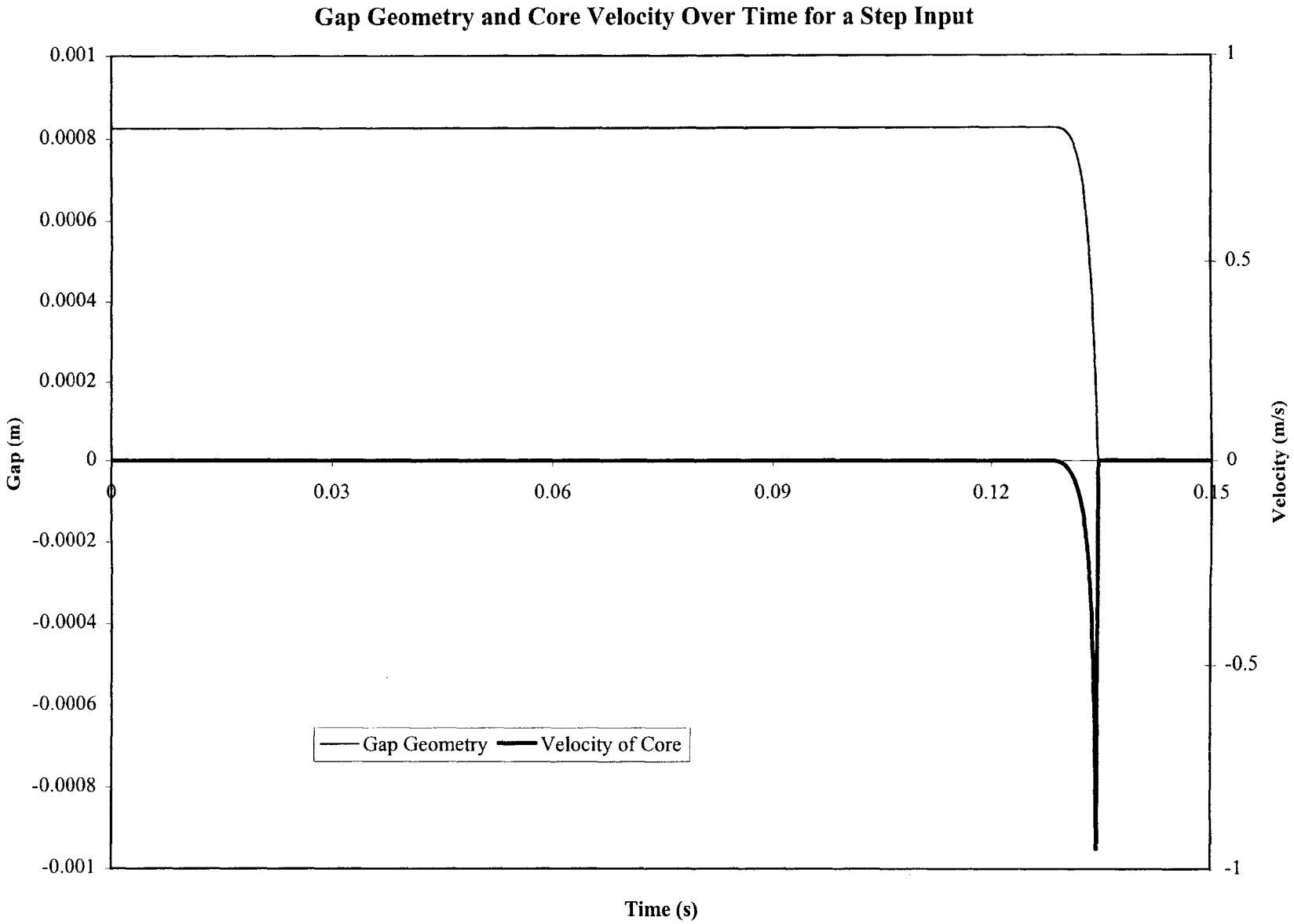
Gap Geometry and Core Velocity Over Time for a Step Input
0.001
0.0008
0.0006
0.0004
0.0002
0
-0.0002
-0.0004
-0.0006
-0.0008
-0.001
Gap (m)
1
0.5
0
-0.5
-1
Velocity (m/s)
0
0.03
0.06
0.09
0.12
0.15
Gap Geometry
Velocity of Core
Time (s)

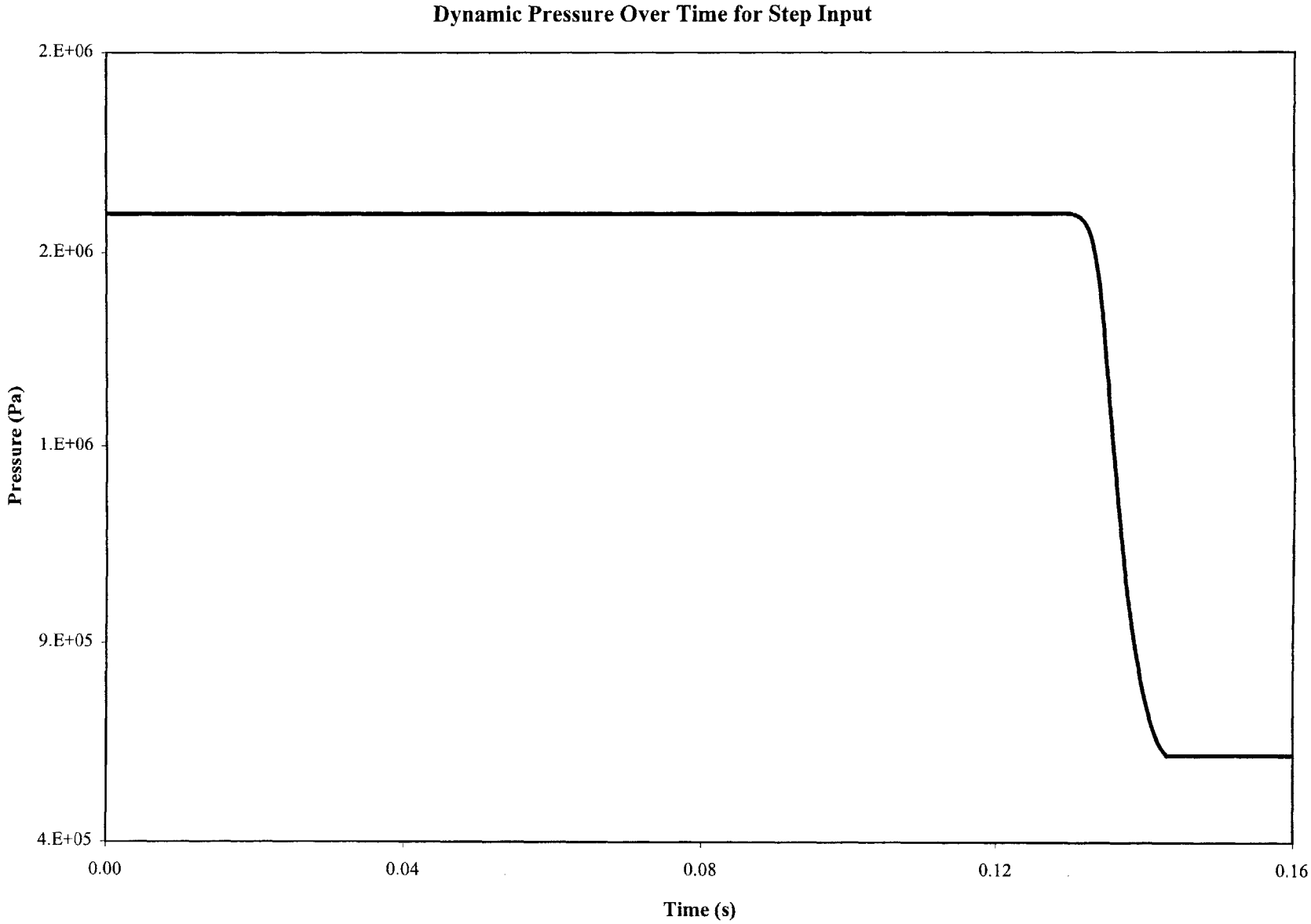
Dynamic Pressure Over Time for Step Input
2.E+06
2.E+06
1.E+06
9.E+05
4.E+05
Pressure (Pa)
0.00
0.04
0.08
0.12
0.16
Time (s)

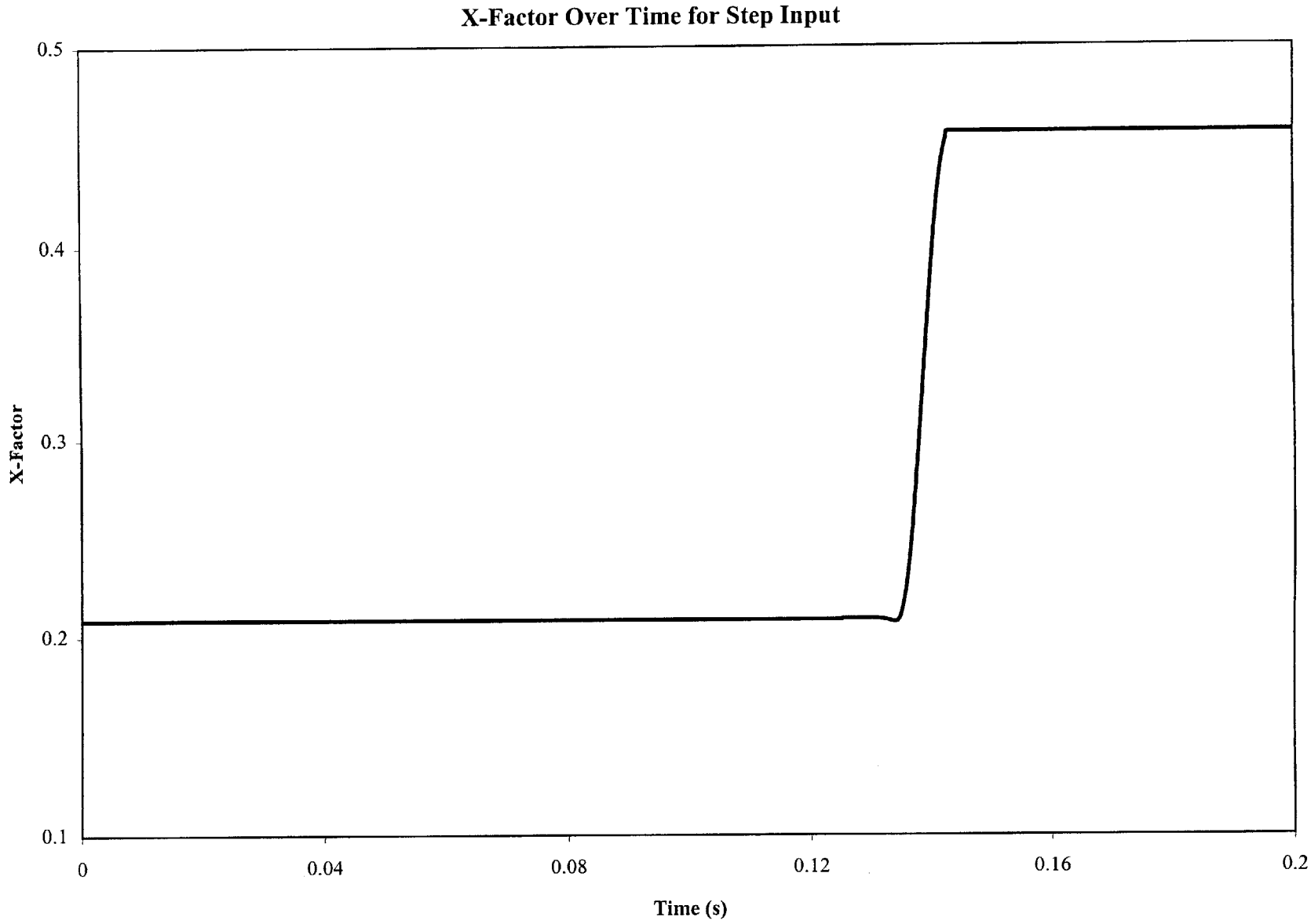
X-Factor Over Time for Step Input
0.5
0.4
0.3
0.2
0.1
X-Factor
0
0.04
0.08
0.12
0.16
0.2
Time (s)

Gap Geometry and Core Velocity Over Time for Capacitor Input

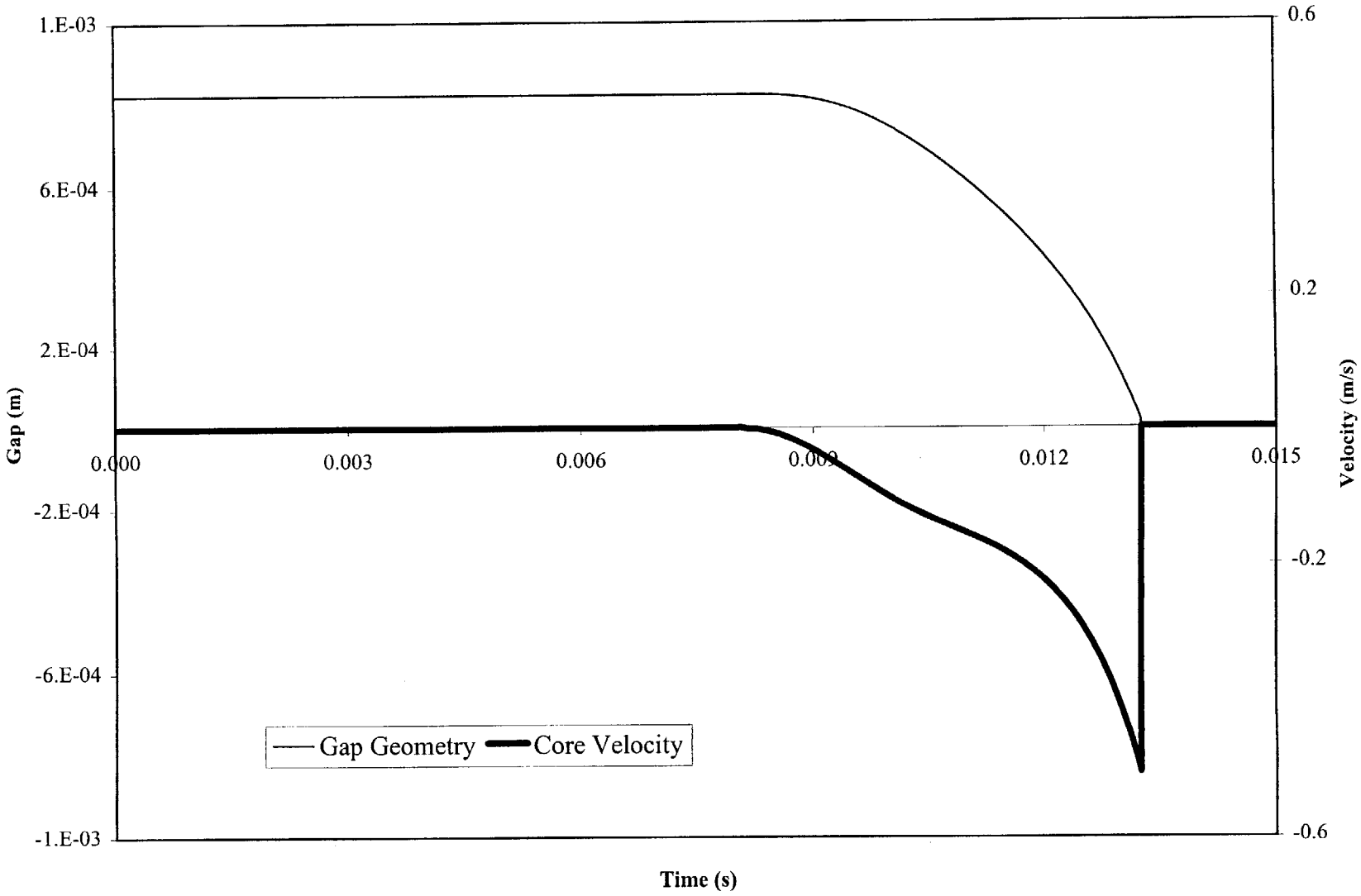

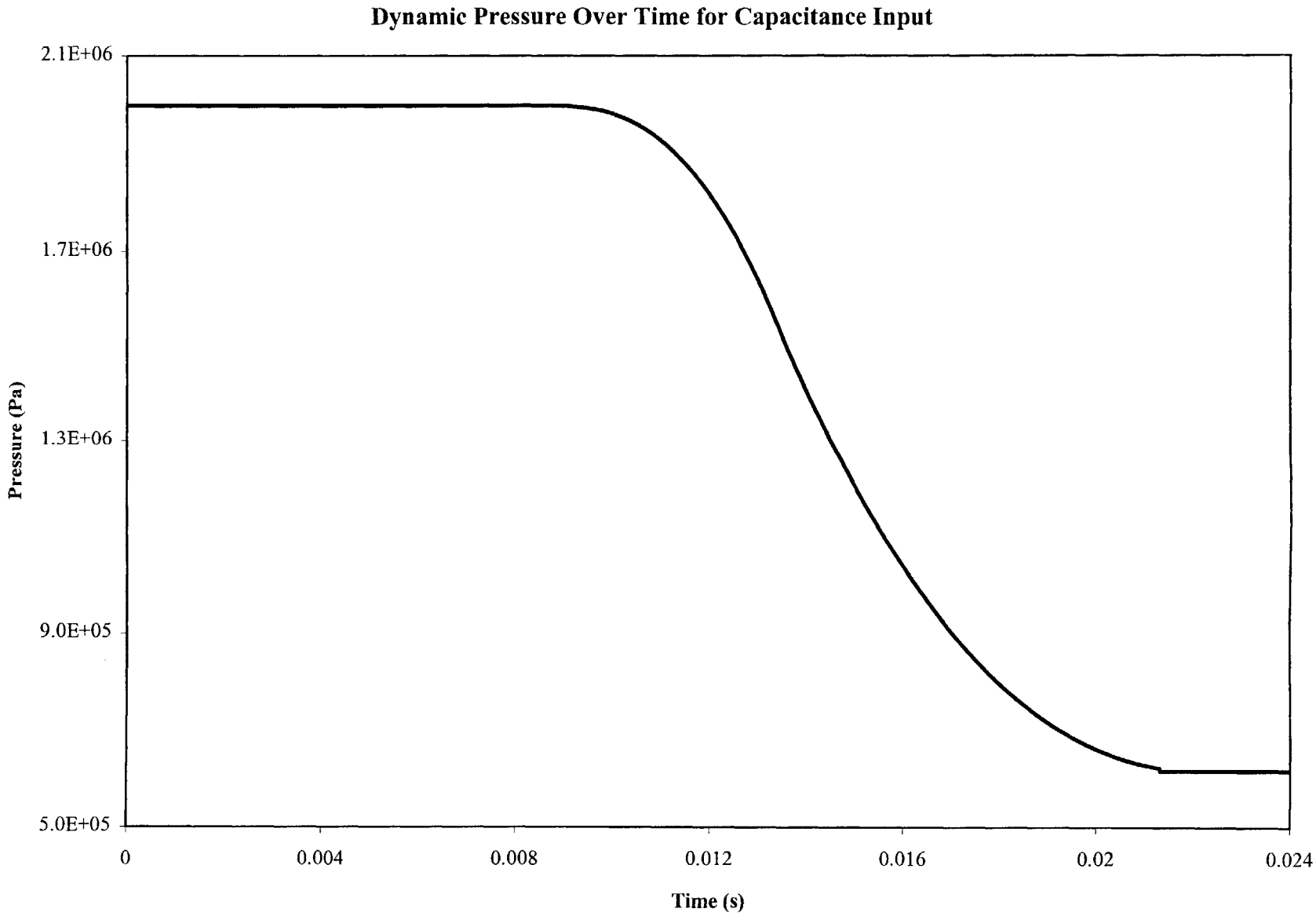
Dynamic Pressure Over Time for Capacitance Input
2.1E+06
1.7E+06
1.3E+06
9.0E+05
5.0E+05
Pressure (Pa)
0
0.004
0.008
0.012
0.016
0.02
0.024
Time (s)

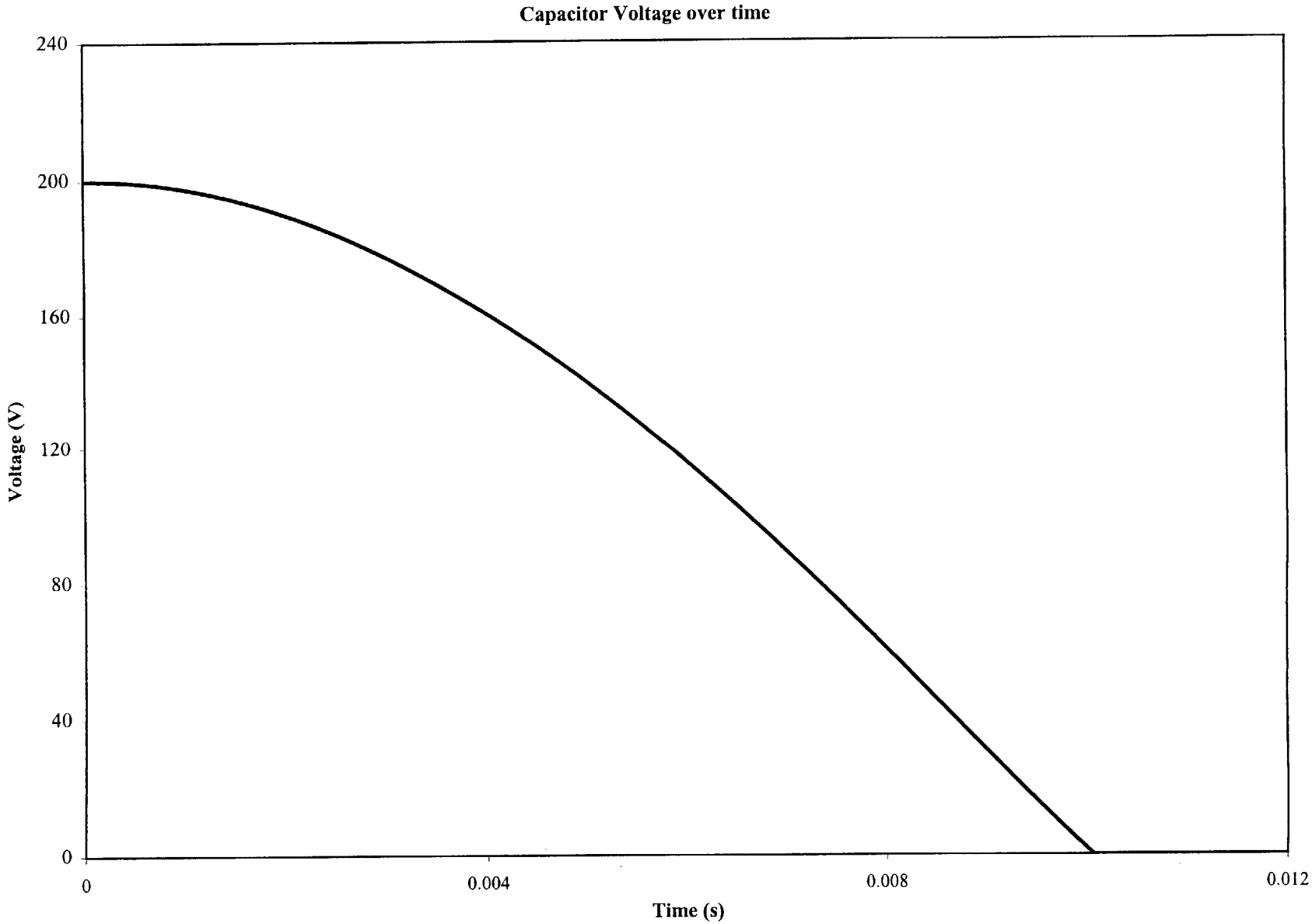
Capacitor Voltage over time
240
200
160
120
80
40
0
Voltage (V)
0
0.004
0.008
0.012
Time (s)

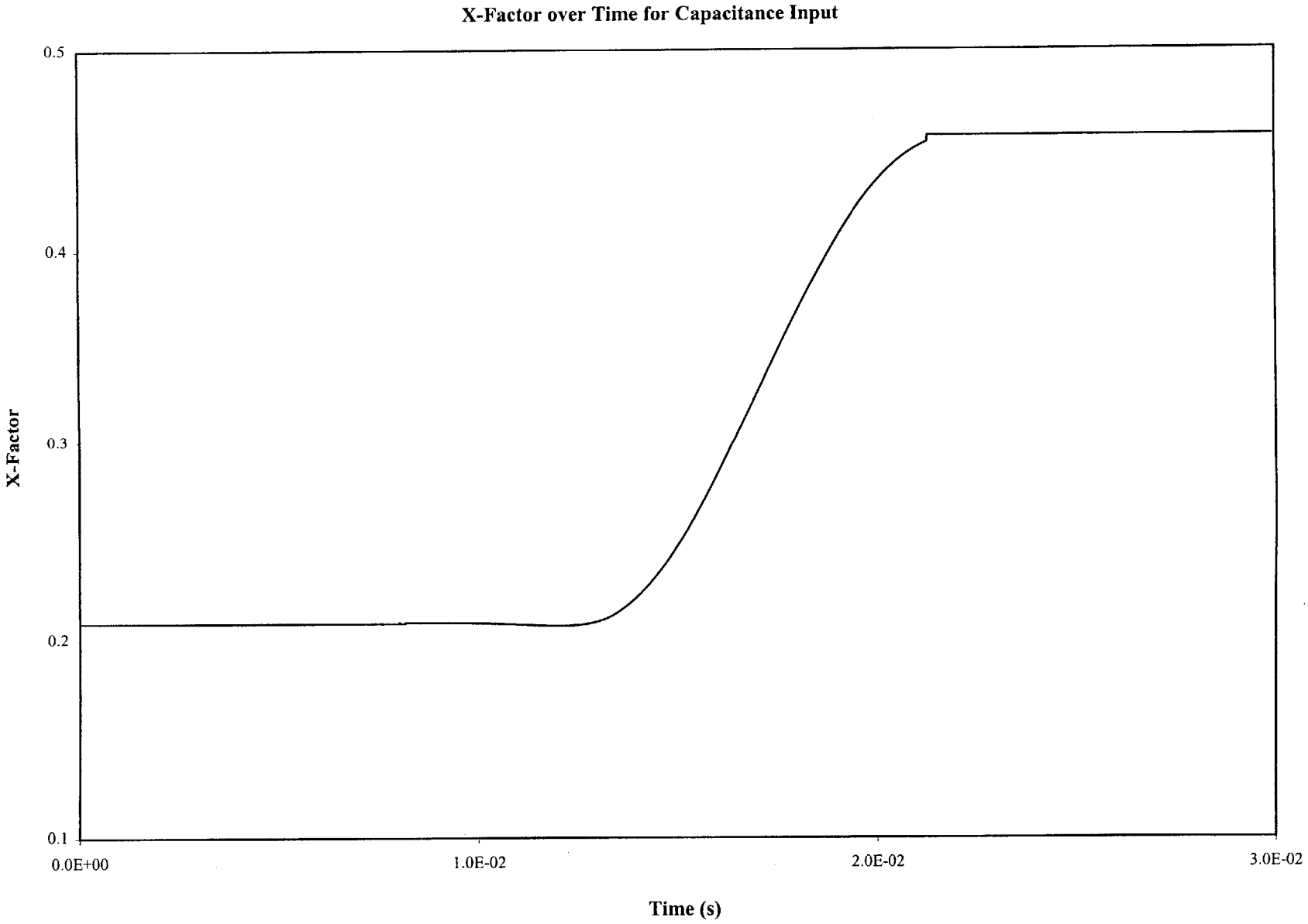
X-Factor over Time for Capacitance Input
0.5
0.4
0.3
0.2
0.1
X-Factor
0.0E+00
1.0E-02
2.0E-02
3.0E-02
Time (s)